REGIONAL MICROPHYSICAL AND RADIATIVE EFFECTS OF AEROSOLS

A Dissertation

by

YUN LIN

Submitted to the Office of Graduate and Professional Studies of
Texas A&M University
in partial fulfillment of the requirements for the degree of

DOCTOR OF PHILOSOPHY

Chair of Committee,	Renyi Zhang
Committee Members,	Donald R. Collins
	Courtney Schumacher
	Qi Ying
Head of Department,	Ping Yang

May 2018

Major Subject: Atmospheric Sciences

ABSTRACT

In this study, the regional-scale aerosol effects are quantitatively assessed under various weather conditions by conducting numerical modeling studies to improve the understanding of physical processes involved in aerosol-cloud and aerosol-radiation interactions.

A continental cloud complex consisting of three cloud regimes is simulated by the Weather Research and Forecast (WRF) model to investigate the aerosol microphysical effect (AME) and aerosol radiative effect (ARE). The results reveal that the responses of three cloud regimes to aerosols are jointly controlled by AME and ARE. The aerosol effects on the cloud complex are distinct from its individual cloud regime, highlighting that aerosol-cloud interactions for diverse cloud regimes and their transitions need to be carefully evaluated.

The increasingly severe regional haze in China is associated with a high ratio of oxygenated organic aerosol over odd-oxygen concentrations during clean-to-hazy transition periods, corresponding to intensive photochemical activities in Beijing. Modeling studies using WRF with an aerosol radiative module indicate that the aerosol-planetary boundary layer interactions during severe haze might trigger a positive feedback loop to amplify PM pollution. The small negative forcing at top of atmosphere (TOA) by the heavy loading PM is a result of the strong cooling largely canceled out by the strong heating. The aging of black carbon can contribute significantly to the total PBL collapse and the total BC TOA forcing.

The impacts of aerosols on a hurricane with ocean coupling is studied by using the WRF coupled with Regional Ocean Model System. The aerosol effect causes an expansion

of storm circulation at the cost of the intensity. The aerosol-induced feedback of ocean coupling shows an appreciable influence on the mature storm. The storm destructiveness tends to be exacerbated by the aerosol effect due to the circulation expansion and corresponding structure modulations under polluted condition.

DEDICATION

I would like to dedicate this document to my beloved wife Qiong Su and my newborn nephew Zipeng Yao, who just came to the world when I finished this dissertation.

ACKNOWLEDGEMENTS

CONTRIBUTORS AND FUNDING SOURCES

NOMENCLATURE

AME	Aerosol Microphysical Effect
AOD	Aerosol Optical Depth
ARE	Aerosol Radiative Effect
BC	Black Carbon
CCN	Cloud Condensation Nuclei
CWP	Cloud Water Path
DCCs	Deep convective clouds
HYCOM	HYbrid Coordinate Ocean Model
LWC	Liquid Water Content
NCP	Northern China Plain
PBL	Planetary Boundary Layer
PM	Particulate Matter
RACORO	Routine Aerial Facility Clouds Optical Radiative Observations
SGP	Southern Great Plain
SSA	Single Scattering Albedo
SST	Sea Surface Temperature
SLP	Sea-Level Pressure
TC	Tropical Cyclone
WRF	Weather Research and Forecast

TABLE OF CONTENTS

LIST OF FIGURES

LIST OF TABLES

1. INTRODUCTION[*]

1.1   Overview of Aerosol Microphysical Effects and Aerosol Radiative Effects

By acting as cloud condensation nuclei (CCN) and ice nuclei, atmospheric aerosols greatly affect cloud and precipitation processes, which is referred to as the aerosol microphysical effect (AME) (Twomey 1977; Zhang et al. 2007; DeMott et al. 2011; Tao 2015). Aerosols also alter the Earth's radiative budget by scattering and absorbing shortwave and longwave radiation (Charlson and Pilat 1969; Coakley et al. 1983; Peng et al. 2016), referred to as the aerosol direct effect, which in turn modifies the atmospheric temperature structure and cloud lifetime (Hansen et al. 1997; Ackerman et al. 2000; Wang et al. 2013b), referred as the aerosol semi-direct effect. The aerosol direct and semi-direct effects commonly are considered together as the aerosol radiative effects (ARE). Currently, the understanding of the aerosol effects on weather and climate remains uncertain, since the representation of aerosol and cloud processes, particularly the subgrid cloud dynamics and feedback, by atmospheric numerical models is still difficult. This difficulty is partially responsible for the largest uncertainty in climate projections (IPCC 2013; Wu et al. 2016).

The responses of clouds and precipitation to variable aerosol loadings are complicated, depending on the aerosol properties, cloud systems, and environmental

_____

*Part of this section is reprinted with permission from "Distinct Impacts of Aerosols on an
 Evolving Continental Cloud Complex during the RACORO Field Campaign" by Lin, Y., Y.
 Wang, B. Pan, J. Hu, Y. Liu, and R. Zhang, 2016. *J Atmos Sci*, 73(9), 3681-3700. ©American
 Meteorological Society. Used with permission.

conditions (Yuan et al. 2008; Khain 2009; Lee et al. 2009; Li et al. 2011). Several previous studies (Khain et al. 2005; Seifert and Beheng 2006; Tao et al. 2007; Khain et al. 2008; Lee et al. 2010; Storer et al. 2010; Li et al. 2011; Small et al. 2011) have indicated that the aerosol-cloud interactions differ among the cloud types and regimes. For example, shallow cumulus and marine stratocumulus have been demonstrated to be sensitive to AME (Kaufman et al. 2005; Matsui et al. 2006; Xue et al. 2008; Kogan et al. 2012; Yang et al. 2012; Werner et al. 2014), since an increased aerosol concentration leads to a smaller effective droplet radius, a higher droplet concentration, less precipitation, a higher cloud liquid water, longer-lived clouds, and a larger cloud fraction. However, a number of other studies of shallow cumulus have indicated that the cloud fraction and lifetime are not necessarily enhanced under more polluted conditions (Wang et al. 2003; Jiang and Feingold 2006; Lin et al. 2006; Small et al. 2009; Seigel 2014; Saleeby et al. 2015). Deep convective clouds (DCCs) are also affected by AME. For example, a higher aerosol loading leads to a suppressed warm rain process but enhanced mixed-phased processes (Andreae et al. 2004; Khain et al. 2005; van den Heever et al. 2006; Li et al. 2008b). The modifications on DCC microphysical processes by aerosols are attributed to the enhancements of liquid water mass loading and additional latent heat released, leading to invigorated convection (Li et al. 2008a; Li et al. 2008b; Tao et al. 2012), or to an increasing amount of long-lasting small ice particles in stratiform/anvils, as recently suggested by Fan et al. (2013). Conflicting results have been reported for the aerosol impacts on precipitation in different deep convective systems (Khain et al. 2005; Tao et al. 2007; Wang et al. 2011; Lee and Feingold 2013), and those previous studies have demonstrated that the correlation between AME and

2

aerosols is highly variable, dependent of the scale and types of clouds and meteorological environments (Tao et al. 2007; Khain et al. 2008; Jiang et al. 2011).

Progress has also been made to elucidate the aerosol-cloud-radiation feedback on the regional and global scales (Tie et al. 2003). Several studies have revealed that a reduced cloud cover, lowered cloud optical thickness, or a short cloud lifetime occurs for low and mid-level clouds with absorbing aerosols (Johnson et al. 2004; Zhang et al. 2008; Allen and Sherwood 2010; Sakaeda et al. 2011; Li et al. 2013). Fan et al. (2008) have shown that ARE induces a decrease in relative humidity, resulting in a decreased cloud cover and optical depth and suppressed precipitation for a daytime DCC. A study of ARE on sea breezes by Grant and van den Heever (2014) has shown that aerosols suppress the precipitation due to reducing down-welling shortwave radiation and surface latent heat fluxes. The aerosol semi-direct effect is dependent of the locations of an aerosol layer relative to the clouds and underlying surface (Lindeman et al. 2011; Wang et al. 2013b). For the case that aerosols lie above a cloud layer, particularly for marine stratocumulus cloud decks over the regions off the western coasts of continents, the diabatic heating due to aerosol absorption strengthens the inversion and reduces the entrainment rate, causing an enhancement of stratocumulus clouds (Wilcox 2010; Sakaeda et al. 2011; Li et al. 2013; Yamaguchi et al. 2015).

1.2   AME and ARE on Cloud Complex with Various Cloud Regimes

Realistic simulations of the various cloud systems are crucial to reduce the uncertainty in the quantitative assessment of the aerosol effects on climate (IPCC 2013). Although the previous studies have examined the aerosol effects on isolated continental DCCs (Fan et al. 2007b; Fan et al. 2008; Li et al. 2008b), the continental cloud system

consisting of various boundary layer cloud regions has not been properly represented in current atmospheric models due to poorly parameterized small-scale turbulence and convection (Zhang et al. 2005; Vogelmann et al. 2012; Wood 2012).

To evaluate the properties of such continental boundary layer clouds and their association with aerosols, a field campaign, Routine AAF Clouds with Low Optical Water Depths (CLOWD) Optical Radiative Observations (RACORO) organized by DOE, has been conducted at the ARM Southern Great Plain (SGP) site (Vogelmann et al. 2012). The five-month campaign provides the first extended-term airborne and ground-based cloud and aerosol information for various continental boundary layer clouds. The RACORO campaign has already been examined by some parameterization studies (Lu et al. 2013). However, detailed studies on AME and ARE from the RACORO continental cloud systems are still lacking. In addition, most of the previous studies have focused on either AME or ARE (Johnson et al. 2004; Lee and Feingold 2013), and only a few studies, e.g., Fan et al. (2008), Shi et al. (2014), and Jiang and Feingold (2006), have been specifically designed to simultaneously examine the overall aerosol effects at the cloud-resolving scale, including aerosol direct, semi-direct, and indirect effects, particularly for the continental boundary layer clouds. Shi et al. (2014) simultaneously tested AME and ARE on continental convective clouds over west Africa and found that ARE dominantly modulates the dynamics of convective clouds.

In addition, the monotonicity of cloud response to aerosols depends on cloud types and aerosol levels (Li et al. 2008b; van den Heever et al. 2011; Saleeby et al. 2015). In a cloud complex, the aerosol effects associated with an individual cloud regime likely offset or compensate with each other, so-called buffering effect (van den

Heever et al. 2011). Moreover, the recent IPCC report (2013) and other previous studies, e.g., Li et al. (2011) and Fan et al. (2013), have indicated that the investigation of long-term aerosol net effects on different cloud types are critical because aerosol effects are likely different for the different cloud regimes and the net aerosol effects could be quite different from any individual one. Therefore, it is necessary to study the overall aerosol effects on a combination of various cloud regimes and to evaluate the aerosol effects during cloud regime transition.

1.3   Aerosol Pollution Characteristics and Aerosol-Radiation-PBL Interactions During Severe Haze Formation

With rapid economic growth, fast urbanization, and increasing population, many regions have experienced frequently severe regional haze due to the extremely heavy particulate matter (PM) pollution (Zhang et al. 2015b). Northern China Plain (NCP) is one of the regions suffering severe haze condition (Guo et al. 2014). The severe haze in China has attracted public attention because the heavy PM pollution during hazy days has induced great degradation in visibility and air quality, adverse effects on human health, and likely pronounced modifications on regional and global weather systems (Wang et al. 2014b; Zhang et al. 2015b). Direct emissions and subsequent secondary PM formation are the primary reasons for the severe haze in China (Guo et al. 2014; Sun et al. 2014; Zhang et al. 2015b; Wang et al. 2016a), and adverse weather conditions for pollution dispersion, such as high-pressure control, suppressed local atmospheric circulations, and weakened large-scale circulation, are considered external causes leading to haze (Liu et al. 2013; Wang et al. 2014d; Cai et al. 2017). However, it still remains unclear that what are the primary formation

mechanisms leading to the heavy PM pollution and how the PM pollution evolves and eventually results in severe regional haze events in China (Zhang et al. 2015b).

The photochemical reactions are one of the primary mechanisms leading to the rapid PM accumulations at the early stage of severe haze formation (Guo et al. 2014; Zhang et al. 2015b). At the instance of the haze in Beijing, the remarkably efficient PM formation due to photochemical activity is characterized by the most rapid particle size and mass growths coincided with increasing ozone levels during daytime (Zhang et al. 2015a). But how efficient the photochemical production of PM could be during severe haze events and what are the distinctive features of the extremely heavy PM pollution in megacities in China comparing with the PM pollution in other megacities across the world still need to be elucidated in detail to better understand the severe haze in China.

The importance of aerosol regional climate effects has been recognized for the polluted condition, given that haze events occur throughout the year in China (Ramanathan et al. 2007; Wang et al. 2009; Wang et al. 2015a). But the aerosol radiative forcing and climatic implications under extremely hazy condition are still in lack of accurate quantification, evident with a large dispersion of the value of aerosol radiative forcing during severe haze events (Li et al. 2007; Xia et al. 2007; Wang et al. 2009; Che et al. 2014). In addition, the interactions between aerosol and planetary boundary layer (PBL) due to aerosol radiative effects might increase the haze severity, particularly during winter when haze occurs frequently (Wang et al. 2015a; Wang et al. 2016b; Zhang et al. 2018). The meteorological conditions in boundary layer like atmospheric stability and moisture can be further altered by aerosol-PBL interactions, thus inducing additional elevation of PM pollution near ground (Tang et al. 2016a; Tie et al. 2017). However, the aerosol-PBL

interactions and their subsequent feedbacks in thermodynamics and dynamics are still in need of sufficient quantification under extremely hazy condition (Li et al. 2017).

The role of black carbon (BC) in aerosol-PBL interactions and aerosol regional climate effects has been documented by previous studies (Menon et al. 2002; Bond et al. 2013; Wang et al. 2013b; Ding et al. 2016). The BC aging process has been demonstrated to markedly enhance BC absorption by considerably modifying particle chemical and physical properties (Zhang et al. 2008; Peng et al. 2016; Peng et al. 2017). For example, Peng et al. (2016) experimentally documented through a series of chamber studies in Beijing that the mass absorption cross section (MAC) of BC is enhanced by 2.4 times in a short time because of BC aging. Apparently, the BC absorption enhancement might cause additional aerosol radiative forcing (Peng et al. 2016) and suppression on PBL development (Wang et al. 2017), but the studies on the radiative effect of BC aging are limited, requiring more quantitative examination on it (Wang et al. 2013b; He et al. 2015; Gustafsson and Ramanathan 2016).

1.4   Aerosol-hurricane-ocean Interactions

Tropical cyclone (TC) development is affected by several factors associated with the TC's energy supply (heat and moisture), including sea surface temperature (SST) and wind shear (Emanuel et al. 2004; Khain et al. 2010). In addition, the weakening effect of aerosol on TCs have been recognized in past decades (Rosenfeld et al. 2007; Khain et al. 2010; Rosenfeld et al. 2012; Wang et al. 2014a). As a result of aerosol microphysical and thermodynamic responses, the outer rainbands are invigorated due to additional latent heat release at upper-level from the freezing of supercooled water under polluted condition. This invigoration of outer rainbands induces strong low-level cooling due to the intensive evaporation of precipitation, and thus the supply of warm and moist air for storm center is

reduced and the convection over the eyewall region is suppressed, eventually weakening the hurricane. Moreover, hurricane development can be delayed and the decay takes place earlier under polluted conditions, with an enlarged rainband and increased precipitation (Wang et al. 2014a). If aerosols penetrate the storm core, the eyewall would be invigorated, particularly at the early stage when the storm forms and its circulation is not well organized (Cotton et al. 2012; Herbener et al. 2014).

It is well-known that the strong winds associated with the passage of TCs over the ocean induce a strong vertical mixing and upwelling in the ocean subsurface layer near the core of the storm, which could lead to a decrease in ocean surface temperature. The cold wake after TCs, in turn, weakens the storm intensity and fosters the storm circulation expansion via reducing heat and moisture exchange from ocean surface to the storm (Bender et al. 1993; Ma et al. 2013). The simulations of TCs carried out only with atmosphere models (e.g., WRF), in which SST is prescribed or fixed, normally overestimate the intensity of hurricanes (Dodla et al. 2011; Wang et al. 2014a; Lynn et al. 2016). The overestimation by previous studies is partially due to the missing air-sea interactions in the simulations since atmosphere-ocean interactions show strong negative feedback on storm intensity (Khain and Ginis 1991; Schade and Emanuel 1999). Therefore, it is expected that the use of coupled atmosphere-ocean models would improve the simulations of TCs and thus more accurately predict hurricane development.

On the other hand, aerosols might induce changes in the convergence process in the subsurface mixing layer and associated upwelling of cold water by modifying the thermodynamic and dynamic conditions near the surface layer (Khain et al. 2016; Lynn et al. 2016), which in turn impacts TC intensity and/or structure. However, most of the previous

studies on aerosol-hurricane interactions either use fixed SST or prescribe SST from reanalysis data (Rosenfeld et al. 2011; Wang et al. 2014a), which could lead to biases when evaluating aerosol effects on hurricanes because of the missing feedbacks of air-sea interactions. Therefore, there is a need to incorporate ocean feedbacks into modeling studies to investigate the aerosol-hurricane-ocean three-way interactions.

There is potentially non-linear and complicated three-way interaction among aerosol, hurricane, and SST. On the one hand, the aerosol weakening of hurricane in turn weakens the wind stress over the ocean and thus reduces the vertical mixing and upwelling. Therefore, the negative feedback on hurricane intensity due to air-sea interactions is mitigated because of aerosol effects. On the other hand, the reduced ocean surface cooling is favorable to evaporate water from ocean to atmosphere, again energizing the hurricane. However, few studies have been conducted on aerosol impacts on TCs using atmosphere-ocean coupled models until recently. Lynn et al. (2016) and Khain et al. (2016) perform simulations on hurricane Irene under polluted condition using a coupled atmosphere-ocean model and found that both aerosol effects and ocean coupling weaken hurricane intensity, and particularly, the timing of Irene's intensity evolution cannot be well captured without air-sea interactions, even with aerosol effects.

However, the one-dimensional ocean model used in Lynn et al. (Lynn et al. 2016) still shows an underestimate of the SST cooling when the hurricane passed by around 1 °C on average, since the 1-D ocean model has a limited ability to accurately predict the physical process of convergence and its associated upwelling cooling. By comparing simulations using 1-D and 3-D ocean model coupling with a hurricane model, Yablonsky and Ginis (2009) suggests that the 3-D ocean model performs much better in the upwelling cooling

induced by the three-dimensional physical process in the upper ocean than 1-D one. In addition, the ocean coupling effect is not isolated yet in most of the previous studies, and particularly its importance relative aerosol effects on hurricane development need to be examined separately.

1.5 Objective

The major objective of this study is to investigate the regional-scale aerosol effects under various weather conditions. The specific tasks are: (1) to study aerosol microphysical and radiative effects on a continental cloud complex during the RACORO field campaign, in which three different sequentially appearing continental cloud regimes are identified. Simulations using Weather Research and Forecasting with and without ARE are conducted to examine the responses of cloud micro- and macrophysics and precipitation to aerosol loadings. The aerosol effects due to cloud transition and the aerosol net effects on the cloud complex are particularly evaluated to accurately assess the overall response of the various cloud regimes; (2) to elucidate the formation and evolution of severe haze in China as well as the regional climate effects under extremely hazy condition, by conducting case studies on two typical severe haze episodes occurring in fall of 2013 in Beijing, China. The WRF model coupled with an explicit aerosol radiative module is employed to examine the interactions between severe haze and PBL as well as aerosol/BC radiative forcing. Particularly, to what extent the BC aging can affect the haze-PBL interactions and its contribution to net aerosol radiative forcing during severe haze periods are explicitly studied; (3) to investigate the aerosol-hurricane-ocean three-way interactions by performing modeling studies on Hurricane Katrina 2005 using a regional three-dimensional atmosphere-ocean coupled model, WRF-ROMS. The WRF coupled with

a 3-dimension ocean model (Patricola et al. 2012) is employed to incorporate the thermodynamic and dynamic feedbacks of air-sea interactions to aerosol-hurricane interactions. By contrasting a coupled simulation on the polluted hurricane and an uncoupled one with SST from the outputs of the corresponding clean coupled case, it is the first time that the aerosol-induced ocean coupling effect is isolated from aerosol-hurricane interactions and the relative importance of ocean coupling in comparison with aerosol effects is evaluated.

2. NUMERICAL MODEL DESCRIPTION

2.1 Aerosol-aware Two-moment Bulk Microphysical Scheme

An aerosol-aware two-moment bulk microphysics scheme has been developed by Li et al. (2008b) at Texas A&M University and then implemented into Weather Research and Forecasting (WRF) model (hereafter TAMU-WRF). The detailed description of the TAMU microphysics scheme can be found in Li et al. (2008b), in which the number concentrations of aerosols and cloud droplets are prognostically treated. This prognostic treatment is in contrast to the diagnostic feature commonly adopted in many other two-moment bulk microphysics schemes (Wang et al. 2011). Aerosols activated to form cloud droplets are assumed to contain ammonium sulfate only for AME, since ammonium sulfate represents one of the abundant aerosol chemical compositions at various continental locations (Fan et al. 2005; Zhang et al. 2015b). Also, although organics, formed from photochemical oxidation of biogenic and anthropogenic volatile organic compounds (Lei et al. 2000; Zhang et al. 2002; Zhao et al. 2005), constitute the other key ingredient in aerosols, the aerosol hygroscopicity is dominated by the inorganic fraction (Guo et al. 2014). Nucleation scavenging is the only mechanism to remove aerosols in our scheme, and aerosol regeneration from droplet evaporation is not considered yet. Under favorable wind conditions, aerosols with a fixed number and mass concentration at the lateral boundaries of the outer domain are transported through advection and convection to provide an additional aerosol source for the inner domain.

The microphysical scheme explicitly calculates the mass mixing ratios and number concentrations of five hydrometeor categories, i.e., cloud droplet, rain drop, ice crystal,

snow, and graupel. In total 32 microphysical processes are included in the scheme for treatments of the conversions between the five types of hydrometeors and self-conversions between them. Specifically, the heterogeneous ice nucleation and homogeneous freezing processes are explicitly parameterized in this microphysics scheme. The deposition nucleation parameterization is based on Pruppacher and Klett (1997), and the immersion-freezing parameterization follows Bigg (1953). The homogeneous freezing is parameterized following Milbrandt and Yau (2005). The Rapid Radiative Transfer Model (RRTM) scheme (Mlawer et al. 1997) and the Goddard scheme (Chou and Suarez 1999) are employed as the longwave and shortwave radiation parameterizations, respectively. Usually, the YSU scheme (Hong et al. 2006) and the thermal diffusion scheme are adopted for the planetary boundary layer parameterization and for the land surface, and no cumulus parameterization is considered.

TAMU-WRF has been successfully used for investigations of AME on cloud, precipitation, or lightning activities in isolated convective storms and mesoscale convective systems (Li et al. 2009; Wang et al. 2011; Wang et al. 2013a; Wang et al. 2014a; Wang et al. 2014b).

2.2   Aerosol Radiative Module with Different Mixing State Assumptions

An aerosol radiative module is implemented in the Goddard Shortwave Radiation Scheme in WRF to online compute wavelength-dependent aerosol optical properties, including aerosol optical depth, asymmetry factor and single scattering albedo (SSA) (Fan et al. 2008). By using the aerosol radiative module, we can explicitly evaluate aerosol radiative effects on clouds and the development of the planetary boundary layer.

Ammonium sulfate and black carbon (BC) are the two chemical compositions considered for computing aerosol optical properties. In addition, two types of aerosol mixing state assumptions are employed in this study. One is internal mixing, in which the aerosol mixture consists of ammonium sulfate and BC. Given the internal mixing assumption, the composite reflective index of aerosol particles is calculated using the volume-weighted reflective index of an individual component. Another assumption is core-shell configuration, in which BC is taken as the core and ammonium sulfate is treated as the shell. The core-shell configuration is employed for investigating BC aging process. A Mie theory code named as DMILAY for a layered sphere is implemented into the aerosol radiative module (Toon and Ackerman 1981) to handle the calculations with the core-shell configuration. For the two mixing states, the mass percentage of an individual component is based on available measurements nearby. For example, for the case at the southern region of United States, the aerosol is assumed consisting of 95% ammonium sulfate and 5% BC, which is consistent with observations (Levy et al. 2013) and other model studies (Wang et al. 2014c).

In addition, the hygroscopic growth of aerosol particles is taken into account, following Mallet et al. (2004). This aerosol radiative module has been successfully applied to investigate aerosol radiative effects on deep convective clouds (Fan et al. 2008) and storm system (Wang et al. 2014a).

2.3 Regional Atmosphere-ocean Coupled Cloud-resolving Model-WRF-ROMS

Given that the ocean feedback could be a crucial factor to influence hurricane due to the strong upwelling cooling associated with hurricane passage, there is a need to incorporate air-sea interactions when we evaluate the aerosol effect on hurricane development. In this

14

study, we proposed to couple WRF with the Regional Ocean Modeling System (WRF-ROMS) to examine the aerosol-hurricane-ocean three-way interactions.

ROMS is a hydrostatic, free-surface, terrain-following 3-dimensional ocean model. Comparing to 1-D ocean model, ROMS can well capture the 3-D process of upwelling cooling. Also, due to its 3-D nature, ROMS can consider salinity modifications in the ocean, which is induced by a large amount of precipitation at the ocean surface when a hurricane passes by. The aerosol effect on sea level height can be studied as well by using ROMS.

With an interface coupler, ROMS updates SST to WRF, and precipitation minus evaporation, surface wind, latent and sensible heat fluxes, as well as radiative fluxes are exchanged from WRF to ROMS (Patricola et al. 2012). The WRF and ROMS couples every 10 min.

3. DISTINCT IMPACTS OF AEROSOLS ON AN EVOLVING CONTINENTAL CLOUD COMPLEX DURING THE RACORO FIELD CAMPAIGN[*]

3.1 Experiment Design and Simulation Evaluation

The evolving continental cloud complex over the SGP region spanned from 25 to 27 May 2009, including shallow cumuli, a DCC, and a one-day persisting stratus. On 25 May, the shallow cumuli formed by weak and isolated convection and lasted for a few hours (0900 LST – 1800 LST) with small-scale drizzle precipitation at the dissipation stage. From 1700 LST on 25 May to 0900 LST on 27 May, a large-scale cold front passed across the SGP region, stretching from the low-pressure center in South Dakota to the southwest end in the Texas Panhandle. A strong prefrontal convective line passed the ARM site observational area in the early morning of 26 May (from 0000 LST to 0600 LST) associated with the formation of DCC, which caused intensive precipitation. During and after the cold front passage at the SGP site, a weakly precipitating stratus developed at 2100 LST on 26 May and persisted throughout 27 May, with relatively thick cloud physical and optical depths.

The model domain is configured with three two-way nested grids, as shown in Fig. 3.1. The outmost domain has a size of 900 km × 900 km with a horizontal grid spacing of 9 km, centered at the SGP central facility (36.5934ºN, 97.5113ºW). The size and horizontal

_____

grid spacings are 540 km × 540 km and 3 km for the second domain and 228 km × 228 km and 0.75 km for the innermost domain, respectively. Unless stated otherwise, a domain inside the innermost domain with a size of 105 km × 105 km around the SGP site is used for analysis throughout this paper in order to minimize the interference from co-existing cloud regimes at the same time period and covers the flight routes during RACORO campaign. The vertical coverage is 20 km, consisting of fifty vertical levels with a stretched vertical resolution, which is finer close to the ground (about 50 m) and coarser aloft (about 400 m above 14 km). North American Regional Reanalysis (NARR) is used as the initial condition and lateral boundary conditions, which are updated every 3 hrs.
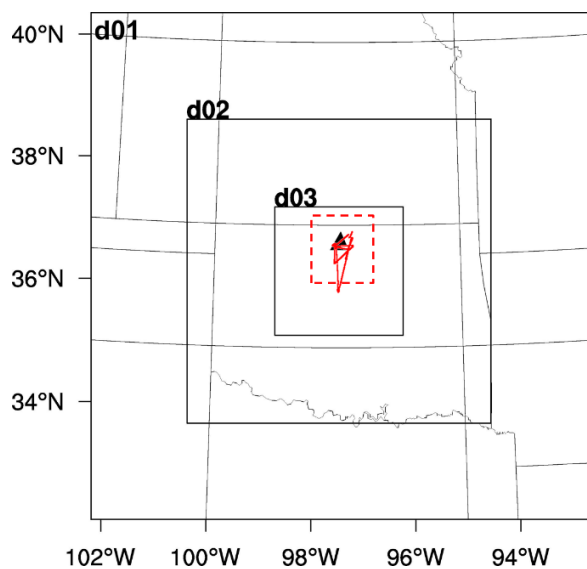
Figure 3.1 Two-way nested configuration of the modeling domains. Reprinted and adapted with permission from the American Meteorological Society (Lin et al. 2016).

17

Sensitivity experiments are conducted to evaluate the aerosol impacts on cloud and precipitation processes. Three different aerosol scenarios are considered to reflect the range of aerosol conditions during the RACORO field campaign in 2009: A run with a clean aerosol condition (Clean), a run with the moderate aerosol level close to the measurements (Mode), and a run with the polluted condition (Pollu), with the initial surface aerosol concentrations of 280, 700, and 2800 cm^{-3}, respectively. As shown in Fig. 3.2, the initial aerosol vertical profiles below 2 km are constrained by the airborne Passive Cavity Aerosol Spectrometer Probe (PCASP) measurements collected on 26 May and 27 May, 2009 during the RACORO field campaign since PCASP contains most aerosols responsible for cloud droplet formation under weak turbulence (Vogelmann et al. 2012). An approximately exponentially decreasing dependence is employed to represent the aerosol profiles with height above 2 km (Fan et al. 2007a; Li et al. 2009).
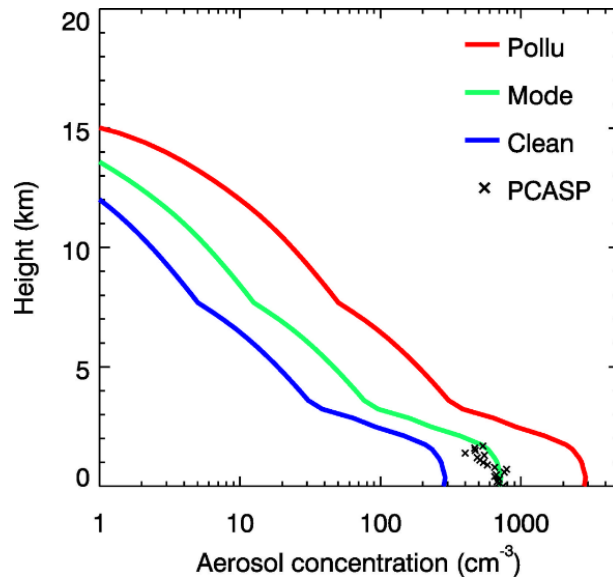
Figure 3.2 Aerosol vertical profiles as initial conditions for modeling study. Reprinted and adapted with permission from the American Meteorological Society (Lin et. al., 2016).

Two simulations for each aerosol scenario are conducted, i.e., with AME only and with both aerosol microphysics and radiative effects (MRE). ARE is evaluated from the differences between MRE and AME simulations. Considering that the underlying microphysics-dynamics-thermodynamics interactions of the system are nonlinear, the differences between MRE and AME for the DCC and stratus are not solely attributable to ARE, but also to the cloud-environment interactions before the DCC or the stratus. To separate ARE from the impacts of development of preceding clouds on the condition prior to latter clouds, we perform additional simulations with the inclusion of microphysical (AME) and radiative (ARE) effects only (defined as MRO hereafter), in which ARE is included starting on the second day (the deep convection regime onward) and then only on the third day (the stratus regime only). See Fig. 3.3 for detailed information.
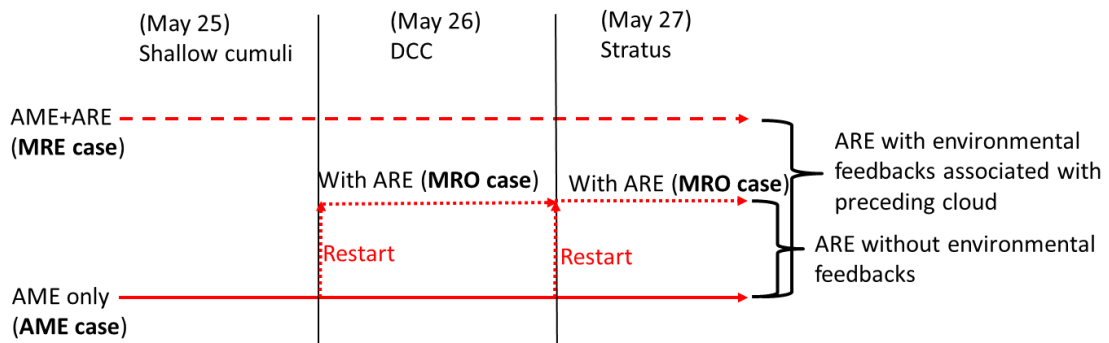
Figure 3.3 Simulation scheme to separate ARE from environmental feedbacks induced by ARE on the preceding clouds.

In order to validate our model performance, the AME and MRE simulations conducted for the moderate pollution scenario are compared with the observations from the RACORO campaign. The comparison between the ground-based measurements of CCN from ARM Aerosol Observing System and simulations shows that our simulations generally capture the temporal variation of the observed CCN (Fig. 3.4d).

The observed cloud fraction is obtained from the ARM Active Remotely-Sensed Cloud Locations (ARSCL) Value-Added product. The cloud fraction from the simulations is defined as the percentage of the grids with a total hydrometeor water mass mixing ratio greater than 10^{-6} kg kg^{-1} within a region of 10 km x 10 km centered at the SGP site. Figs. 3.4a and 3.5 depict the temporal evolutions of the observed and simulated cloud fraction during 25 - 27 May, showing that both the AME and MRE runs reproduce the major characteristics of the different clouds and the transition of the cloud types in terms of the cloud onset time, duration, and size, although the modeled stratus is rather discontinuous. Fig. 3.4a also shows that the simulated cloud fraction is underestimated for shallow cumuli, and the simulated stratus dissipates earlier than that of the observation.
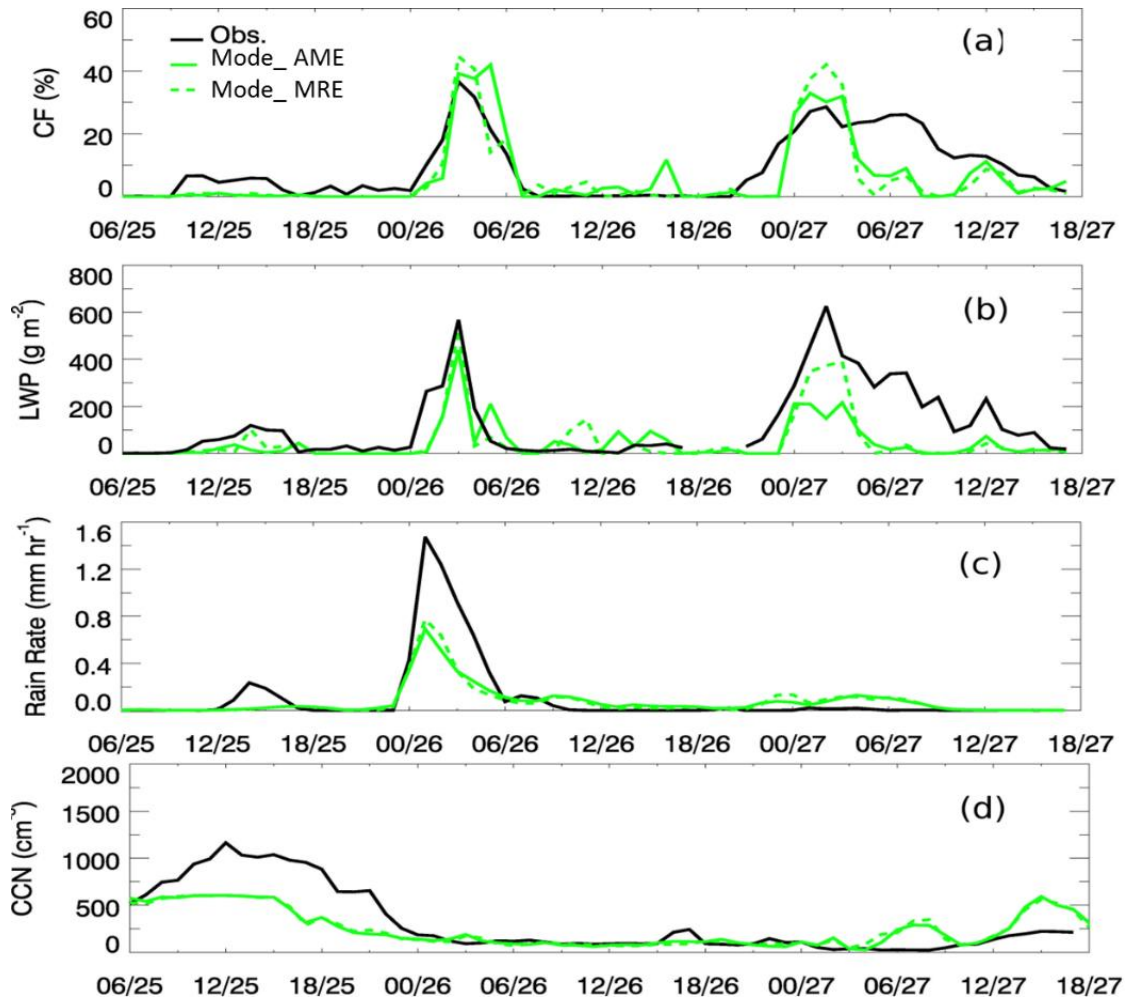
Figure 3.4 Comparisons of the Mode runs with ground observations: (a) cloud fraction, observation is from the ARM Active Remotely-Sensed Cloud Locations (ARSCL) Value-Added product; (b) liquid water path (LWP), observation is from Microwave Radiometer (MWR); (c) precipitation rate, observation is from Arkansas-Red Basin River Forecast Center (ABRFC); and (d) CCN concentration, observation is from Aerosol Observing System for simulations under three aerosol scenarios. Reprinted and adapted with permission from the American Meteorological Society (Lin et. al., 2016).

21
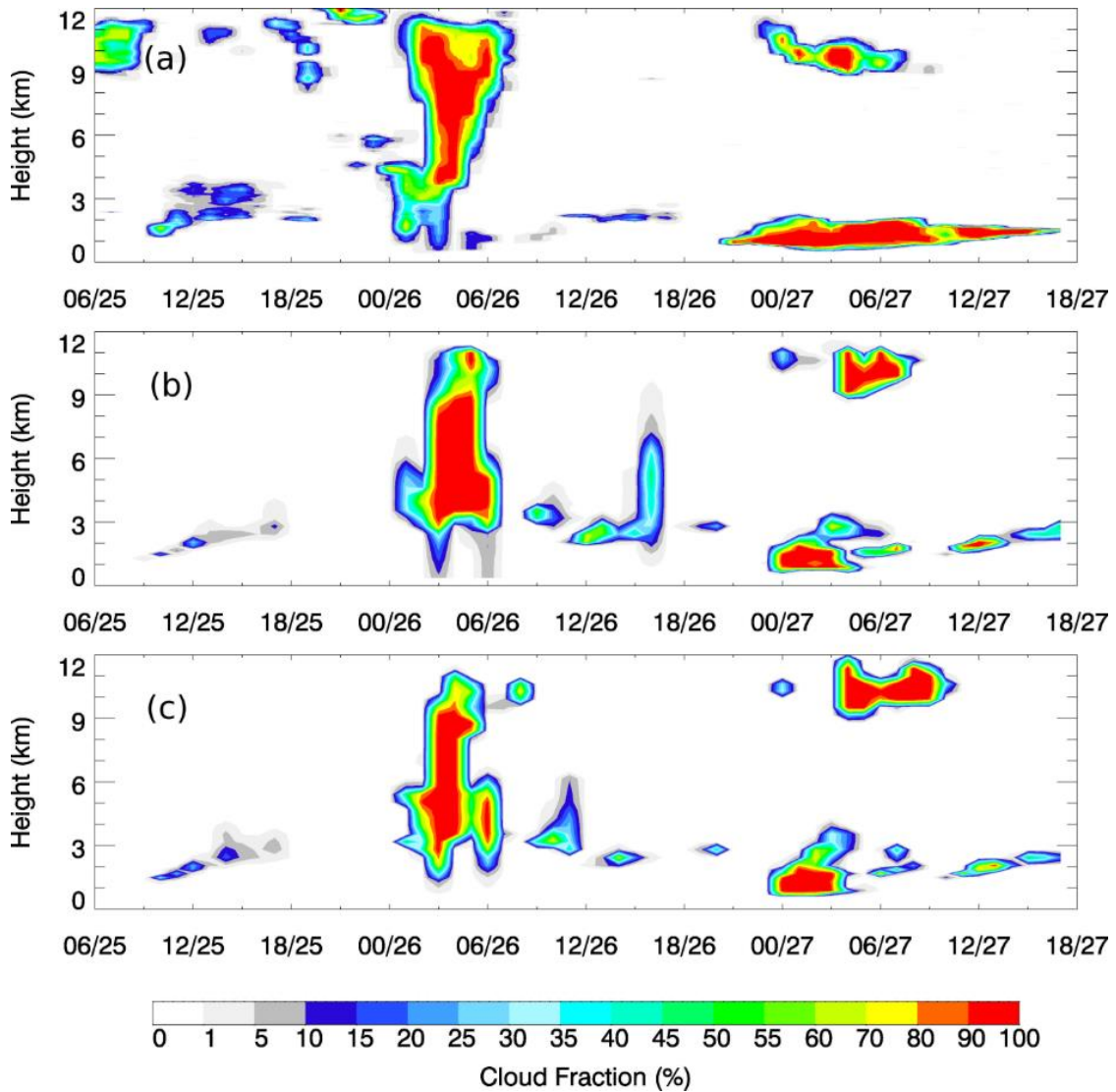
Figure 3.5 Comparison of the cloud fraction profiles between observation and simulations: (a) ARSCL measurements, (b) Mode_AME run, and (c) Mode_MRE run. The shallow cumuli on 25 May, a deep convective cloud on 26 May, and a stratus on 27 May are detected and simulated. Reprinted and adapted with permission from the American Meteorological Society (Lin et. al., 2016).

The LWP measured by the Microwave Radiometer (MWR) with an uncertainty of 20 - 30 g m^{-2} over various atmospheric conditions (Turner et al. 2007) and the precipitation rate estimated by Arkansas-Red Basin River Forecast Center (ABRFC) are also used for

model evaluation. The simulations reproduce the temporal variations of the LWP and precipitation rate from the observations (Figs. 3.4b and c). Fig. 3.4b also shows that the modeled LWP for the stratus is on average one-fourth of the observed value and Fig. 3.4c shows that the maximal precipitation rates from the simulations are one half of the observed value.

The liquid water content (LWC), cloud droplet effective radius, and droplet number concentration are measured by the Cloud and Aerosol Spectrometer (CAS) for a drop size distribution of 2 - 50 μm during the aircraft flight from 1200 to 1600 LST on 27 May 2009. The corresponding cloud quantities from the simulations are averaged over the time period of the aircraft flights and over all the cloud grids in the domain. A scaling factor is used to obtain the simulated cloud droplet effective radius from the volume mean radius since the cloud droplet effective radius is proportional to the volume mean radius according to Liu and Daum (2002). The domain means of the simulated LWC, cloud droplet effective radius and number concentration exhibit similar vertical variations with the observations, but the cloud droplet number concentration is about one-third of the corresponding airborne measured value. The discrepancy in the cloud droplet number concentrations between model and observation may be explained because of inefficient transport of aerosols into the cloud layer by the model.

Additional simulations are conducted to examine the influence of the horizontal grid spacing in resolving the boundary layer clouds by nesting down the current horizontal grid spacing (750 m) to the large eddy simulation (LES) scale (150 m). The simulations using both resolutions yield similar aerosol-cloud interactions (not shown). In addition, the droplet nucleation rate based on an explicit supersaturation in our microphysical scheme produces

23

similar vertical varying pattern as the one with a parameterized turbulence (Ghan et al. 1997; Abdul-Razzak et al. 1998).

3.2   Cloud Microphysics Response to Aerosol

Figs. 3.6 and 3.7 show the simulated cloud microphysical quantities, including the mass mixing ratio, number concentration, and effective radius of the five types of hydrometeors (i.e., cloud droplet, raindrop, ice crystal, snow, and graupel). These quantities are population-means over all the selected cloudy grids (i.e., with a mass content greater than 10^{-6} kg kg^{-1}) in the selected domain and averaged vertically and/or temporally, similarly to Fan et al. (2007a). The time periods used for the population-means in Fig. 3.7 are 0900 - 1800 CST on 25 May 2009 for shallow cumuli, 0000 - 0900 CST on 26 May 2009 for the DCC and 2100 CST on 26 May to 1800 CST on 27 May 2009 for the stratus. The error bars in Figs. 3.7 and 3.9-3.11 represent one standard deviations, which are estimated from the means of three ensemble runs. The ensembles are conducted with small perturbations in the initial temperature condition. Additionally, the statistical significance is evaluated for the differences induced by AME and ARE using the Student's t-test. For example, to determine whether the mean of a quantity of Pollu_AME run is statistically different from that of Clean_AME run, t-test for the three ensemble means from Clean_AME run and Pollu_AME run is performed at a significance level of 5%. Unless stated otherwise, all the enhancements or reductions due to AME and ARE reported here are statistically significant with a confidence level of 95%.

Figs. 3.6a and 3.7 show the responses of cloud droplets and raindrops to aerosols for the shallow cumuli. With AME only, the cloud droplets and raindrops exhibit monotonic changes with varying aerosol. For example, the cloud water mass and droplet number

24

increase by 47% and 500%, respectively, from the Clean to Pollu run. In contrast, the rain water mass and number decrease by 17% and 58%, respectively. More efficient condensation of water vapor on activated aerosols is partially responsible for the larger cloud water mass at the higher aerosol level since the condensation rate of water vapor depends on the cloud droplets number (Li et al. 2008b). Because of smaller cloud droplets under the polluted condition, the conversion from cloud droplets to raindrops via collision-coalescence process is efficiently inhibited, as reflected by the lower number of raindrops in the Pollu run (Fig. 3.7). Once formed, raindrops grow more efficiently in the polluted environment because of more cloud water to collect, explaining that the Pollu run produces a larger mean effective radius of raindrops (371 μm) than that by the Clean run (333 μm). The more efficient growth of raindrops under more polluted condition is consistent with the previous studies (Saleeby et al. 2010). AME induced changes for the shallow cumuli are statistically significant with a confidence level of 95%. For MRE runs with ARE, it is evident that at a given aerosol level both the cloud water mass and rain water mass are reduced relative to AME simulations, implying suppressed shallow cumuli by ARE. The ARE-induced suppression of the shallow cumuli is statistically significant at 95% under the polluted condition (Pollu runs).
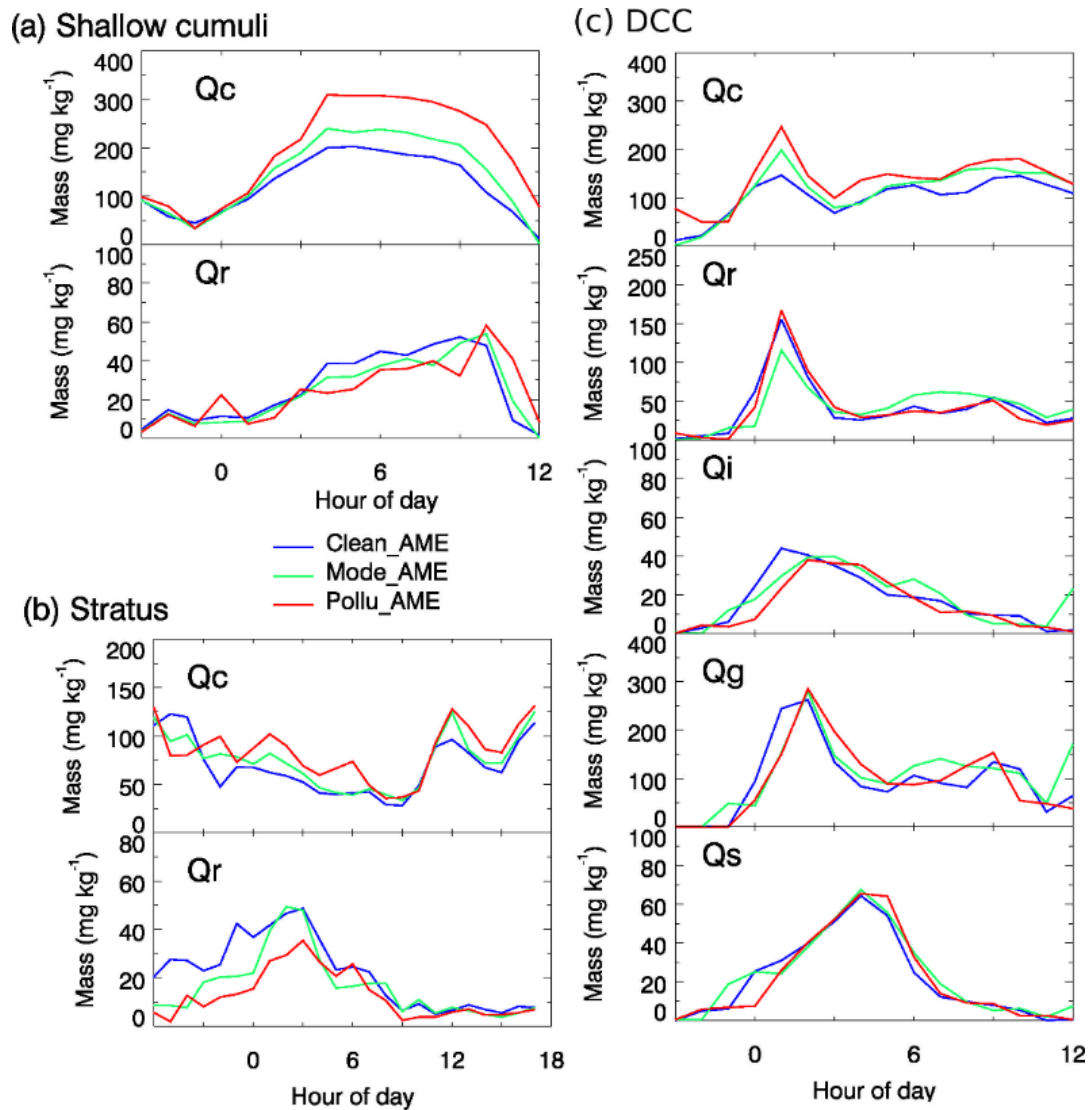
Figure 3.6 Temporal evolutions of the mass mixing ratio of hydrometeors for (a) shallow cumuli, (b) stratus, and (c) DCC under three aerosol cases, i.e. Clean_AME (blue), Mode_AME (green) and Pollu_AME (red). For shallow cumuli and stratus, only cloud and rain water (Qc and Qr) are presented. In addition to cloud and rain water, ice crystal (Qi), graupel (Qg) and snow (Qs) are also shown for DCC. Reprinted and adapted with permission from the American Meteorological Society (Lin et. al., 2016).
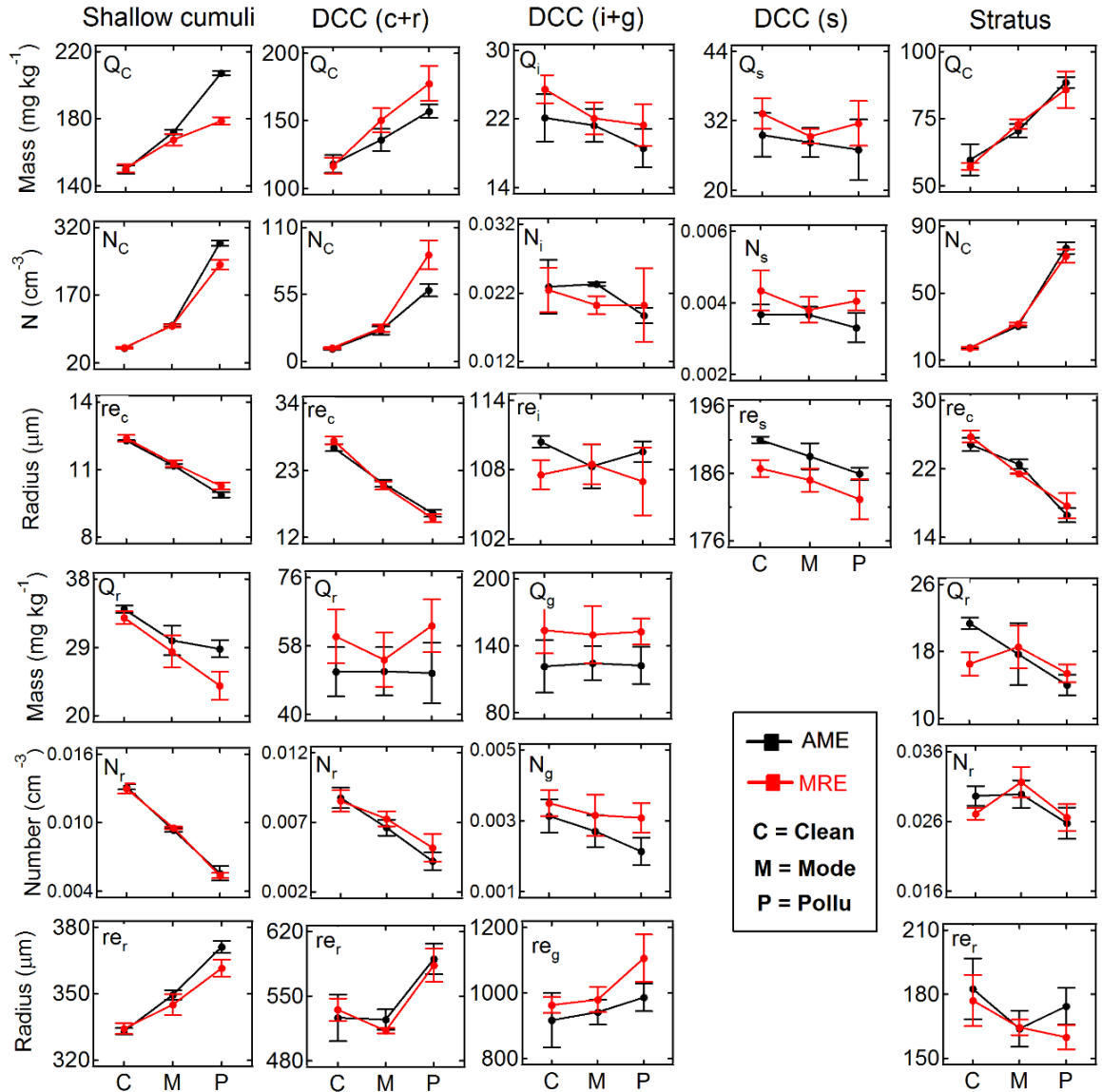
Figure 3.7 Population-mean of the cloud microphysical properties (mass mixing ratio, Q; number concentration, N; mass weighted mean radius, re). The vertical lines denote the error bars (one standard deviation), which are estimated from three ensembles conducted with small perturbations in initial temperature condition. Reprinted and adapted with permission from the American Meteorological Society (Lin et. al., 2016).

Fig. 3.6c and Fig. 3.7 (the middle three columns) exhibit the dependence of DCC microphysics on aerosol loadings. With AME only, the raindrop mass mixing ratio of the DCC is insensitive to the aerosol concentration, distinct from the shallow cumuli. In our

microphysics scheme, graupels below the freezing level are assumed to be completely melted (Li et al. 2008b), producing additional rain water to compensate the loss due to the inhibited collision-coalescence process in the polluted DCC. The time series in Fig. 3.6c show that the amount of ice-phase hydrometeors (i.e. ice, snow, and graupel) decreases initially but later increases with aerosol, suggesting a delay and a temporal shift in the ice-phase processes due to AME. This temporal shift explains the overall weak dependence of ice particles on aerosols shown in Fig. 3.7. The fact that ice particles are insensitive to aerosols for DCC in our study are different from the previous studies, which show invigorated mixed-phase processes in polluted DCCs associated with enhanced lightning activities, i.e., more aerosol leads to higher levels of ice particles (Williams et al. 1991; Nesbitt et al. 2000; Orville et al. 2001; Bond et al. 2002; Li et al. 2009; Tao et al. 2012). The minimal ice production in most polluted DCC suggests an inefficient ice nucleation. Immersion freezing is suppressed under the polluted condition, since immersion freezing is a function of the droplet size, which is smaller at a higher aerosol level (Pruppacher and Klett 1997). The inhibited ice nucleation leads to less formation of snow particles. One important mechanism to produce graupel is freezing of rain drops that are delivered to high altitudes (Li et al. 2008b), as is demonstrated by the trends of graupel mass, number, and effective radius, which are similar to the corresponding rain trends in the DCC regime (Fig. 3.7). The amount of hydrometeors is enhanced with ARE (see MRE runs in Figs. 3.6c and 3.7), suggesting an invigoration of the DCC by ARE. For example, the graupel mass is enhanced by 28% on average in MRE runs relative to AME runs.

Fig. 3.6b and in Fig. 3.7 (the fourth column) indicate that the microphysical response of cloud droplets in the stratus is similar to those of the shallow cumuli and the DCC. There

28

is a monotonic decrease in raindrop mass and number in AME runs, but a non-monotonic trend in MRE runs, suggesting that ARE has a noticeable influence on stratus rain water.

3.3   Cloud Macrophysics and Precipitation Response to Aerosol

Figs. 3.8 and 3.9 display the dependences of cloud macrophysics on initial aerosol concentrations for the different cloud regimes. In AME runs, an increase in aerosol loading leads to a reduced domain-averaged cloud fraction of the shallow cumuli and stratus but an enhanced cloudiness of the DCC (Figs. 3.8a and 3.9a). For instance, the cloud fractions for the shallow cumuli and stratus are reduced by 40% and 27%, respectively, from the Clean_AME to Pollu_AME run. In MRE runs, the cloud fraction decreases with aerosols with a larger slope for the shallow cumuli and a smaller slope for the stratus. For the DCC, the cloudiness shows a non-monotonic trend, that is, the cloud fraction decreases from the Clean to Mode run but increases from the Mode to Pollu run. For a given aerosol concentration, the DCC cloud fraction is enhanced by 13% on average in MRE simulations relative to AME simulations. Also shown in Figs. 3.8b and 3.9b, LWP for the shallow cumuli and DCC exhibits an increasing trend with increased aerosol in AME simulations. For example, from the Clean to Pollu run, LWP increases by 13 % and 35 % for the shallow cumuli and DCC, respectively. LWP for the stratus appears to be insensitive to aerosol loadings. With ARE, the LWP trends are altered for all the three cloud regimes. For example, there is little change for LWP in MRE runs during the shallow cumuli period, as aerosol increases. For the DCC and stratus, the LWP responses are non-monotonic. Similar to the cloud fraction, LWP for the DCC in MRE runs is enhanced by 22%~44 % relative to AME runs. The responses of domain-averaged precipitation rate to aerosol loading also depend on the cloud regimes (Figs. 3.8c and 3.9c). The precipitation is significantly suppressed in the

29

polluted shallow cumuli with or without ARE. There are monotonic responses in AME runs for the DCC and stratus clouds, but non-monotonic trends in MRE runs. At a given aerosol level, the precipitation rate associated with the DCC in MRE runs is considerably enhanced (on average by 30 %) compared to AME runs.

The suppressed surface precipitation (-36 %) from the Clean to Pollu run leads to more liquid water, corresponding to a moderately enhanced LWP (13%). However, the decrease in precipitation and the increase in LWP do not result in an enhancement of cloudiness but lead to a marked reduction in cloud fraction (-40%). For the stratus, the precipitation rate is reduced by 55%, while the cloud fraction decreases by 26%. These responses are contrary to the expected second aerosol microphysics effect, i.e., aerosol-induced precipitation suppression causing enhanced fractional cloudiness (Albrecht 1989). Several previous studies, e.g. Xue et al. (2006; 2008), Saleeby et al. (2010), and Saleeby et al. (2015), have suggested that the aerosol effects on droplet evaporation compete with the effects on precipitation to control warm clouds. The condensation/evaporation rate in our microphysics scheme is depended on droplet population and its mean size (Li et al. 2008b). When the cloud droplet number concentration increases with aerosols (Fig. 3.7), there is a considerable decrease of the cloud droplet size for the shallow cumuli and stratus, suggesting more efficient evaporation of cloud droplets and less efficient conversion to raindrops under polluted condition. The less cloudiness under the polluted condition of the shallow cumuli and stratus indicates that the effect of aerosol-induced enhancement of droplet evaporation dominates over the effect of aerosol-induced suppression of precipitation.
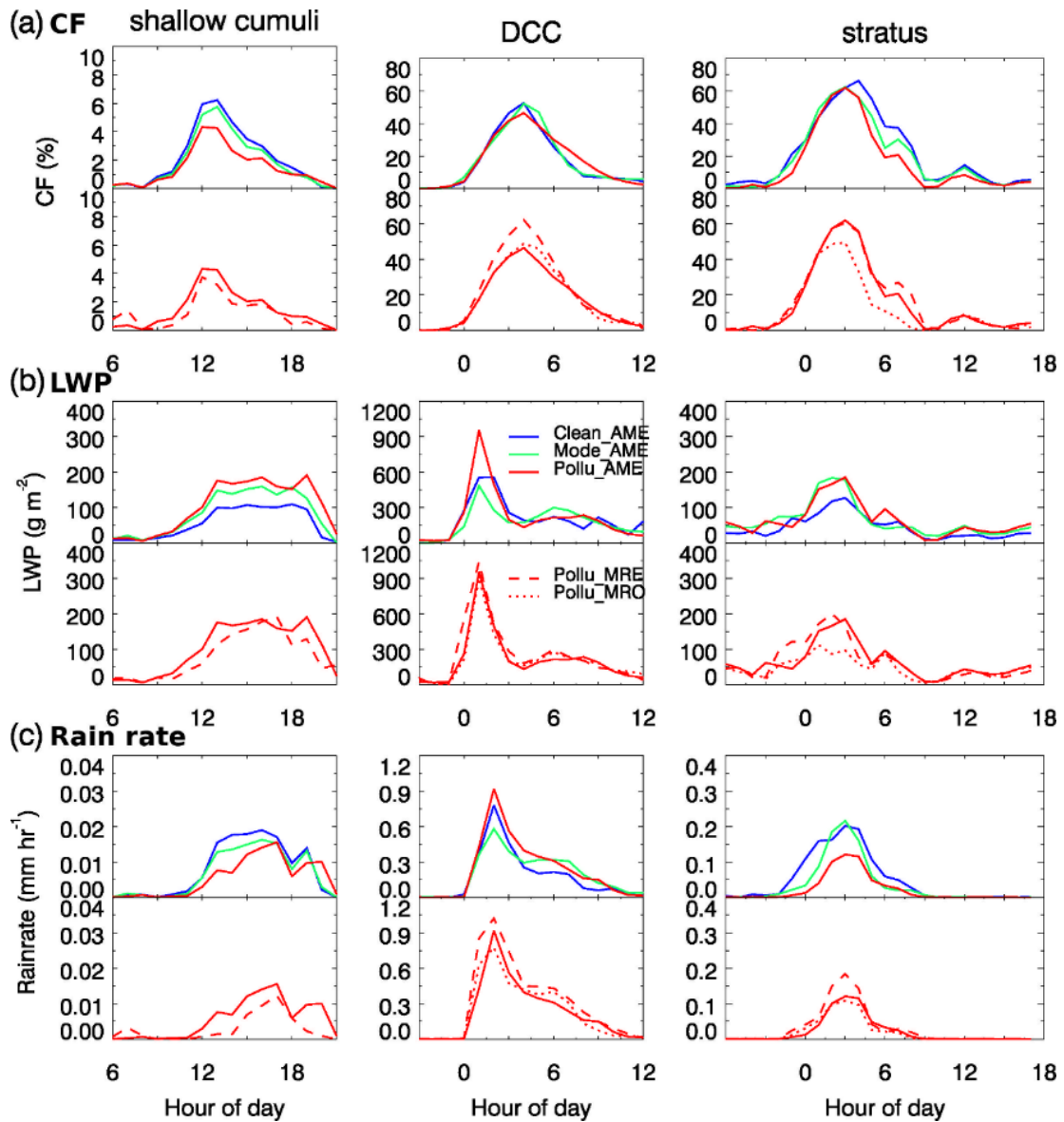
Figure 3.8 Temporal evolutions of (a) the cloud fraction, (b) liquid water path (LWP), and (c) precipitation rate under different aerosol conditions for the three cloud regimes. The left, middle, and right columns correspond to the shallow cumuli, DCC, and stratus, respectively. Reprinted and adapted with permission from the American Meteorological Society (Lin et. al., 2016).

In contrast to the shallow cumuli and stratus, a monotonic increase of the surface precipitation (34%) is evident from the Clean to Pollu run when the DCC occurs. Note that

31

the mean radius of raindrops in the DCC considerably increases when increasing aerosols (Fig. 3.7). Larger raindrops generated under the polluted condition have a higher probability of surviving evaporation when falling to the ground-level, producing more surface precipitation (Lim and Hong 2010). Since there is a notable increase in LWP (34%) for the polluted DCC, the reduction in the liquid water due to more precipitation appears to be compensated by the enhanced liquid water by more efficient condensation growth, as evident by the elevated cloud water mass under the polluted condition (Fig. 3.7). More liquid water is responsible for a higher cloudiness. The cloud fraction of the DCC is enhanced by 7% from the Clean to Pollu run (in Fig. 3.9). Since the amount of ice particles are insensitive to aerosols (Fig. 3.7), the invigoration of the DCC in terms of the enhanced LWP and precipitation (Figs. 3.8b and c and 3.9b and c) is mainly explained by the efficient condensation of cloud water. The tendency of cloudiness to the increase with aerosols for the DCC is in contrast to that for the shallow cumuli, perhaps because the DCC has a larger cloud size (a larger cloud fraction of 25%) than the shallow cumuli (a less cloud fraction of 6%), resulting in a limited entrainment drying with a larger surface-to-volume ratio (Xue and Feingold 2006). Also, cloud droplets in the DCC are on average larger than those of the shallow cumuli by four microns at a given aerosol level, leading to less evaporation and more collision-coalescence growth of droplets in the DCC.

For the comparison between MRE and AME run (Figs. 3.8 and 3.9), the cloudiness, LWP, and precipitation for the shallow cumuli are reduced with ARE. These reductions appear to be unrelated to the solar evaporation by soot-contained aerosols as implied in McFarquhar et al. (2004) study, because the mean droplet size is larger in the MRE than AME runs (Fig. 3.7). In fact, the weakened cloud microphysical response to aerosols with

32

ARE, i.e., the weakened increasing trend of the cloud droplet number concentration in the

MRE runs comparing to the AME runs (Fig. 3.7), are likely responsible for these reductions,

because of the thermodynamics and dynamics effects by absorbing aerosols. For the DCC

and stratus clouds, the variations of the cloud faction, LWP, and precipitation with aerosols

are markedly modified by ARE, since those responses are monotonic in the AME runs but

non-monotonic in the MRE runs.
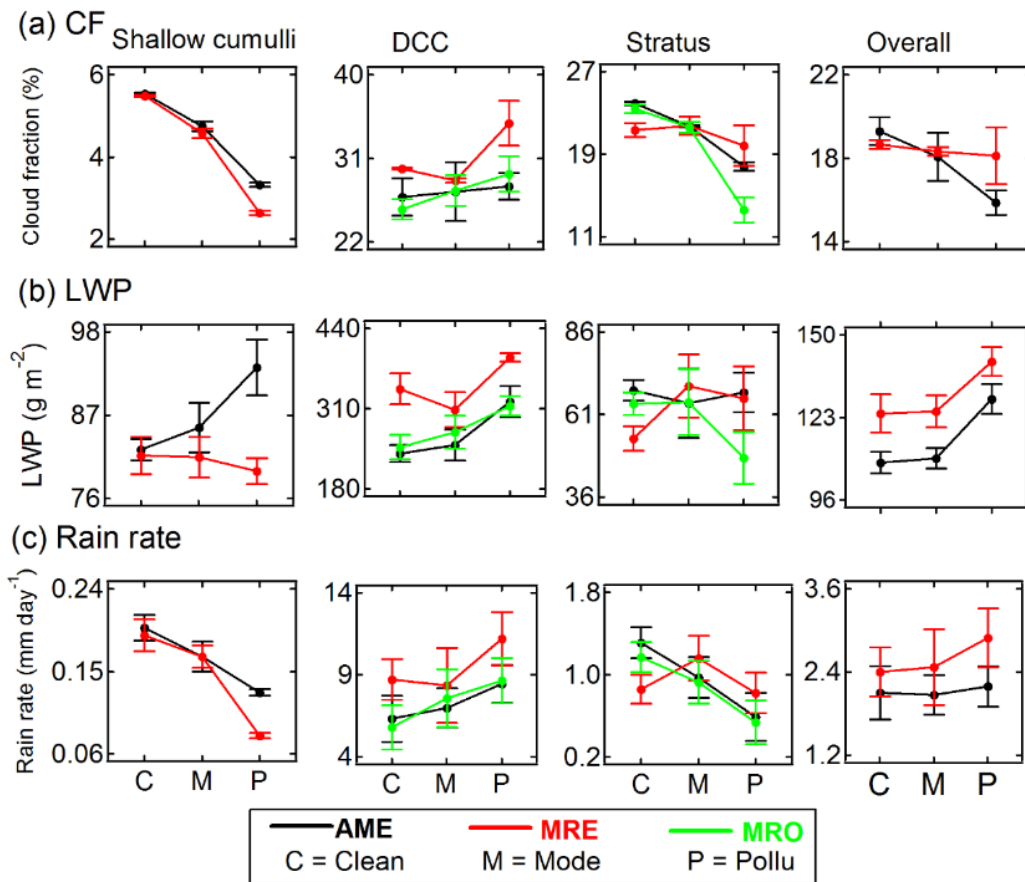
Figure 3.9 Domain-averaged cloud fraction (a), cloud column-mean of liquid water path (LWP) (b), and accumulated precipitation (c) under the Clean, Mode, and Pollu aerosol scenarios for the shallow cumuli, DCC, stratus, and overall effects (from the left to right columns, respectively). Reprinted and adapted with permission from the American Meteorological Society (Lin et. al., 2016).

Also shown in Figs. 3.8 and 3.9, the simulations without the preceding cloud-environment feedbacks (MRO) is compared to the MRE and AME runs to estimate the contribution to the latter cloud changes from ARE on the DCC and stratus clouds. The comparison of MRE and MRO to AME indicates that ARE is overestimated using the contrast between MRE and AME. For example, the cloud fraction of DCC is enhanced by 14% from Pollu_AME to Pollu_MRO, but the cloud fraction is enhanced by 24% from Pollu_AME to Pollu_MRE. An examination of MRO shows that the micro- and macrophysics of DCC in MRO run is closer to AME than to MRE. For the stratus, without the interference of development of the preceding clouds (Pollu_MRO), the polluted stratus cloud is suppressed by ARE (Fig. 3.8), similar to that of the shallow cumulus, and the microphysical responses of stratus to aerosols behave monotonically, similarly to the simulations with AME only (Fig. 3.9). For MRE, the macrophysical responses of the stratus are non-monotonic because the impacts of the preceding cloud-environment interactions are included. The nonlinear ARE on the environment through their impacts on the preceding clouds is larger than those for the DCC and stratus clouds. Since this study focuses on the aerosol effects on a continuously evolving system, ARE impacts on the preceding cloud-environment interactions are included when accessing the aerosol radiative effects on the DCC and stratus clouds.

3.4   Thermodynamic and Dynamic Feedbacks due to AME and ARE

The latent heating rates and updraft mass flux are examined to reveal the aerosol-thermodynamic and dynamic feedbacks. The vertical profiles of latent heating rates as well as the changes in net heating rate between the MRE and AME runs are shown in Fig. 3.10. The net heating rate is decomposed into the heating due to condensation (or freezing and

34

riming for DCC) and the cooling due to evaporation (or sublimation and melting for DCC). All rates are averaged over the domain and the corresponding cloud periods. The mean updraft mass flux shown in Fig. 3.11 is determined as the product of the vertical velocity and air density for all grids with a non-zero vertical velocity (Morrison 2012). The difference of the updraft mass flux between the MRE and AME runs is also presented. The horizontal lines in Figs. 3.10 and 3.11 represent the error bars calculated for one standard deviation. T-test performed at a significance level of 5% indicates that the AME on updraft mass flux for the DCC is statistically significant and the ARE on the latent heating and updraft mass flux is statistically significant for the shallow cumuli and DCC.
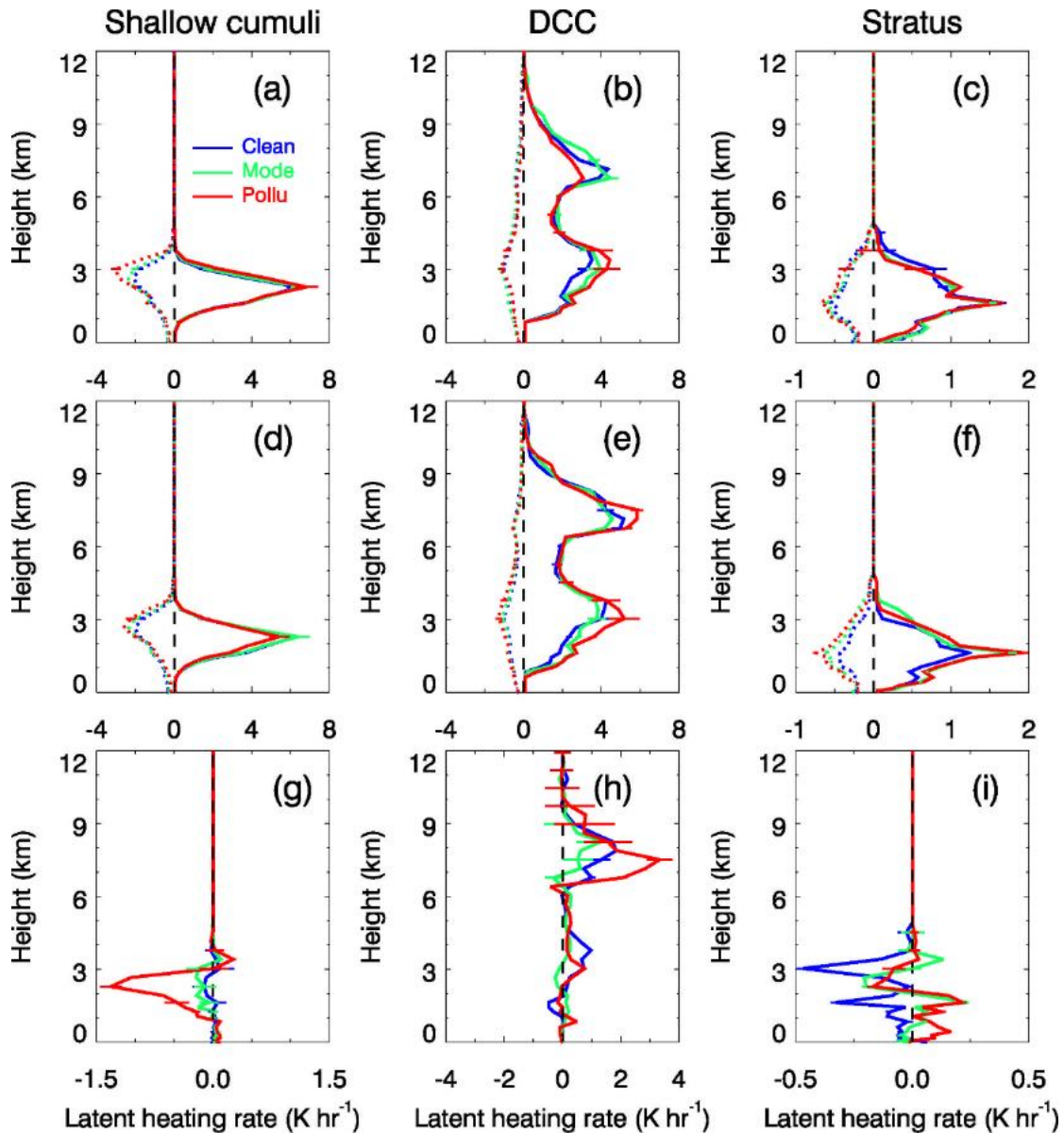
Figure 3.10 Vertical profiles of the latent heating rates for the three cloud regimes under the different aerosol scenarios. The left, middle, and right columns correspond to the shallow cumuli, the DCC, and stratus, respectively. (a)-(c) are for the AME runs, and (d)-(f) are for the MRE runs. The solid and dot lines in (a)-(f) represent the heating and cooling rates, respectively. (g)-(i) represent the difference in the net latent heating rates between the MRE and AME runs. The net heating rates are equal to the sum of the heating and cooling rates. Reprinted and adapted with permission from the American Meteorological Society (Lin et. al., 2016).

For the AME runs in Figs. 3.10a and c, the heating due to condensation is insensitive to aerosols during the shallow cumuli and the stratus periods, but the cooling due to evaporation is intensified with increasing aerosols. The stronger cooling at a higher aerosol level indicates that the more efficient evaporation due to the larger amount of smaller droplets under the polluted condition leads to the reductions in cloudiness of the shallow cumulus and stratus clouds. The enhanced cooling likely causes a stronger downward motion (Xue and Feingold 2006), further suppressing the two cloud regimes. However, the corresponding updraft mass fluxes are insensitive to aerosols (Figs. 3.11a and c), perhaps because of litter changes in the latent heat released. The response of the heating during the DCC period depends on the altitude (Fig. 3.10b), i.e., the heating increases monotonically at low altitudes (below 4 km) but non-monotonically at high altitudes (above 6 km). The increase in heating at low altitudes suggests more efficient condensation in the polluted DCC, as reflected by the higher cloud water mass of the DCC in the Pollu run (Fig. 3.7). As a result, the convection for the polluted DCC is invigorated (Fig. 3.11b), leading to the increases in cloudiness, LWP, and precipitation (Fig. 3.8 and 3.9). Above 6 km, the increasing trend in mass flux is inconsistent with the decreasing trend in latent heating, probably due to the continuous influence of the invigoration of updrafts at lower atmosphere (below 4 km). Also note that the cold pools exist just below the DCC (the peaks of the cooling rates in Fig. 3.10b), corresponding to the evaporative cooling induced by precipitation. Those cold pools are important for cloud maintenance (Tao et al. 2007; Grant and van den Heever 2015). For the DCC case, the cold pools are insensitive to aerosols, suggesting that the aerosol-cold pool interaction is not a key factor controlling the DCC characteristics in this study.
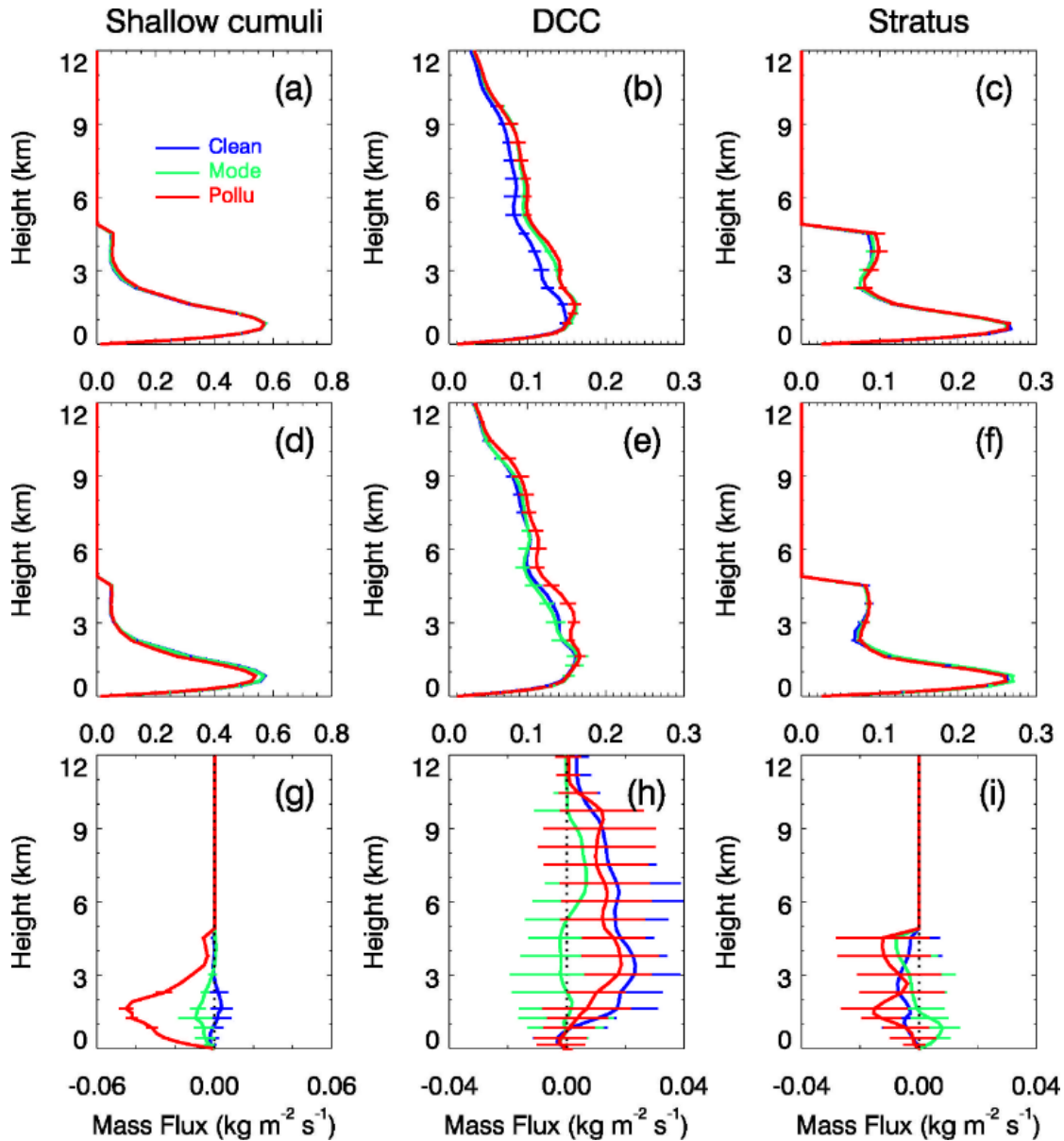
Figure 3.11 Vertical profiles of the updraft mass flux (vertical velocity > 0 m s⁻¹) for the three cloud regimes under the different aerosol scenarios. The left, middle, and right columns correspond to the shallow cumuli, DCC, and stratus, respectively. (a)-(c) are for the AME runs, (d)-(f) are for the MRE runs, and (g)-(i) are for the differences in the mass flux between the MRE and AME runs. Reprinted and adapted with permission from the American Meteorological Society (Lin et. al., 2016).

With ARE, the tendency of the cooling to increasing aerosols for the shallow cumuli

is weakened, indicating less efficient evaporative cooling in the MRE runs. The

microphysical features (Fig. 3.7) also show that, at a same aerosol level, droplets in the MRE runs are on average larger than those of the AME runs, leading to a reduced surface-to-volume ratio of droplets in the MRE runs and suppressed evaporation. The heating in the MRE runs exhibits a weak decreasing trend (Fig. 3.10d). Correspondingly, the updraft mass flux decreases with aerosols (Fig. 3.11d). By contrasting the ARE and AME runs, the differences in the net heating rate as well as the updraft mass flux tend to be more negative under the polluted condition (Figs. 3.10g and 3.11g), suggesting that the reduced latent heat and suppressed updraft by ARE are more significant at a higher aerosol level. The suppressed updraft results in the reduced cloud fraction, smaller LWP and less precipitation for the shallow cumuli (Fig. 3.9).

The convection of DCC in the MRE runs shows a non-monotonic response to aerosols (Fig. 3.11e), corresponding to the non-monotonic trend of the latent heating (Fig. 3.10e). The non-monotonic responses of the latent heating and convection lead to the non-monotonic responses of cloudiness, LWP, and precipitation shown in Fig. 3.9. In Figs. 3.10h and 3.11h, the differences in the net latent heating rate and updraft mass flux between MRE and AME runs are positive, representing a stronger convection in the MRE than AME runs. These positive changes explain the invigorated DCC, i.e. the enhanced cloudiness, LWP and precipitation shown in Fig. 3.9. For the stratus, the aerosol-induced increase in the cooling rate competes with the increase in the heating rate, and both control the updraft responses to aerosols shown in Figs. 3.11c and f. As a result, the differences in the net latent heating rate and updraft mass flux between the MRE and AME runs are either positive or negative for the different aerosol levels (Figs. 3.10i and 3.11i), resulting in the complexity of the aerosol-stratus cloud interactions with ARE as shown in Figs. 3.7 and 3.9.

39

The modifications of the thermodynamic and dynamic conditions by ARE are examined by contrasting the polluted MRE and AME runs in terms of the temporal evolution of the various environmental parameters, including the radiative heating rate, temperature, relative humidity, cloud water content, equivalent potential temperature, updrafts and downdrafts as shown in Fig. 3.12.

As shown in Fig. 3.12a, the positive changes in the heating rate by shortwave radiation are observed repeatedly from 0600 to1800 LST each day, representing a significant absorption of solar radiation by soot-contained aerosols in the MRE runs. The peak value of the heating rates for the Pollu case with ARE is 2.9 K day^{-1}, by 0.7 K day^{-1} higher than that of the Pollu case without ARE. During the shallow cumuli period (i.e., the daytime on 25 May), the solar absorption causes warming in the low troposphere, as reflected by the positive changes in temperature around at 1-3 km in Fig. 3.12b, and cooling at the surface, as reflected by the negative changes in temperature near the surface. As a consequence, the atmosphere is stabilized, evident by the negative changes in the equivalent potential temperature in Fig. 3.12e. The more instable atmosphere explains the weaker updrafts and downdrafts during the shallow cumuli period in Figs. 3.12f and g as well as the smaller updraft mass flux for the polluted condition in Fig. 3.11g. The relative humidity is considerably reduced (Fig. 3.12c) because less moisture is transported to the cloud region due to the weakened updraft. As a result, the shallow cumuli are suppressed by ARE, as reflected by a lower cloudiness and smaller LWP (Fig. 3.9) as well as the negative changes in the cloud water content (Fig. 3.12d).
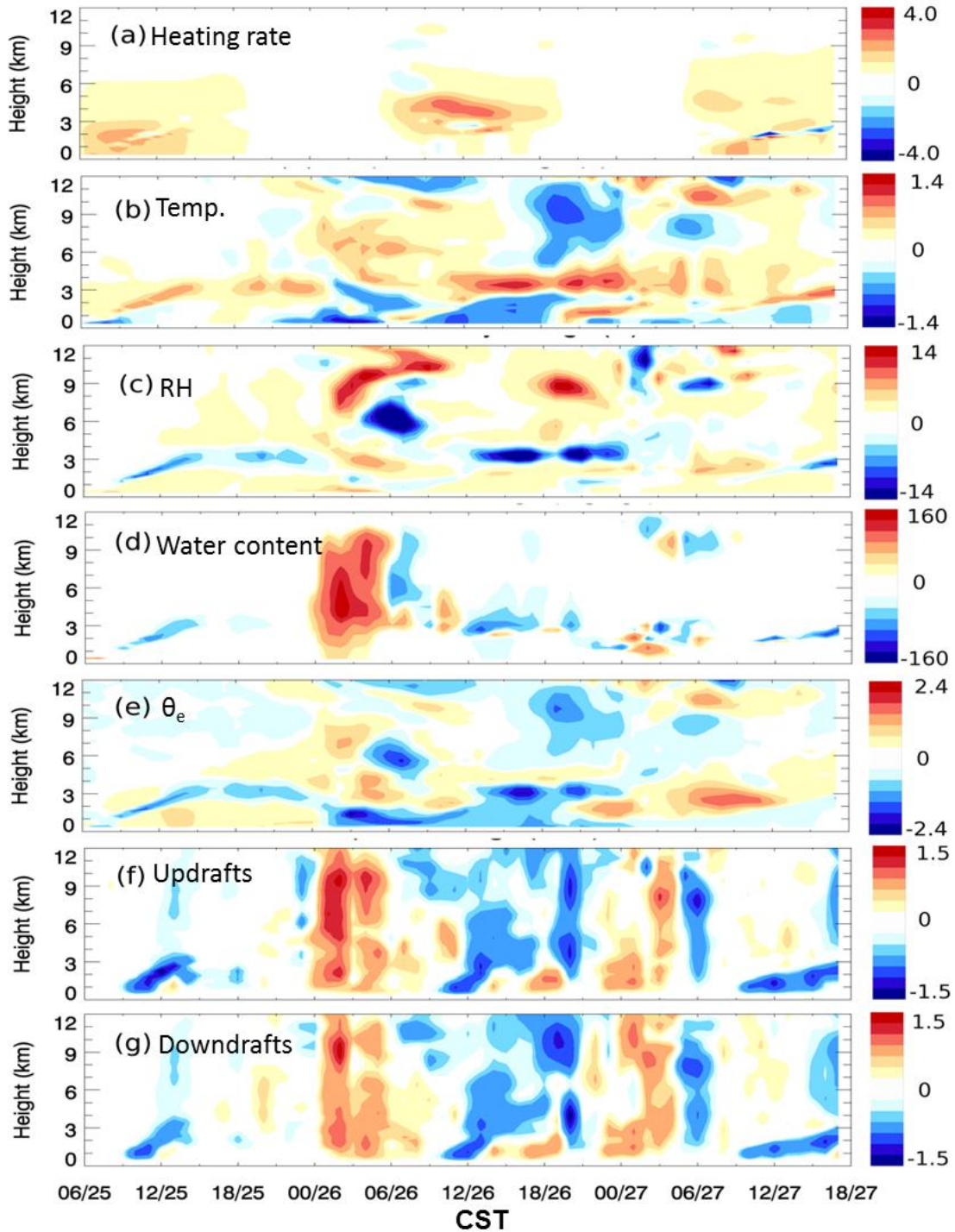
Figure 3.12 Temporal evolution of the differences in (a) the heating rate by shortwave radiation (K day^{-1}), (b) temperature, Temp. (K), (c) relative humidity, RH (%), (d) cloud water content (mg kg^{-1}), (e) equivalent potential temperature, θ$_e$ (K), (f) updrafts (m s^{-1}), and (g) downdrafts (m s^{-1}) between the Pollu_MRE and Pollu_AME runs (i.e., MRE - AME). Reprinted and adapted with permission from the American Meteorological Society (Lin et. al., 2016).

41

The positive changes in the cloud water content during the DCC period (Fig. 3.12d) are associated with the enhanced atmospheric instability. Consistently, the positive changes in the equivalent potential temperature are shown just before the DCC formation (Fig. 3.12e), suggesting a more unstable atmosphere with ARE. The increased instability as well as the invigorated convection (Fig. 3.12f and g) in the early morning on 26 May are possibly triggered by the heating effect of absorbing aerosols during the daytime of 25 May. Also, note that the positive changes in relative humidity during the DCC period suggest more water vapor transported to the upper troposphere because of the stronger updrafts (Figs. 3.12f and 3.11h). As a result, the cloud microphysical processes in DCC, such as the graupel formation and growth, are strengthened by ARE (i.e., from the enhanced graupel mass, number and size from the AME to MRE runs in Fig. 3.7), leading to the higher LWP and more precipitation (Fig. 3.9). The underlying mechanism for the invigorated DCC in our study is similar to the "aerosol-enhanced conditional instability" mechanism, which has been demonstrated by Grant and van den Heever (2014) and Fan et al. (2015). For example, Fan et al. (2015) has documented that the daytime convection is suppressed with increased atmospheric stability by light absorbing aerosols, resulting an excess moist air mass transported downwind at night and causing stronger convection at the downwind area as well as more heavy precipitation. The difference between this study and Fan et al. (2015) is that the aerosol-enhanced conditional instability occurs at the downwind area in Fan et al. (2015) but at the source region in this study.

The interactions between aerosols and the stratus are complicated due to the ARE impacts on the environment feedbacks of the shallow cumuli and DCC. Under the polluted condition, the increased cloud water content of the nighttime stratus (from 0000 to 0600 LST

42

on May 27) is explained by the enhanced instability and invigorated convection (Figs. 3.12e, f, and g). The daytime stratus (from 0900 to 1800 LST on May 27) tends to be suppressed by aerosol heating, as reflected by the negative changes in the cloud water content and vertical velocities (Figs. 3.12d, f, and g).

3.5   The Overall Effects of Aerosols on the Cloud Complex

The overall aerosol effects on the evolving cloud complex are shown in Fig. 3.7 in terms of the domain-averaged cloud fraction, LWP, and rainfall rate averaged over the entire cloud period. It is evident that the aerosol net effects on the cloud complex are noticeably different from the aerosol effects on the individual cloud regimes. For instance, the mean cloud fraction over all the three cloud regimes slightly decreases from 19% (19%) to 16% (18%) from the Clean to Pollu runs with AME (MRE). The overall LWP and rainfall rate increase with aerosols for the AME and MRE runs. These trends of the evolving cloud complex are distinct from those of its individual cloud regime, suggesting that the aerosol effects associated with an individual cloud regime likely offset or compensate with each other, via a buffering effect (van den Heever et al. 2011). The overall aerosol effects for the 3-day simulation are statistically significant (i.e., the relatively small error bars in Fig. 3.7), in contrast to the weak effects by van den Heever et al. (2011) with a much longer simulation (40-day) performed. Since the overall response of the cloud properties to aerosols for the evolving cloud complex is distinct from those of its individual cloud component, it is necessary to evaluate the long-term response of the various cloud types when assessing the aerosol direct and indirect radiative forcings.

3.6   Summary

The aerosol microphysical and radiative effects on an evolving continental cloud complex occurring from 25 May to 27 May 2009 during the DOE ARM RACORO field campaign are investigated. The TAMU-WRF model with a two-moment bulk microphysics by Li et al. (2008b) and a modified Goddard radiation scheme by Fan et al. (2008) is employed to investigate the AME and ARE. The activation of aerosols to CCN is estimated by assuming a chemical composition of either pure ammonium sulfate or ammonium sulfate containing a small fraction (5%) of black carbon when evaluating the aerosol radiative effect. Two typical boundary layer clouds (shallow cumuli and a one-day persisting stratus) and a DCC formed associated with a pre-frontal convective line are simulated in this cloud complex. Comparison of the cloud fraction between simulations and measurements shows that the temporal evolutions of cloud fractions of the different clouds and the transition of the cloud types at the SGP central facility are reproduced in the simulations, but the modeled stratus is discontinuous, and the cloud fractions of the shallow cumuli and the stratus are underestimated. The simulated LWP and precipitation generally agree temporally with the observations, but the simulations underestimate the magnitude of LWP for the stratus and peak value of precipitation for the DCC.

The simulated mass and number concentrations and effective radii of cloud droplets and raindrops for all the three cloud regimes exhibit overall monotonic responses to initial aerosol concentrations with or without ARE. A higher aerosol level yields more numerous CCNs for water vapor to condensate, but inhibits the conversion of cloud droplets to raindrops, explaining the enhancement of cloud droplet nucleation and the suppression of raindrop formation. The overall change in ice water content induced by aerosols is

insignificant, but the onset of ice formation was delayed in AME. The comparison of AME and MRE simulations implies that at a given aerosol level shallow cumuli are suppressed while the DCC is invigorated with ARE. The microphysical response of raindrops for the stratus behaves differently with ARE, suggesting that ARE has significant impacts on the stratus rain water. Note that ARE discussed in this study for the DCC and stratus clouds also contains the impacts of the environmental feedbacks through ARE influences on the preceding cloud regimes.

The responses of the cloud fraction, LWP, and precipitation to aerosols depend on the cloud regimes. The cloud fraction for shallow cumuli and the stratus decreases with aerosol due to AME, indicating that the aerosol-induced suppression of precipitation is dominated by aerosol-induced intensification of droplet evaporation, as suggested by Xue el al. (2008). For the DCC, the increases in cloudiness, LWP, and precipitation with increasing aerosols are due to more efficient condensation and less efficient evaporation, corresponding to enhanced latent heating at low altitude and updraft mass flux. ARE tends to reduce cloudiness and precipitation associated with shallow cumuli, likely because of a weakened cloud microphysical response to the changes in aerosol concentration with ARE. ARE exhibits a remarkable influence on the trends of cloud fraction, LWP, and precipitation for the DCC and stratus clouds, since their responses to aerosol are monotonic with AME only but non-monotonic with both AME and ARE. Because there are less cloudiness and smaller LWP for the two simulated boundary layer clouds under the polluted condition, the loss dominates over generation for the condensate mass. In comparison, Khain et al. (2008) have found that both the generation and the loss of the condensate mass can be enhanced in the polluted condition of warm cloud-base clouds.

45

Simulations with and without ARE under the polluted condition show distinct characteristics of the cloud micro- and macrophysics, because of the changes in atmospheric instability and thermodynamics caused by ARE. Because of the radiative heating from soot particles, the convection strength and RH are both reduced during the daytime. Subsequently, cloud amounts of the shallow cumuli are decreased in ARE. The increasing atmospheric instability by absorbing aerosol alters the temperature and moisture conditions during daytime and further leads to an enhanced atmospheric instability and excess moisture at night and a favorable condition for the nighttime DCC formation, similar to the "aerosol-enhanced conditional instability" mechanism previously demonstrated by Grant and van den Heever (2014) and Fan et al. (2015).

The buffering effect of one cloud regime on another makes the overall aerosol effects of the cloud complex distinctly different from any of the individual cloud types, consistent with van den Heever et al. (2011). Hence, the aerosol-cloud interaction for the diverse cloud regimes and their transitions throughout the cloud lifecycle needs to be evaluated to assess the overall aerosol direct and indirect radiative forcings on regional and global climate. Future statistical study on long-term observations and/or modeling simulations is also necessary to more accurately examine the comprehensive aerosol effects on clouds and precipitation. Also, case studies associated with various synoptic setups need to be selected to improve the representation of aerosol-cloud interactions and test the robustness of conclusions drawn from this work.

4. FORMATION, RADIATIVE FORCING, AND CLIMATIC IMPLICATIONS OF SEVERE REGIONAL HAZE IN CHINA

To better understand the formation and evolution of severe haze in China as well as the regional climate effects under extremely hazy condition, two typical severe haze episodes occurring in fall of 2013 in Beijing, China were selected as case studies, in which the satellite observation and field measurements were examined and numerical modeling studies were performed on interactions between severe haze and PBL as well as aerosol/BC radiative forcing response using WRF model coupled with an explicit aerosol radiative module (Fan et al. 2008; Wang et al. 2014a). To what extent the BC aging can affect the haze-PBL interactions and its contribution to net aerosol radiative forcing during severe haze periods are also studied by conducting additional simulations with and without consideration of BC aging.

4.1 Data and Modeling Design

The observed aerosol optical depth (AOD) in this study is derived by combining the Moderate Resolution Imaging Spectroradiometer (MODIS) measurements of Aqua and Terra based on the equal-weighted mean method to increase the spatial coverage (Levy et al. 2009). MODIS data was downloaded at http://giovanni.gsfc.nasa.gov/aerostat/. The Terra visible images were obtained at https://worldview.earthdata.nasa.gov/. The one-year $PM_{2.5}$ concentration in Beijing is obtained from the Embassy of United States, Beijing, China (http://www.stateair.net/web/historical/1/1.html). PBL height in is based on reanalysis data of MERRA-2. The typical severe haze days selected for analysis are the days with a daily $PM_{2.5}$ concentration greater than 200 μg m^{-3}, and the typical clean days are the days with a

daily $PM_{2.5}$ concentration smaller than 30 μg m^{-3}. The PBL height and $PM_{2.5}$ surface concentration at 14:00 Beijing time (BJT) each day in 2013 are used for analysis. All the raining days are filtered out. The SSR data are based on satellite observation (Tang et al. 2016b) and obtained from http://www.tpedatabase.cn, also averaged over all the severe haze days in 2013 in Beijing.

The field campaign conducted at Beijing from 25 September to 14 November in 2013 to characterize Beijing severe haze events has been reported by Guo et al. (Guo et al. 2014). Briefly, the simultaneous measurements of gaseous species and aerosol properties were performed in the campus of Peking University, an urban site located in northwestern Beijing. A suite of state-of-the-art instruments were deployed during the campaign, including a tapered element oscillating microbalance (TEOM) for $PM_{2.5}$ mass concentration, a combined nano-scanning mobility particle sizer (SMPS) and standard SMPS for the particle size distribution, an Aerodyne high-resolution time-of-flight aerosol mass spectrometer for chemical composition of submicron particles, and a single-wavelength (670 nm) Thermo multiangle absorption photometer for black carbon. These measurements provide $PM_{2.5}$ concentration, aerosol chemical composition and gaseous data as well as the aerosol initial conditions as input for numerical simulation. $PM_{2.5}$ data for Baoding and Shijiazhuang cities are reprinted from Li et al. (Li et al.).

Haze-PBL interactions and regional climate effects of typical Beijing severe haze events are examined using the WRF model. A 100×100 grids domain with a horizontal grid spacing of 2 km is set up to cover the Beijing urban region. Initial and boundary meteorological conditions are generated from six-hourly NCEP FNL (Final) Operational Global Analysis (1°× 1°). No convective parametrization is applied for the simulations.

We perform simulations under the different aerosol pollution conditions, including clean and severe haze cases. The two most hazy days (28 September and 5 October 2013, respectively) during the two severe haze episodes (EP1 and EP2) are selected for case studies, and the simulations on these two days are referred as HAZE cases. Core-shell configuration is assumed for BC and non-BC (pure ammonium sulfate only) mixing in aerosols for HAZE cases. The two days just before the two severe haze episodes started (25 September and 2 October 2013) are simulated for comparison with HAZE cases, representing the typical clean condition, thus referred as CLEAN cases. The aerosol initial and boundary conditions for all the simulation in this study are based on measurements during the 2013 Beijing field campaign (Fig. 4.1). We take aerosol measurements on 25 September and 2 October 2013 as input for CLEAN cases and 28 September and 5 October 2013 for HAZE cases. Therefore, according to the measurements, the aerosol surface number and mass concentration for modeling initialization are 3.5×10^4 cm^{-3} (3.6×10^4 cm^{-3}) and 10 μg m^{-3} (11 μg m^{-3}) for CLEAN case of EP1 (EP2) and 1.7×10^4 cm^{-3} (1.8×10^4 cm^{-3}) and 280 μg m^{-3} (310 μg m^{-3}) for HAZE case of EP1 (EP2), respectively. Also based on measurements, the BC percentage in total aerosol mass is set as 10.0% and 6.0% for Clean and HAZE cases, respectively. There is few cloud on the days we selected for numerical simulations, therefore the aerosol indirect effects are ruled out.
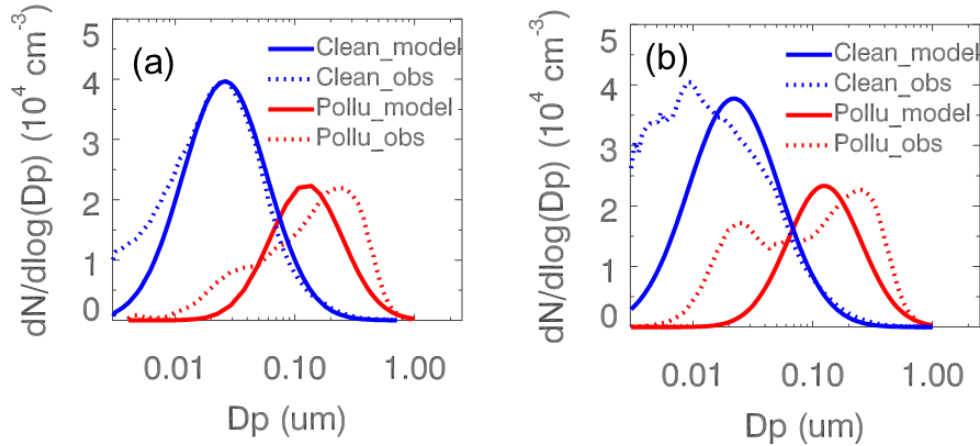
Figure 4.1 Aerosol size distributions from observations and for modeling inputs. Aerosol size distributions taken from measurements (a) on 25 and 28 September and (b) 2 and 5 October, 2013 (blue and red dot lines, respectively) and used as inputs for the simulations of Clean and HAZE cases (blue and red solid lines, respectively).

To assess the role of BC in suppression effect of severe haze on PBL development and aerosol radiative forcing during severe haze episodes, we perform another sets of simulations under severe haze condition but excluding BC effects (referred as non-BC case), in which BC radiative effect is turned off by assigning zero value to both the real and imaginary parts of BC refractive index. By doing so, SSA in non-BC case is nearly unity. To isolate the BC aging effects, additional sets of simulations are performed under severe haze condition but with "fresh" BC (referred as "fresh" BC cases), in which the BC core is not imbedded in the non-BC shell and its optical properties is calculated separately by Mie theory calculation code. In "fresh" BC case, the lensing effect due to the coating during aging process is excluded, but the restructuring effect induced by aging is taken into account partially since the BC core is assumed spherical and already in compact status. In contrast, it is reasonable that BC components in HAZE cases is treated as in aged status, considering

50

the full aerosol components (both BC and non-BC) and core-shell configuration in HAZE cases. Therefore, we also refer HAZE cases as "aged" BC cases when discussing the role of the BC aging. Summaries for all the simulation cases are listed in Table 4.1.

One possible hypothesis to account for the underestimation in the absorbed AOD and the directive radiation forcing of BC in current models is the underestimation in the coating-enhancement of ambient BC absorption (Bond et al. 2013; Gustafsson and Ramanathan 2016). Peng et al. (Peng et al. 2016) have reported the absorption of aged BC aerosols is enhanced by 2.4 relative to the fresh BC based on the chamber experiments during hazy days in Beijing, offering a possible reconciliation of previous reports on the coating-enhancement of BC aerosols (Gustafsson and Ramanathan 2016). To address the concern that the coating-enhancement of ambient BC absorption is underestimated in current models (Bond et al. 2013; Gustafsson and Ramanathan 2016) and thus the potentially biased radiative effects of aged BC, additional simulations are conducted (referred as Haze2.4) by constraining the enhancement of mass absorption cross section of BC (E_{MAC-BC}) to an experimental value derived from the chamber study during severe haze days in Beijing by Peng et al. (Peng et al. 2016). Though the E_{MAC-BC} derived from HAZE case in which the core-shell configuration is used is slightly lower than 2.4 reported by Peng et al. (Peng et al. 2016), the comparison between Haze and Haze2.4 cases (not shown) suggests that there is little difference in thermodynamic, dynamic and radiative budget. It is also evident that constraining E_{MAC-BC} to experimental value does not alter haze-PBL interactions significantly.

The modeling results are validated by several sources of observations. The simulated temperature and relative humidity are in good agreement with sounding data in terms of

51

vertical variations (Fig. 4.2). The maximal PBL height derived from HAZE case of EP1 is comparable to the magnitude of available ceilometer observations (Fig. 4.7). The simulated AOD at 550 nm is 0.05 and 3.6 for 25 and 28 September 2013 and 0.04 and 2.0 for 2 and 5 October 2013, qualitatively consistent with Aerosol Robotic Network (AERONET) measurements at Beijing (Table 4.1). The one-day accumulated surface solar radiation on 28 September is 9.2 MJ m^{-2} in simulation, comparable to the ground-based measurement of 10.6 MJ m^{-2} (Table 4.1).
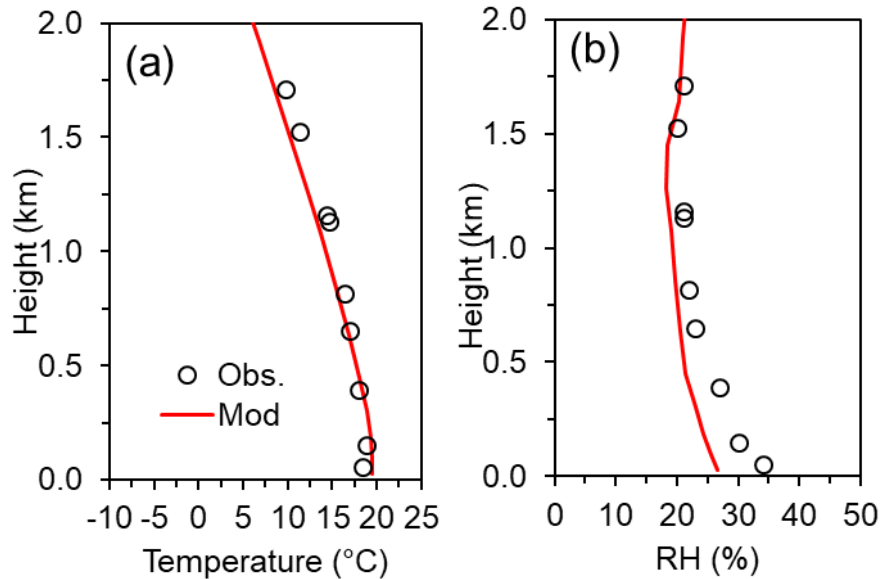
Figure 4.2 Comparison of model simulations with sounding observations. (a), temperature profile at 12Z 28 September 2013. (b), relative humidity profiles at 12Z 28 September 2013. Black open cycles denote sounding profiles and solid lines denote the simulations.

Table 4.1 Summary of simulation cases and comparisons between measurements and simulation for AOD and accumulated surface solar radiation during haze EP1/EP2.

Case names	Description	AOD	SSR (MJ m^{-2})
CLEAN case	The clean days just before the two selected haze episodes start (25 Sep. and 2 Oct., 2013), with daily mean PM$_{2.5}$ < 30 μg m^{-3}.	-	-
HAZE case or "aged" BC case	The most polluted days during the selected haze episodes (25 Sep. and 2 Oct., 2013), with daily mean PM$_{2.5}$ > 200 μg m^{-3}. The core-shell configuration is assumed for mixing BC and non-BC component. The BC core is assumed as a sphere. HAZE cases are also referred as "aged BC" cases since the lensing effect due to BC aging is already treated by core-shell configuration assumption.	3.6/2.0	9.2/11.3
non-BC case	HAZE cases without BC by turning off BC radiative effects.	-	-
"fresh" BC case	HAZE cases with "fresh" BC, in which the BC core is assumed as a sphere but not imbedded in the non-BC shell. The optical properties of the BC core are calculated separately by use of Mie theory calculation code. To do so, the lensing effect is not considered in the "fresh" BC case.	-	-
Observations	HAZE case for EP1/EP2: Sep. 28/ Oct. 5, 2013	3.5/2.4	10.6/9.8

Note: The observed AOD is from AERONET (http://aeronet.gsfc.nasa.gov/).

In addition to the numerical model simulations, we also employed an empirical equation derived by Nozaki (1973) to examine the sensitivity of RH to PBL height based on observations. The equation is shown below:

$$H = \frac{121}{6}(6 - P)(T - T_d) + \frac{0.169P(U_Z + 0.257)}{12f \ln Z/z_0}$$

where H, T, T_d, and U_z represent the PBL height, surface air temperature, surface dew point, and mean wind speed (m s^{-1}) at height of Z (Z=10 m), respectively. f and z_0 are the Coriolis parameter (s^{-1}) and surface roughness length (0.5 m in this study), respectively. P is the Pasquill stability level, classified as six categories from very unstable (A), moderately unstable (B), slightly unstable (C), neutral (D), slightly stable (E) to moderately stable (F) (Pasquill 1961). To relate RH with PBL height, Tie et al. (2017) modified Nozaki's equation using (100- RH)/5 to replace (T-T_d) based on Wallace and Hobbs (2005). The measured wind speeds are used in the calculation. For the severe haze events, the atmosphere is extremely stable, and hence the Pasquill stability levels are set as 5, respectively. The PBL height for "haze" cases are based on ceilometer observations, and then we increase the observed PBL height by 200 m as input for the "clean" cases.

4.2 Aerosol Pollution Characteristics During Severe Haze Episodes

A field campaign conducted in Beijing from 25 September to 14 November 2013 reveals that severe haze events frequently occurred over the North China Plain (NCP) during this period, associated with clear periodic cycles of PM pollution. The maximal mass concentration of PM$_{2.5}$ (particular matter with aerodynamic diameter less than 2.5 microns) exceeded 200 μg m^{-3} for each severe haze event at three megacities, including Beijing, Baoding, and Shijiazhuang, across the NCP (Figs. 4.3a-c). The PM$_{2.5}$ concentrations at the three megacities present a rapid accumulation at the same time when haze formed, with similar peak timing and magnitudes among different cities on the hazy days. The temporal synchronization and the comparable level of PM pollution among different cities suggest the clear regional feature of severe haze occurring over NCP.

54
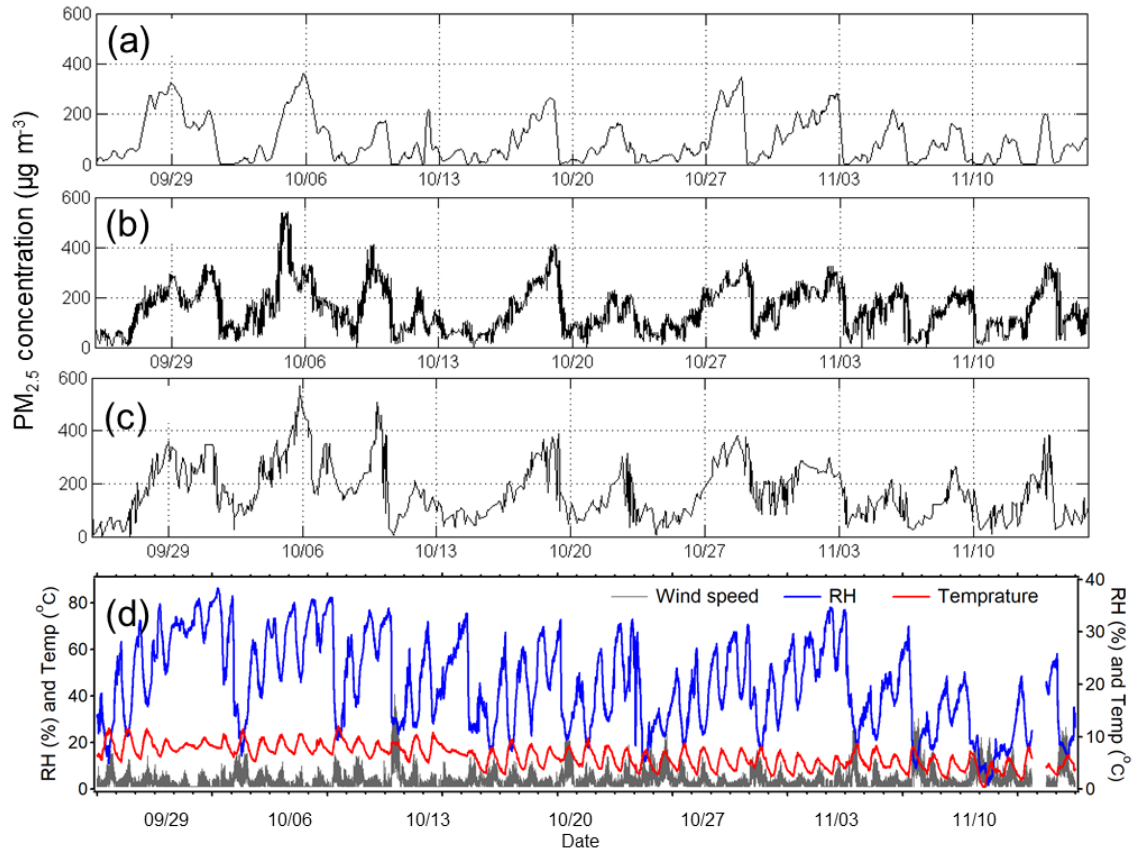
Figure 4.3 Time series of measured PM₂.₅ mass concentrations and meteorological fields from 25 September to 14 November 2013. (a), PM₂.₅ mass concentration measured at Beijing via the field campaign conducted in 2013 (Guo et al. 2014). (b) and (c) show PM₂.₅ mass concentrations for Baoding and Shijiazhuang, other two megacities over NCP. The PM₂.₅ data for (b) and (c are reprinted from ref (Li et al. 2015). (d), meteorological fields at Beijing, including 10m wind speed, RH and temperature, measured during the field campaign conducted in 2013 (Guo et al. 2014).

Two typical extremely hazy days, i.e. 28 September during the first severe haze episode (25 September – 30 September, EP1) and 5 October during the second severe haze episode (2 October – 6 October, EP2), 2013 are captured both by *in-situ* measurements (Fig. 4.3) and satellite observation (Fig. 4.4). The Moderate Resolution Imaging Spectroradiometer (MODIS)-retrieved aerosol optical depth (AOD) at Beijing is extremely high for EP1 and EP2, exceeding 4.0 and 2.0, respectively. The high AOD area centering at

megacities like Beijing are discernible over NCP during the two days (Figs. 1a and b) and correspondingly, grey haze layers covered a large portion of the NCP region observed in satellite visible images (Figs. 1c and d). This AOD pattern in spatial distribution is also the case for the averaged situation over all the hazy days in 2013 in Beijing (daily $PM_{2.5}$ in Beijing > 200 μg m^{-3}) (Fig. 4.6). Though Beijing shows as one center of AOD plateaus during severe haze periods, it is located at the edge area of AOD plateau for the fall seasonal and annual means of all days in 2013 (Figs. 1e and f). Considering the heavy emissions from megacities like Beijing over NCP through all year, the distinct AOD spatial pattern during severe haze episodes from the case at the climatological scale (i.e., seasonal and annual situation) indicates that the emitted pollutants can build up locally only when severe haze forms, i.e., NPC is under control of adverse weather condition for pollution dispersion (Liu et al. 2013; Guo et al. 2014).
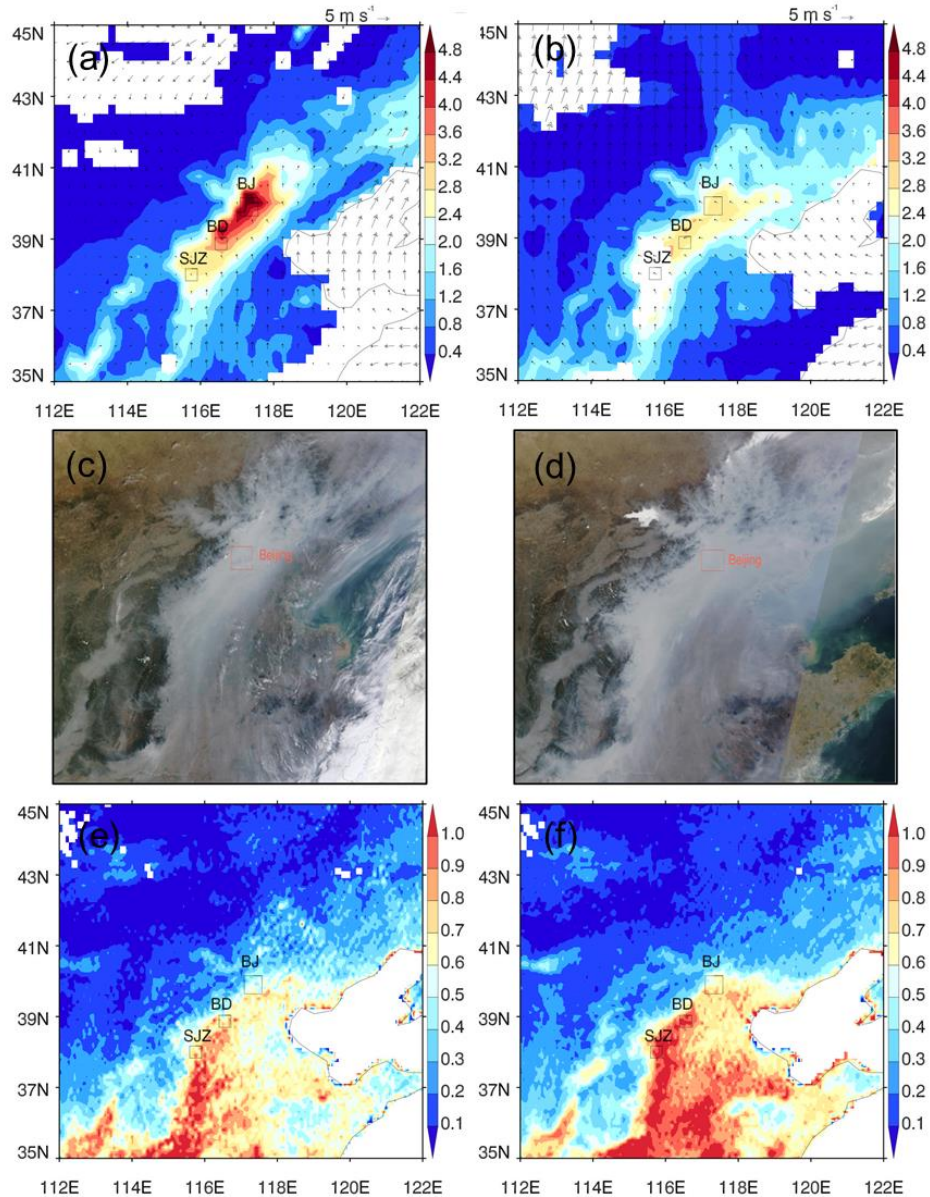
Figure 4.4 MODIS visible images and retrieved AOD for two severe haze episodes in 2013 and the fall seasonal and annual means of 2013 over North China Plain. (a) AOD on 28 September 2013 derived based on the combined Aqua and Terra MODIS measurements. The one large square represents Beijing (BJ) location and the two small squares indicate other major megacities near Beijing over NCP, including Baoding (BD) and Shijiazhuang (SJZ). (b) is same as (a) but for 5 October 2013. Wind field imposed on (a) and (b) is based on ECMWF reanalysis data. (c) Terra visible image for the severe haze day on 28 September 2013. (d) same as (c) but for 5 October 2013. (e) AOD seasonal mean of 2013 fall. (f) AOD annual mean of 2013.

4.3 Photochemistry in Severe Haze Formation

There are several lines of evidence suggesting that the heavy PM pollution leading to severe haze over NCP initialized at urban regions like Beijing due to the efficient PM formation over there. Most evidently, the $PM_{2.5}$ mass concentration during the clean-to-hazy transition period, i.e., 27 September for EP1 and 4 October 2013 for EP2, increased by more than 200 μg m^{-3} in less than 8 hrs (Figs. 4.5a and b). Also, the great elevation of PM was associated with a great increase in the mass concentration of oxygenated organic aerosol (OOA), which is a surrogate for secondary organic aerosol (SOA) (Wood et al. 2010). Since OOA and O_x ($[O_x] \equiv [O_3] + [NO_2]$) are both produced from atmospheric VOC oxidation and both of them have lifetime longer than 12 hours, it is expected that the levels of OOA and O_x should be correlated to some extent when their formations are in the similar timescale and at the same location (Atkinson 2000). For the two haze episodes under study, it is found that the enhancement in OOA coincided with the elevated level of O_x (Figs. 4.5c and d). In addition, the R^2 for the linear regression of OOA and O_x during the rapid transition periods (from 7:00 am to 2:30 pm) were 0.96 for EP1 and 0.95 for EP2, respectively (Fig. 4.5e). The high correlations between OOA and O_x suggest that the production of PM via photochemical reactions was highly active during severe haze episodes. More importantly, the ratio of [OOA] versus [O_x] in Beijing was about 2.4 and 5.1 times of that in Mexico City and Houston, respectively, indicating that the PM formation in Beijing was much more efficient than the case of Mexico City and Houston (Fig. 4.5f). The more intensive photochemical formation of PM is attributable to the presence of higher levels of aerosol precursors like aromatic volatile organic compounds and nitrogen oxides in Beijing than the other two cities (Zhang et al. 2015a; Zhang et al. 2015b).

58
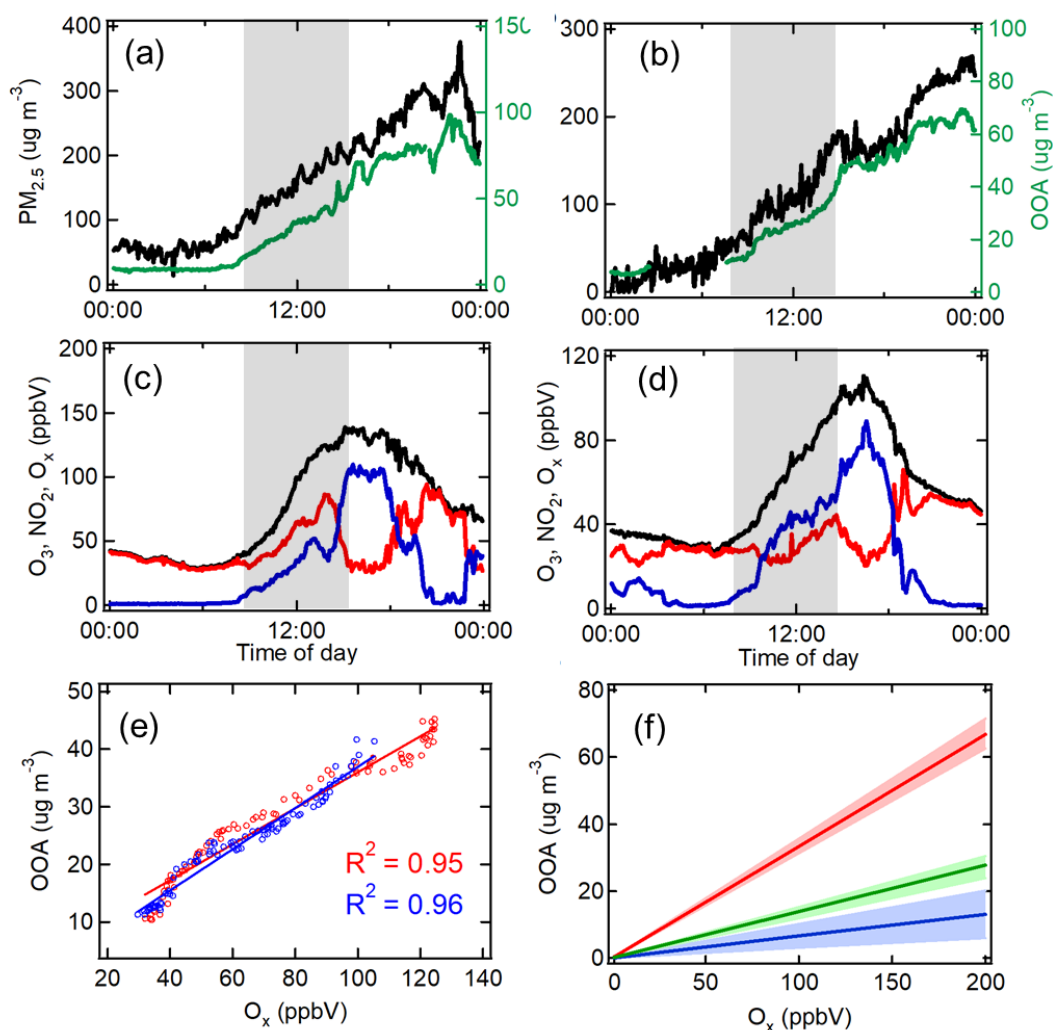
Figure 4.5 Time series of in-situ measured PM, PM composition and associated gaseous species as well as the correlations between O_x and OOA during transition periods of the two severe haze episodes in Beijing. (a), time series of OOA (green) and PM$_{2.5}$ (black) mass concentration on 27 September 2013. (b), same as (a) but for 4 October 2013. 27 September and 4 October 2013 are the transition periods from clean days to the most polluted days for the two severe haze episodes. (c), time series of O_3 (blue), NO_2 (red), and O_x (black) mixing ratios on 27 September 2013. (d), same as (c) but for 4 October 2013. (e), linear regressions of O_x and OOA on 27 September (red circles) and 4 October (blue circles), 2013. Grey shadings in (A-D) denote the time periods used for the linear regressions in (e). (f), the ratios of [OOA] and [O_x] changes (Δ[OOA]/Δ[O_x]) in Beijing and other two megacities (i.e. Mexico City and Houston) in the world.

Once produced, PM rapidly accumulated at urban scale and a regional severe haze eventually formed over NCP since the region was under the control of stagnant weather condition, characterized by the weak southerly winds over Beijing and its surrounding areas (Figs. 4.4a and b).

4.4 Aerosol-PBL Interactions during Severe Haze

Based on the ground-based measurements and the reanalysis data of the Modern-Era Retrospective analysis for Research and Applications, Version 2 (MERRA2), it is revealed in Fig. 4.6a that daily maximal PBL height is negatively correlated with surface $PM_{2.5}$ concentration. Fig. 4.6b shows that the maximum PBL height on severe haze days (daily $PM_{2.5}$ concentration > 200 μg m^{-3}) is lower by 800 m on average than that on typical clean days (daily $PM_{2.5}$ concentration < 30 μg m^{-3}). Also note that the dimming area of satellite-retrieved surface solar radiation (SSR), an average over all the severe haze days in 2013, exactly matches the high AOD region over NCP (Figs. 4.6c and d). The response of PBL development to PM pollution and the linkage of aerosol-PBL interactions to aerosol radiative effects are elucidated by sensitivity studies modeling the two most hazy days during the two selected severe haze episodes (hereafter HAZE cases). The cases under typical clean condition (hereafter CLEAN cases) are performed as well to isolate severe haze effects by comparing HAZE cases with CLEAN cases.
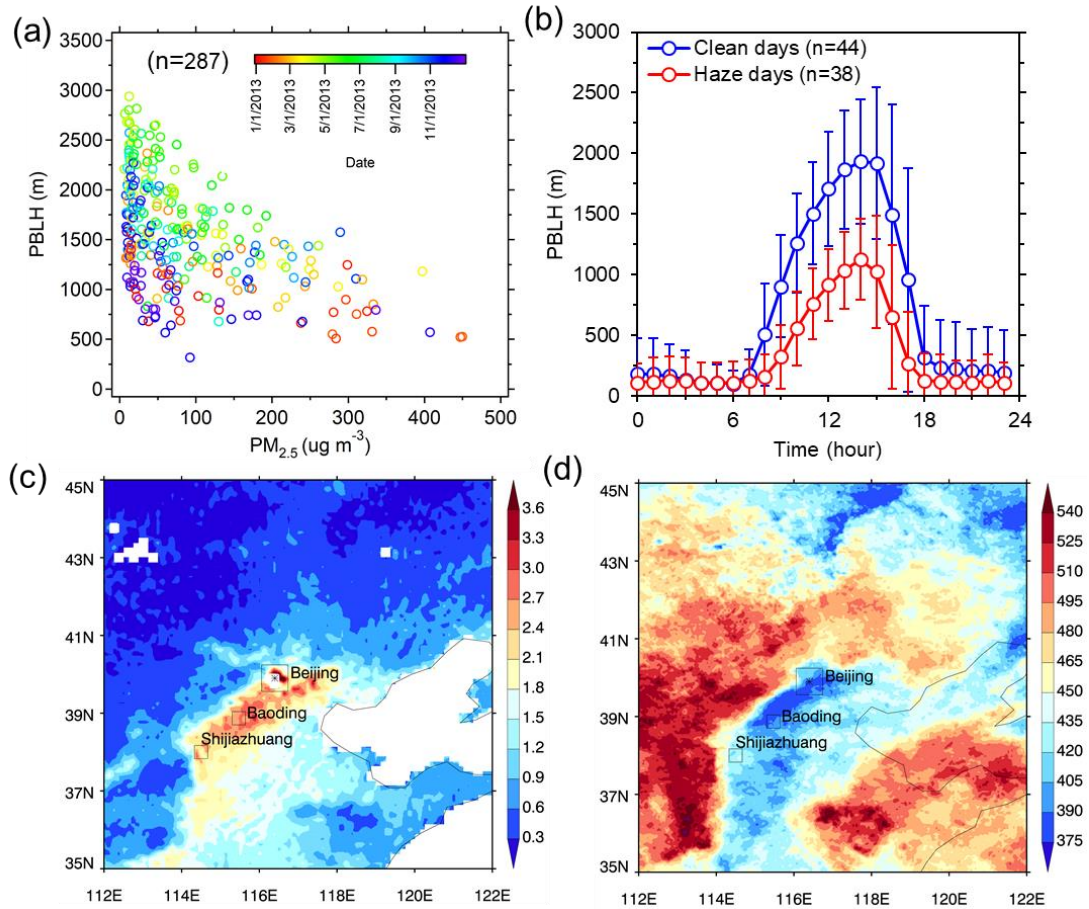
Figure 4.6 The correlations among aerosol pollution, PBL height, and surface solar radiation (SSR). The scattering plot for daily PM$_{2.5}$ concentration and PBL height (a). The mean diurnal variations of PBL height averaged on all clean days (daily mean PM$_{2.5}$ < 30 μg m^{-3}) and hazy days (daily mean PM$_{2.5}$ > 200 μg m^{-3}) in 2013 for Beijing, China (b). (c) and (d) are satellite-retrieved AOD and surface solar radiation (SSR) averaged over all the haze days in 2013 for Beijing, China, respectively. *n* is the number of days selected for considerations.

It is shown that the simulated maximum height of PBL under the extremely hazy condition is reduced by more than 300 m relative to the clean condition (Fig. 4.7a and c). The reduction in PBL height is reasoned to aerosol radiative effects (Yu et al. 2002; Petäjä et al. 2016). The warmer temperature is found at the altitude of around 1 km and less SSR is over ground under severely hazy condition than the clean condition (Fig. 4.7b and d). As a

61

result, the updrafts are weakened and the turbulent kinetic energy (TKE) is reduced in HAZE cases relative to CLEAN cases (Figs. 4.7a and c), leading to enhanced atmospheric stratification and hindered the development of PBL. The largely reduced TKE during severe haze periods shown in this study is consistent with a recent field measurement of turbulent fluxes, which are greatly reduced in a mixed surface layer under the polluted condition (Wilcox et al. 2016). Also, the weak wind under severe haze might suppress the entrainment from above the top of the boundary layer, further restricting the development of PBL.

The strong interactions between aerosols and PBL might affect the hazy condition near the surface by altering atmospheric dynamic and thermodynamic conditions and stability in the boundary layer. Firstly, the PM concentration near the ground increases as the mixing layer is compressed, which results in a smaller volume for PM vertical dilution than expected. Secondly, the diurnal feature of PM pollution tends to diminish because of the collapsed PBL, and hence the PM continuously accumulates near the surface. Therefore, the heavy pollution can persist over an extensive period (4-7 days), as observed during the field campaign in Beijing (Guo et al. 2014). The continuous build-up of PM in Beijing for several days is distinct from other megacities across the world with clear diurnal feature of pollution, such as Houston, Los Angeles, and Mexico City (Zhang et al. 2015b), implying that the importance of strong haze-PBL interactions in deteriorating the air quality in Beijing. Thirdly, surface winds are reduced by 0.7 m s^{-1} from CLEAN to HAZE cases because of a stabilized boundary layer under the hazy condition (Fig. 4.8). This suppressed horizontal advection together with weakened vertical convection under severe haze condition suggests that the PM pollution can retain in the atmosphere over the local region for a longer time than expected.
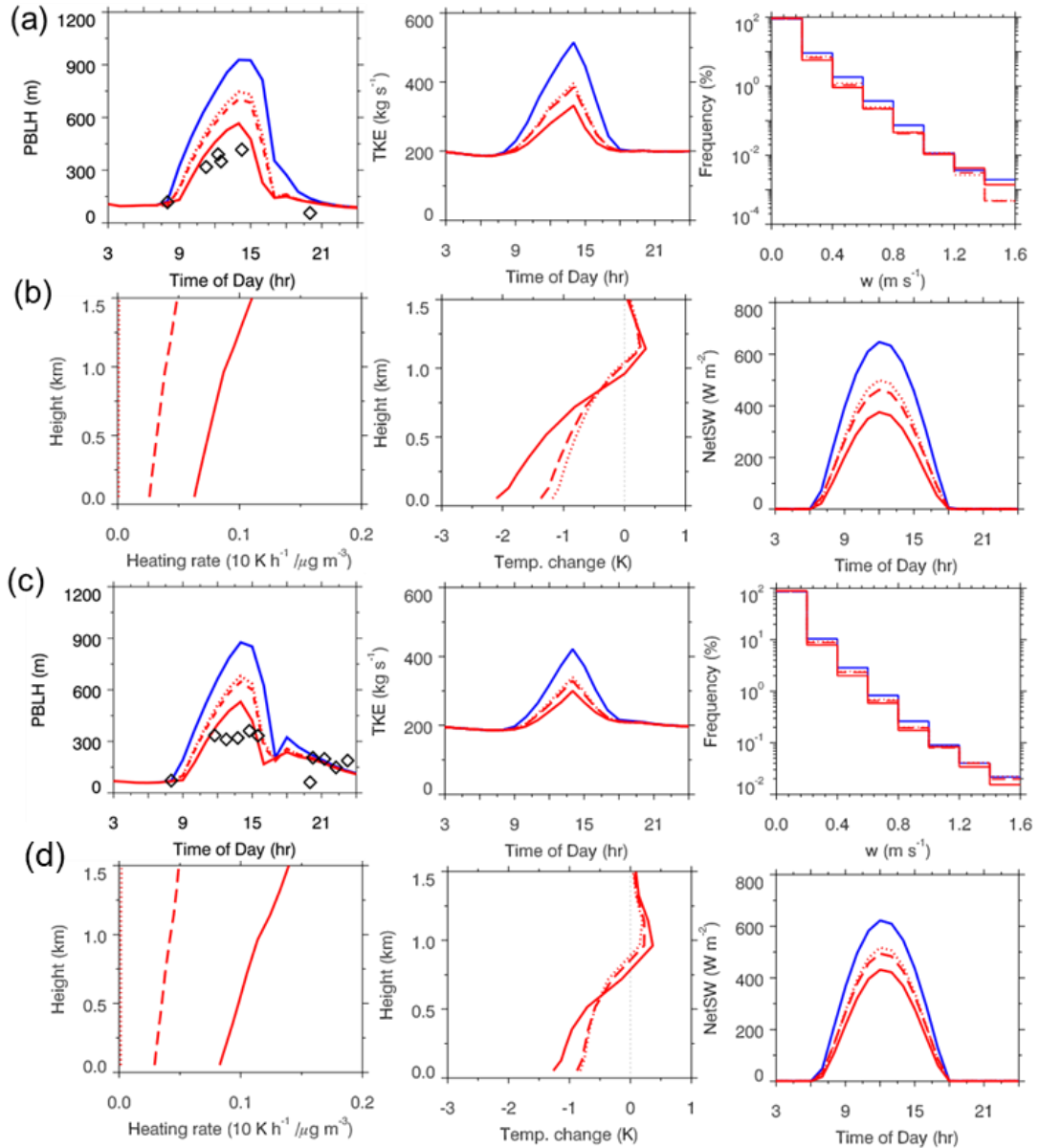
Figure 4.7 Distinct atmospheric dynamic, thermodynamic and radiative features under different pollution conditions. The panels in (a) are temporal evolutions of PBL height (left), vertically-integrated TKE (middle), and frequency of updrafts (right). Blue solid, red dot, dash, and solid lines represent CLEAN, non-BC, fresh" BC, and HAZE cases, respectively. The left panel in (b) is vertical profiles for the shortwave heating rate per unit aerosol mass induced by non-BC components (red dot), "fresh" BC (red dash), and "aged" BC (red solid). The middle panel in (b) is the temperature changes by aerosols without BC (red dot), "fresh" BC (red dash) and aged BC (red solid). The right panel in (b) is the evolutions of net surface shortwave radiation (NetSW). (a) and (b) are for EP 1. (c) and (d) are same as (a) and (b) but for EP 2. The black hollow squares in (a) and (c) are observations of ceilometer measurements.

Finally, the great suppression of PBL height might induce significant enhancement of atmospheric moisture. It shows in observations that the observed RH greatly increases during the two selected episodes (Fig. 4.3d), i.e., about 18% and 19% on clean days (25 Sep. and 2 Oct.) and 55% and 53% on hazy days (28 Sep. and 5 Oct.). In order to examine how sensitive the atmospheric moisture is to the PBL height, we employed a modified Nozaki's equation (Nozaki 1973; Tie et al. 2017) to calculate the RH under different PBL height scenarios using the observed meteorological conditions. Our calculations show that the RH decreases from 68% to 19% for EP1 and from 72% to 23% for EP2 if the PBL height increased only by 200 m on the two most hazy days, suggesting that the moisture in the boundary layer is highly sensitive to the PBL height. The more humid boundary layer is perhaps due to the shallower boundary layer allowing moisture to accumulate, the cooler surface temperature leading to lower saturation level, and the less entrainment of dry air from above the more stable boundary layer under extremely hazy condition (Fan et al. 2008; Liu et al. 2013; Tie et al. 2017). The increasing moisture in the mixing layer under hazy condition leads to an additional hygroscopic growth of aerosol particles (Fan et al. 2008; Liu et al. 2013). For example, the observed growth factors associated with the RH enhancement during EP1 and EP2 both increases from 1.3 on clean days to 1.5 on hazy days, based on calculations using an empirical equation derived for Beijing (Meier et al. 2009). This additional growth of aerosol particles can cause an additional reduction of incoming solar radiation by aerosol scattering and absorption and hence amplify the haze suppression effect on PBL development. In addition to inducing the additional hygroscopic growth, the high moisture favors aqueous-phase reactions in the atmosphere, leading to sufficient formation

of sulfate and thus an elevated level of PM pollution during the haze days, as suggested by

Wang et al. (2016a).
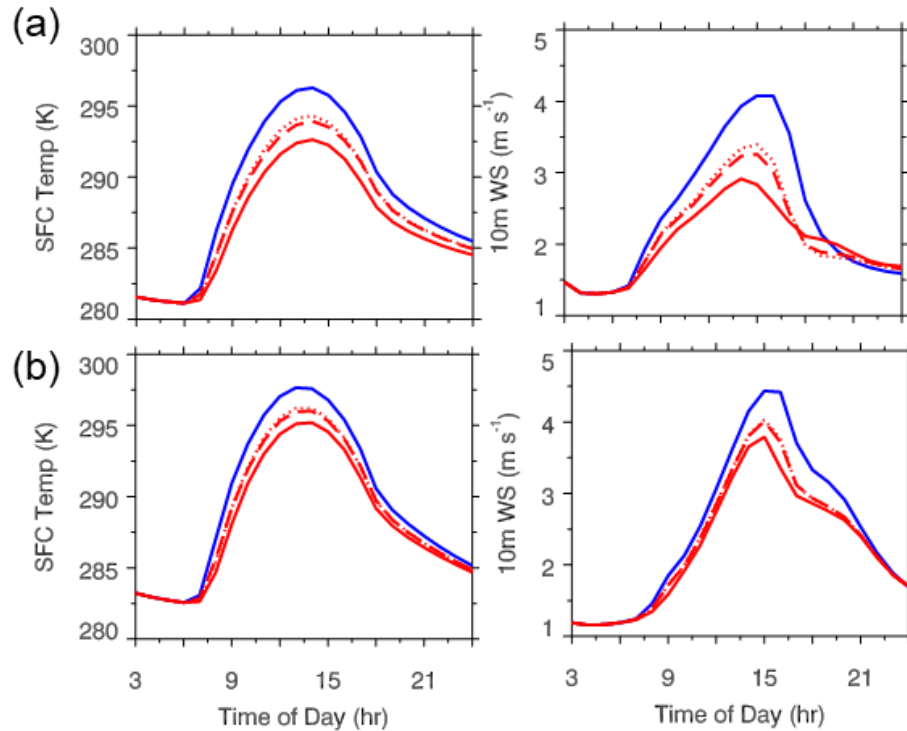
Figure 4.8 Temporal evolutions of simulated surface temperatures (left) and 10-meter wind speeds (right) under different aerosol pollution conditions. (a) is for haze EP1 and (b) for haze EP2. Blue solid lines represent CLEAN case, red dot lines represent the non-BC case, red dash lines represent "fresh" BC case, and red solid lines represent HAZE case (or "aged" BC).

Therefore, the more polluted condition near ground because of the thermodynamic

and dynamic feedbacks induced by the strong aerosol-PBL interactions could further

strengthen the aerosol suppression on PBL development and thus additional stabilization and

moisture enhancement in the boundary layer, leading to a positive feedback loop which further amplifies the hazy condition.

4.5 The Importance of BC and its Aging in Aerosol-PBL Interactions During Severe Haze

In order to isolate BC's role in the suppression of PBL during hazy days, additional simulations are performed for non-BC cases (i.e. BC absorption is turned off in the simulation) and "fresh" BC cases (i.e. the BC core is externally mixed with ammonium sulfate shell). In addition, HAZE cases can be treated as a case with "aged" BC, given the considerations of full aerosol components (i.e. consisting of both BC and non-BC) and core-shell configuration (BC as core and the non-BC component as shell).

Comparing to non-BC cases, "fresh" BC cases show negligible effect on the haze-PBL interactions (Figs. 4.7-4.9), and the changes in solar radiation, thermodynamic and dynamic condition in the mixing layer from non-BC cases to "aged" BC cases are primarily attributed to the radiative effects of the aged BC. It is shown in Figs. 4.7b and d that the shortwave heating rate per unit mass of aged BC is much larger than that of non-BC component and is two times of "fresh" BC, suggesting that BC is more efficient absorbing constituent than non-BC component and the aging process greatly strengthens BC ability to attenuate solar radiation. Though BC accounts for only 6% of total aerosol mass in HAZE cases, there is about 80% of atmospheric warming by total aerosols contributed by BC aging (Figs. 4.7b and d), and about one third of the total reduction in SSR by full-component aerosols can be attributed to the enhancement of BC absorption after aging. The additional reduction of SSR caused by BC aging leads to an additional 0.5-0.8 K cooling at the surface. As a consequence, the atmosphere is stabilized more in "aged" BC cases relative to non-BC

or "fresh" BC cases, evident in the weaker updrafts, smaller TKE, and shallower boundary layer (Figs. 4.7a and c). The maximum PBL height decreases by about additional 150 m with aged BC relative to the non-BC or "fresh" BC cases, and the BC aging contributes more than 30% of the total reduction of PBL height caused by severe haze.

Given that the strong aerosol radiative effect during severe haze days can be largely attributed to the aged BC, cutting off BC emissions at megacities such as Beijing might efficiently alleviate the severity of haze by weakening suppression effect induced by PM on PBL development. The restriction of boundary layer development by BC absorption found here is consistent with the so-called BC "dome effect" (Ding et al. 2016; Petäjä et al. 2016), but in this study we also illustrate the possible importance of the BC aging on haze-PBL interactions.
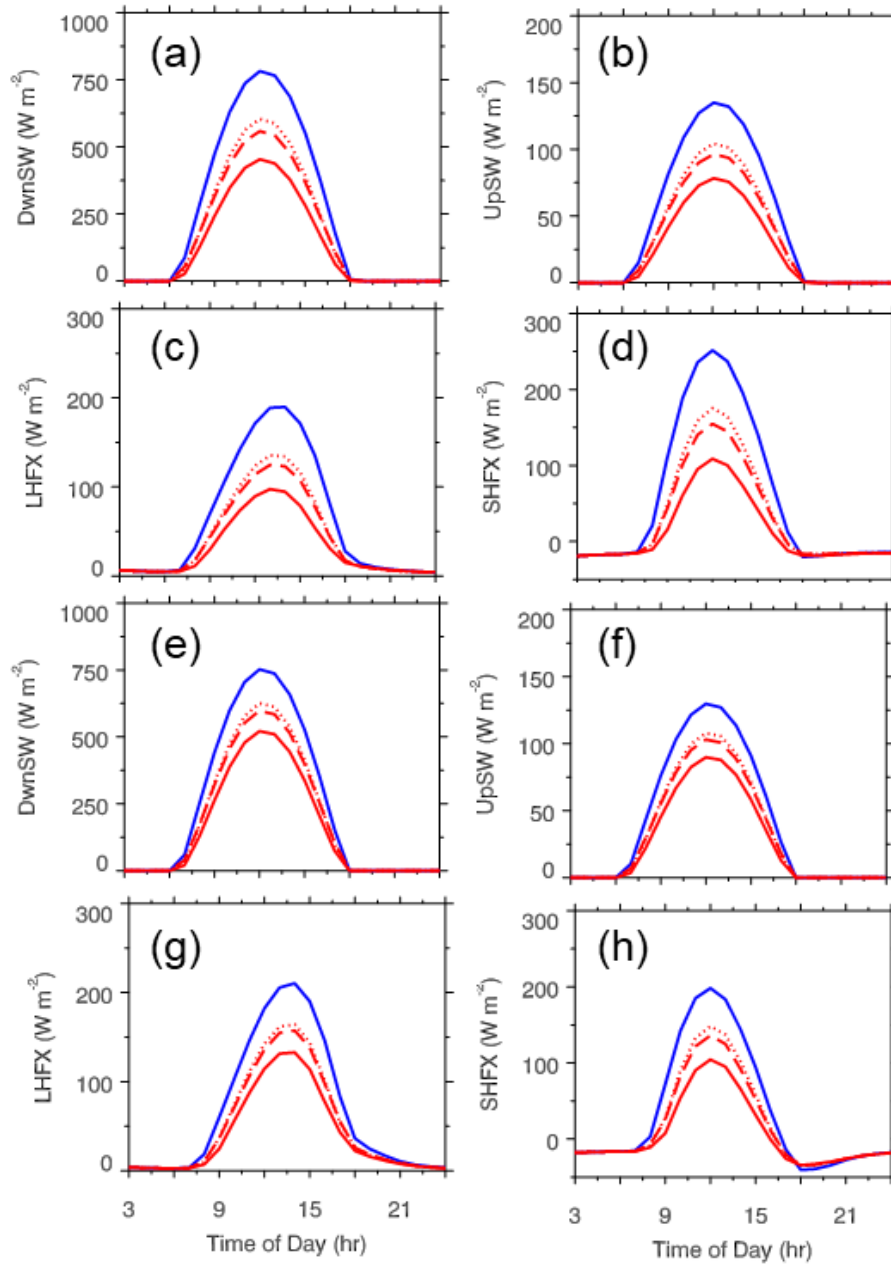
Figure 4.9 Temporal evolutions of downward (a and e) and upward (b and f) shortwave radiation, and latent (c and g) and sensible (d and h) heat fluxes under different aerosol pollution conditions. Panels (a-d) are for EP1 and (e-h) for EP2. Blue solid lines represent CLEAN case, red dot lines represent non-BC case, red dash lines represent "fresh" BC case, and red solid lines represent HAZE case (or "aged" BC).

4.6 Aerosol Direct Radiative Forcing Under Severe Haze Condition

It has been shown that the aerosol direct radiative effects during haze events cause significant regional climate effects (Wang et al. 2009; Ding et al. 2016). Fig. 4.10 shows that the total aerosol forcing at the surface and in the atmosphere under typical severe haze EP1 (EP2) in Beijing are -87.8 (-56.9) W m^{-2} and 82.2 (62.8) W m^{-2}, respectively. The positive atmospheric forcing of the total aerosol is dominated by the forcing of aged BC, which accounts for 80% of the total atmospheric forcing for both haze episodes. The net TOA forcing by total aerosol for EP1 (EP2) is around -5.6 (-5.9) W m^{-2}, which is much smaller than that of the non-BC component with a large negative value of -36.8 (-26.0) W m^{-2}. Clearly, the strong cooling at the surface induced by full-component aerosol under severe haze is canceled out to a large extent by the strong warming in the atmosphere mostly induced by aged BC, leading to a relatively small TOA forcing. Climatologically, it has been shown that the aerosol TOA forcing at regional/national level is nearly zero or even shows a small positive value in China (Li et al. 2007; Ramanathan et al. 2007; Ding et al. 2016), also demonstrating that the large positive forcing by absorbing aerosols greatly compensates the negative forcing by non-absorbing aerosols (Table 4.2). Therefore, the global warming can be mitigated by reducing BC emissions at megacities like Beijing because of the strong warming effect of BC during severe haze events, as suggested in Wang et al. (Wang et al. 2015b).
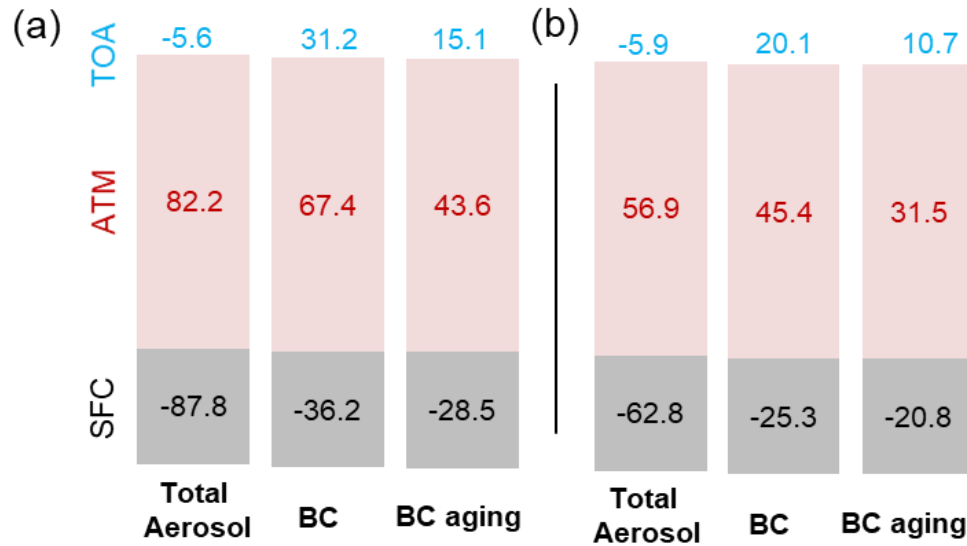
Figure 4.10 Aerosol direct radiative forcing of total aerosol, BC, and BC aging at TOA, atmosphere (ATM), and surface (SFC) for typical severe haze days in Beijing. (a) is for EP1 and (b) for EP2. All forcings are 24-hour means based on the simulations of the two severe haze episodes in Beijing (EP1, 28 September; EP2, 5 October 2013). The forcing due to BC aging is the difference between simulation cases with and without BC aging.

It is worth mentioning that the TOA forcing caused by BC aging contributes about half of the positive forcing by total BC for both haze cases, again suggesting that the aging process considerably enhances the BC warming effect and has significance on regional climate effects. To better understand the BC aging process and improve its representation in modeling is crucial to more accurately estimate BC forcing and therefore aerosol forcing, which requests more decent field measurements and laboratory studies in future (Gustafsson and Ramanathan 2016; Peng et al. 2016).

Table 4.2 Comparisons for aerosol forcing and BC forcing.

Aerosol forcing at TOA (W/m²)						
Sources	R2007	R2007	L2009	W2009	D2016	This study
Method	Model	Model	Obs.	Model +Obs	Model	Model
Region	China	BJ	XH	BJ	China	BJ
AOD	~0.14	0.65	>0.2	1.78	-	3.1
Forcing	0	-20.7	2.4	-21	2.4	-5.6/-5.8
BC forcing at TOA (W/m²)						
Sources	B2013	P2016	G2016	D2016		This study
Method	Model	Model	Model +Obs	Model		Model
Region	China	BJ	XH	BJ		BJ
Forcing	0.71	0.77	~1	35.8		25.7

BJ = Beijing, XH = Xianghe
R2007: Ramanathan et al. (Ramanathan et al. 2007).
L2009: Li et al. (Li et al. 2007).
W2009: Wang et al. (Wang et al. 2009).
D2016: Ding et al. (Ding et al. 2016).
B2013: Bond et al. (Bond et al. 2013).
P2016: Peng et al. (Peng et al. 2016).
G2016: Gustafsson et al. (Gustafsson and Ramanathan 2016).

4.7 Summary

We have illustrated the temporal and spatial characteristics of PM pollution during typical severe haze events over NCP by examining ground-based field measurements and satellite observations. It is clearly shown in the ground-based measurements that the temporal evolutions of PM concentration were consistent among the three megacities (Beijing, Baoding, and Shijiazhuang) across NCP, all showing a simultaneous and rapid increase when haze forms and the nearly same timing of peaks on the haziest days. Distinct from seasonal and annual means, in which Beijing was located at the edge of the high AOD region, an AOD plateau with Beijing as one center was observed based on satellite retrievals

on severe haze days. We have also documented that the rapid formation of PM while Beijing haze forming was due to the intensive photochemical reactions, indicated by the concurrent enhancement in OOA and PM concentrations and the strong linear correlation between OOA and O_x concentrations during the clean-to-hazy transition period. The [OOA]/[Ox] ratio in Beijing is much higher than that in Mexico City and Houston which also suffer PM pollution, attributed to the much higher level of gaseous precursors in Beijing than the other two cities (Guo et al. 2014). As a result, it is crucial for regulating the emissions of gaseous precursors leading to the aerosol formation at megacities in China like Beijing to reduce the haze occurrence and alleviate haze severity.

We have elucidated by modeling the underlying mechanisms for severe haze-PBL interactions, as well as the further feedbacks on hazy condition at ground. Our modeling studies have shown that the PBL height can be largely reduced while severe haze forming, since the boundary layer is markedly stratified (as indicated by the reduced TKE and weakened updrafts) because of the strong aerosol heating in the atmosphere and the strong cooling at the surface, with presence of severe haze. Near surface PM concentration increases in a compressed mixing boundary layer. Also, the dispersion of PM is not favored in the stratified and collapsed boundary layer, and the accumulation of PM continues and can span for several days. In addition, our calculations using the modified Nozaki's equation shows that the depressed PBL results in a great enhancement of atmospheric moisture near ground, and the higher humidity in boundary layer can lead to the larger hygroscopic growth of particles and more efficient aqueous-phase PM production. Therefore, the hazy condition near surface can be significantly exacerbated because of the strong interactions between

72

aerosols and PBL and the subsequent positive feedbacks of dynamics and thermodynamics on aerosol-PBL interactions.

It has also been revealed by modeling studies that the heavy aerosol pollution under severe hazy condition causes significant regional climate effects. The TOA forcing of aerosols for the two typical hazy days in Beijing under study is about of -5.6 ~ -5.9 W m^{-2}, clearly a result of the large cooling at the surface mostly balanced by the large solar heating in atmosphere mainly caused by absorbing aerosols like BC component.

It has been revealed that BC is the major contributor to the positive aerosol forcing in the atmosphere, accounting for 80% of total aerosol heating, and thus plays a significant role in haze-PBL interactions. Cutting off BC emissions does not only improve local air quality by alleviating the suppression effect of severe haze on PBL development but also mitigate global warming due to the large reduction in the strong positive forcing. In addition, we have documented that the aging of BC can contribute more than 40% of PBL collapse induced by total aerosols and about 50% of TOA positive forcing caused by total BC during severe haze, suggesting the importance of BC aging in aerosol-PBL interactions and aerosol regional climate effect under extremely hazy condition. Our work indicates that there is a need to better understand BC aging process and then improve its representation in current models, in order to accurately assess BC/aerosol regional climate effect. Therefore, more field measurements, laboratory work as well as modeling studies are required in future for elucidating the BC aging and its impacts on aerosol optical properties and further on climate (Gustafsson and Ramanathan 2016; Peng et al. 2016).

5. SENSITIVITY OF AEROSOL IMPACTS ON HURRICANE WITH OCEAN COUPLING

In this study, Hurricane Katrina 2005 is simulated using a three-dimensional coupled atmosphere-ocean model to investigate the aerosol-hurricane-ocean three-way interactions. The WRF model is used to simulate the hurricane track and intensity. The WRF coupled with a 3-dimensional ocean model (Patricola et al. 2012) is employed to incorporate the thermodynamic and dynamic feedbacks of air-sea interactions to aerosol-hurricane interactions. The aerosol microphysical effects on hurricane intensity and structure are evaluated explicitly using an aerosol-aware two moment bulk microphysical scheme and an aerosol radiative module in the presence of air-sea interactions. Moreover, comparisons are performed for a coupled simulation of the polluted hurricane and an uncoupled one with SST from the outputs of the corresponding clean coupled case. It is the first time that the aerosol-induced ocean coupling effect is isolated for a polluted hurricane and the relative importance of ocean coupling in comparison with aerosol effects is evaluated.

5.1 Model Configuration and Experiment Design

The regional atmosphere-ocean coupled WRF-ROMS model is used to investigate the aerosol-hurricane-ocean three-way interactions in this study. The TAMU scheme is employed to study aerosol effects on hurricane with ocean coupling. The atmospheric initial and boundary conditions are constrained by the 6-hourly NCEP Climate Forecast System Reanalysis (CFSR, Saha et al. (2010)). The horizontal grid spacing for WRF runs is 3 km, meeting the minimum requirement to represent dynamical and microphysical responses to aerosols (Rosenfeld et al. 2012). Therefore, the convective parametrization is turned off

when running WRF. The simulation domain includes the entire Mexico Gulf and the southern portion of the United States (75° W – 100° W; 17° N – 38° N).

The horizontal grid spacing is also 3 km for ROMS simulations, with 50 vertical levels. The domain for ROMS is configured a little smaller than that of WRF. The initial and boundary conditions for ROMS simulation are based on the HYbrid Coordinate Ocean Model (HYCOM, https://hycom.org/) data set. In this study, the HYCOM reanalysis is used to constrain SST over the ocean regions outside of the ROMS domain.

The initial vertical aerosol profiles for all simulations are characterized by the peak number concentration at the surface and an exponentially decreasing concentration along the vertical direction. The initial aerosol spatial distribution is based on MODIS AOD observations, showing a clear feature of land-ocean contrast (Fig. 5.1a). Therefore, the anthropogenic aerosol concentration over land in all simulations is set as two times of that over the ocean for both initial and boundary conditions (Fig. 5.1b). The aerosol number concentration is fixed at the initial level at lateral boundaries, and aerosols are advected from the lateral boundaries into the inner domain when wind conditions are favorable.

The sea salt particles are considered in this study. The sea salt number concentrations for the initial and boundary conditions are set as 100 cm^{-3}, which is consistent with Lynn et al. (2016). The emissions of sea salt are proportional to surface wind speed, showing high emissions of sea salt at the center of storm, relative to the outside of hurricane.

To test the aerosol sensitivity of hurricane development in the presence of air-sea interactions, we performed three sets of experiments at different aerosol loadings. A coupled clean case (hereafter CLEAN case) has an initial aerosol loading of 200 cm^{-3} over land and 100 cm^{-3} over ocean. To examine aerosol effect with ocean coupling, we increase the aerosol

75

initial concentration by ten times, i.e., aerosol loading of 1000 cm^{-3} over land and 500 cm^{-3}

over ocean, for a coupled polluted case (hereafter POLLU case). The importance of the

ocean coupling effect cannot be evaluated by simply contrasting a coupled simulation with

an uncoupled one since the simulated results greatly vary with the dataset selected for SST

constraining in uncoupled simulations. To avoid this, an additional uncoupled simulation is

carried out with the same aerosol loading as POLLU case but with SST prescribed based on

the output of CLEAN case (hereafter P_UC case).
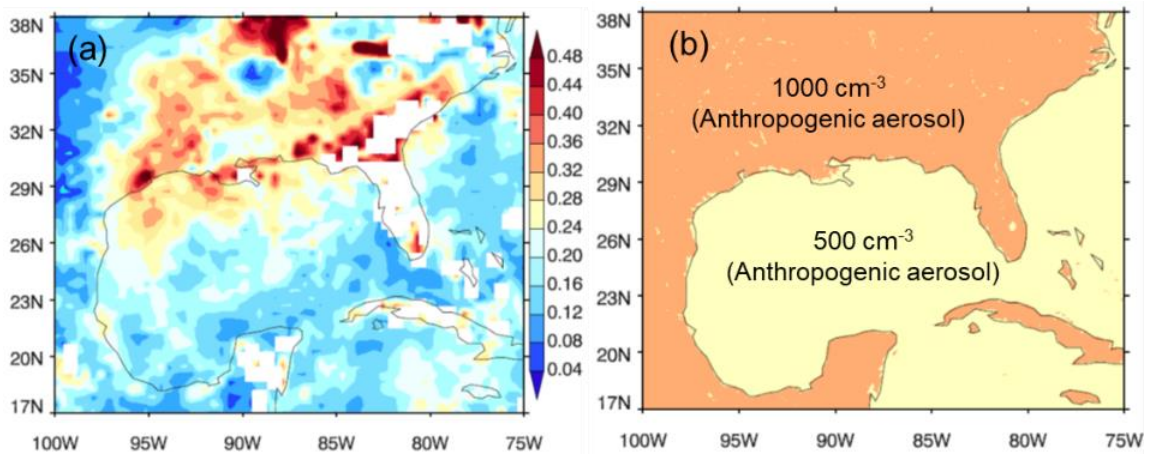
Figure 5.1 MODIS retrieved AOD averaged over the period prior to and during Hurricane Katrina 2005 (Aug. 24 – Aug. 31) (a) and the aerosol initial configuration for simulations of polluted cases (b).

By doing so, the difference between P_UC and CLEAN case is the incorporation of

aerosols, thus the contrast of the two cases representing aerosol effect only. The difference

between POLLU case and P_UC case represents the feedback of air-sea interactions due to

aerosol effect, hereafter referring to the ocean coupling effect. The descriptions of all the

experiments are summarized in Table 5.1.

Table 5.1 List of simulation cases.

Cases	Aerosol configuration	Ocean coupling	SST
CLEAN	Anthropogenic aerosols over land/ocean: 200/100 cm^{-3}. Sea salt: Initial concentration of 100 cm^{-3} and continuous emissions as a function of surface wind speed	Yes	IC/BC based on HYCOM and updating by ROMS
C_CFSR	As in CLEAN case	No	Prescribed by CFSR reanalysis
C_HYCOM	As in CLEAN case	No	Prescribed by HYCOM reanalysis
POLLU	Anthropogenic aerosols over land/ocean: 1000/500 cm^{-3}. Sea salt: Initial concentration of 100 cm^{-3} and continuous emissions as a function of surface wind speed	Yes	As CLEAN case
P_CFSR	As in POLLU case	No	Prescribed by CFSR reanalysis
P_HYCOM	As in POLLU case	No	Prescribed by HYCOM reanalysis
P_UC	As in POLLU case	No	Prescribed from outputs of CLEAN case

The simulations are verified against available observations in terms of SST and hurricane track and intensity. In comparison with the observations from the 9 km-resolution microwave plus infrared (MW_IR) remote sensing (Optimally Interpolated (OI) MW_IR SST daily products), the coupled simulation better captures the SST cold band associated with hurricane passage than two reanalysis datasets, i.e. CFSR and HYCOM (Fig. 5.2). In addition, all the simulations well reproduce the best track of hurricane Katrina (Fig. 5.3) and the observed timing of hurricane intensity evolutions (Fig. 5.4a and b).
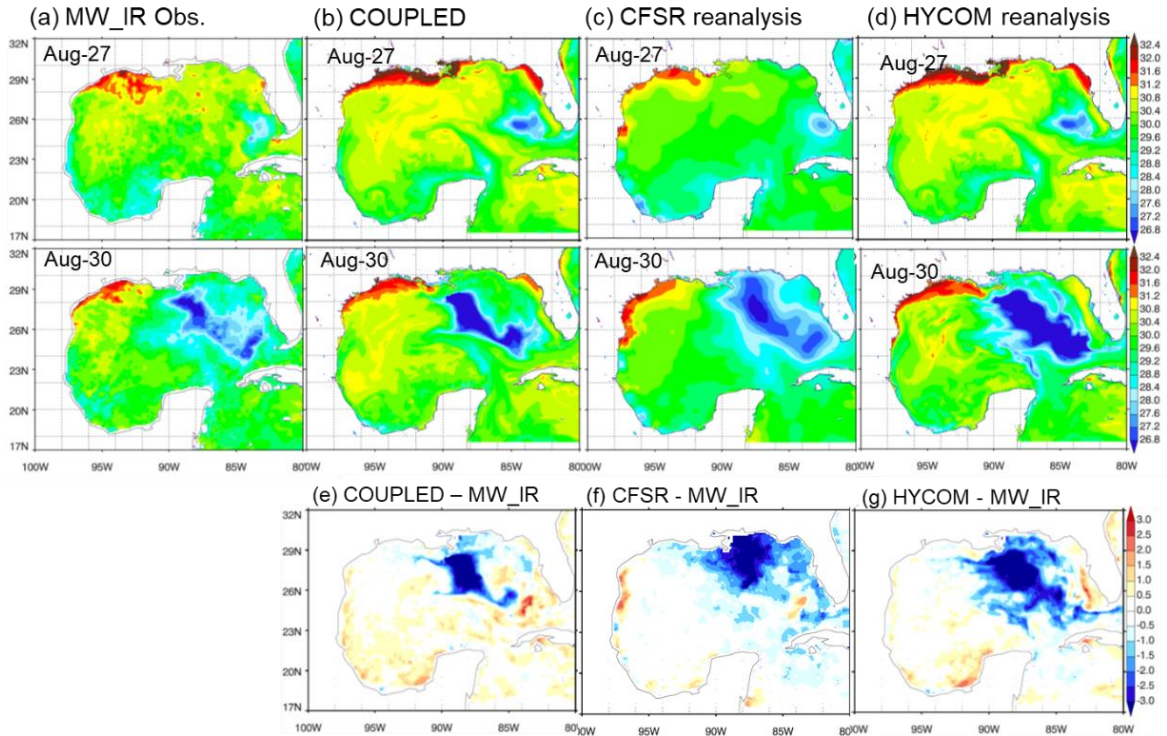
Figure 5.2 Comparison of daily mean SST from observations (MW_IR), the WRF-ROMS coupled simulation and reanalysis SST (CFSR and HYCOM) before (Aug. 27, 2005) and after (Aug. 30, 2005) hurricane Katrina passage. (a) the 9 km-resolution microwave plus infrared (MW_IR) Optimally Interpolated (OI) SST daily products; (b) SST outputs from the coupled simulation (CLEAN case); (c) CFSR SST; (d) HYCOM SST; (e) the difference between coupled simulation and MW_IR observations; (f) the difference between CFSR reanalysis and MW_IR observations; (g) the difference between HYCOM reanalysis and MW_IR observations.
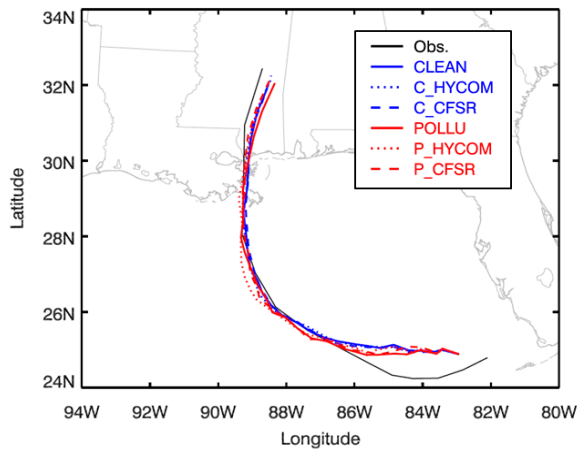
Figure 5.3 Comparison of the simulated track with NHC best track.
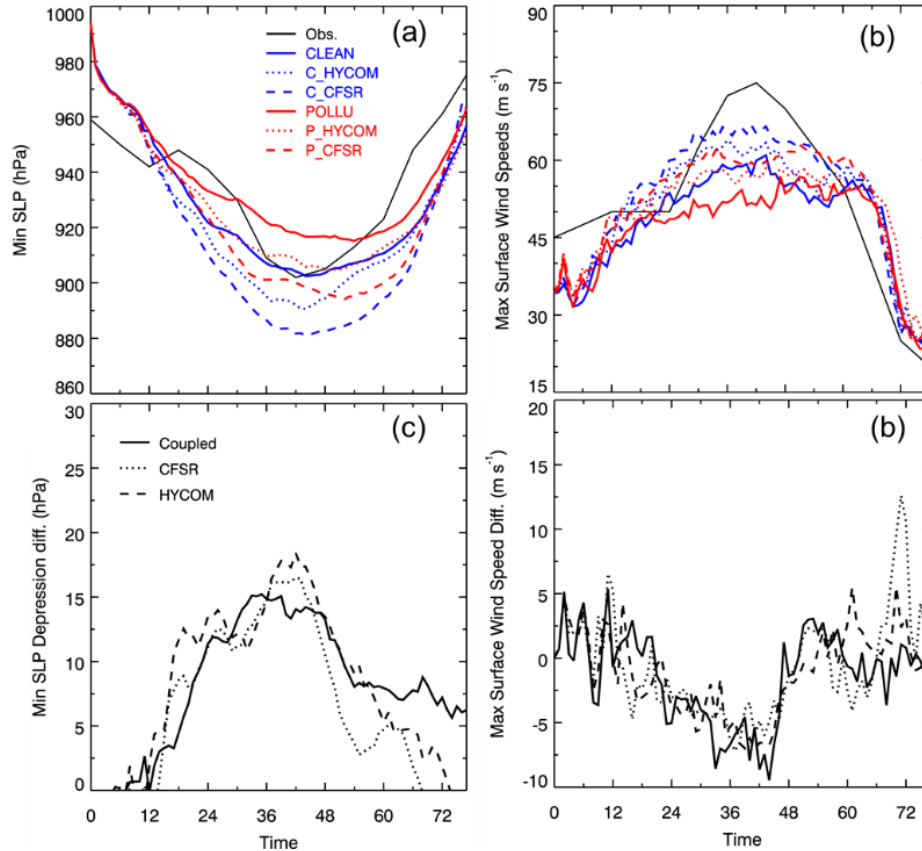
Figure 5.4 Comparison of coupled and uncoupled simulations with SST prescribed based on reanalysis datasets. (a) Minimum SLP; (b) maximum surface wind speed; and (c) and (d) are aerosol-induced changes in pressure depression and maximum wind speed between clean and polluted cases both for coupled and uncoupled simulations. Two reanalysis datasets are used here to drive uncoupled simulations, including CFSR and HYCOM.

Fig. 5.5 shows the evolution of the aerosol surface concentration with time. Clearly the aerosols are depleted quickly in the center of hurricane due to the nucleation removal. The aerosols advected from the lateral boundaries can complement the loss of aerosols. However, the aerosol initial distribution is assumed uniform over land and ocean, and the emissions from the continent are not considered in this study. These assumptions are simplified and thus might lead to biases when estimating the aerosol effect on the hurricane, which requires more realistic configurations for aerosol initial condition in the future studies.
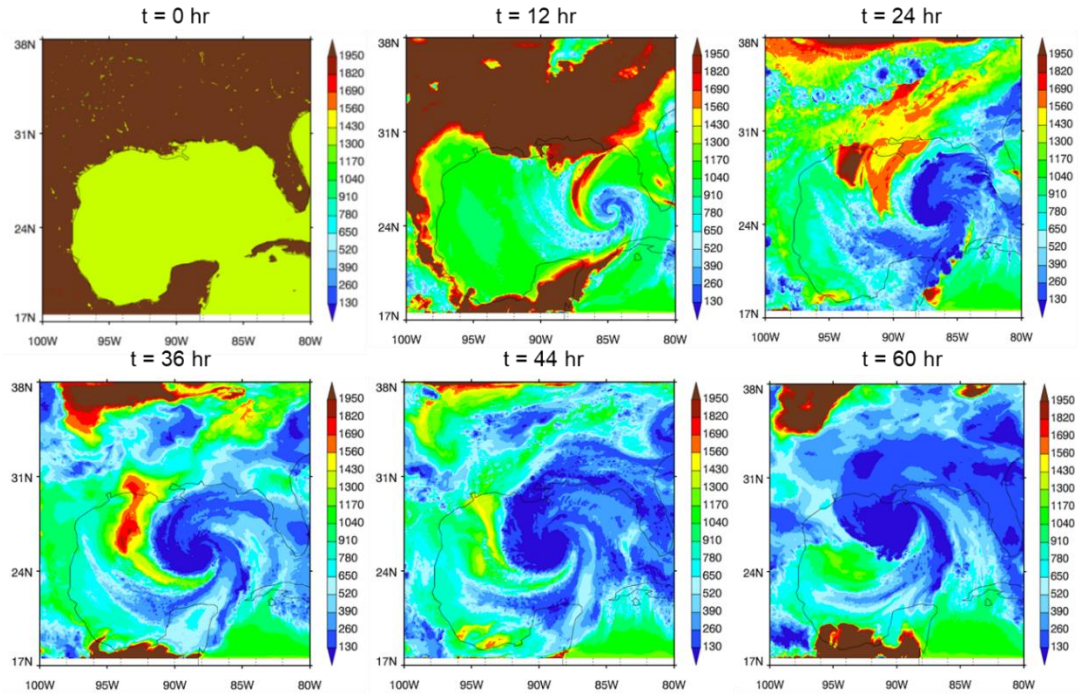
Figure 5.5 Temporal evolution of aerosol number concentration (cm^{-3}) near ground for a polluted case with 2000 cm^{-3}.

In addition, the simulated aerosol distribution is compared to the available MODIS AOD at 18:00 UTC, August 27, 2005 (Fig. 5.6). The overall pattern of aerosol number concentration at the surface is similar as AOD, particularly for the aerosol flow from the continent involved into the storm system. We still need more observations to verify the evolution of aerosols through the entire hurricane lifecycle in the future studies.
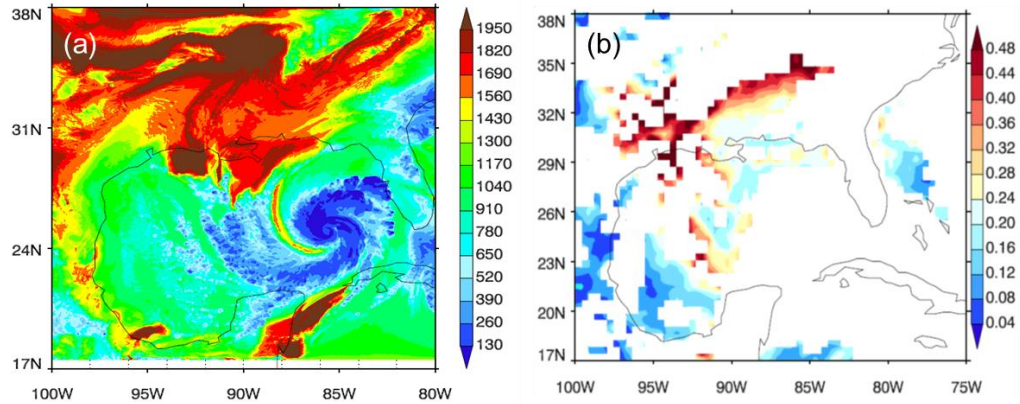
Figure 5.6 Comparison between simulated aerosol concentration with MODIS AOD at 18:00 UTC, August 27, 2005.

5.2 Aerosol Microphysical Effect on Strom with Ocean Coupling

Fig. 5.7 displays the overall responses of hurricane intensity, circulation size and structure to aerosol effects in presence of air-sea interactions (CLEAN versus POLLU cases). Figs. 5.7a and b show that involving aerosols in the hurricane circulation tend to greatly reduce hurricane peak intensity by reducing minimum sea-level pressure (SLP) depression and decreasing maximum surface wind speed. The aerosol weakening effect on hurricane in this coupled study is consistent with previous studies using uncoupled models (Rosenfeld et al. 2007; Khain et al. 2010; Rosenfeld et al. 2011; Wang et al. 2014a). In addition, Figs. 5.7c-e reveal that more precipitation is produced in the POLLU case than the CLEAN case, particularly during the time period from 24 hr to 48 hr. The enhancement in precipitation in the polluted condition might be due to the invigoration of cloud formation at hurricane periphery induced by aerosol effects. More discussions will be provided later.
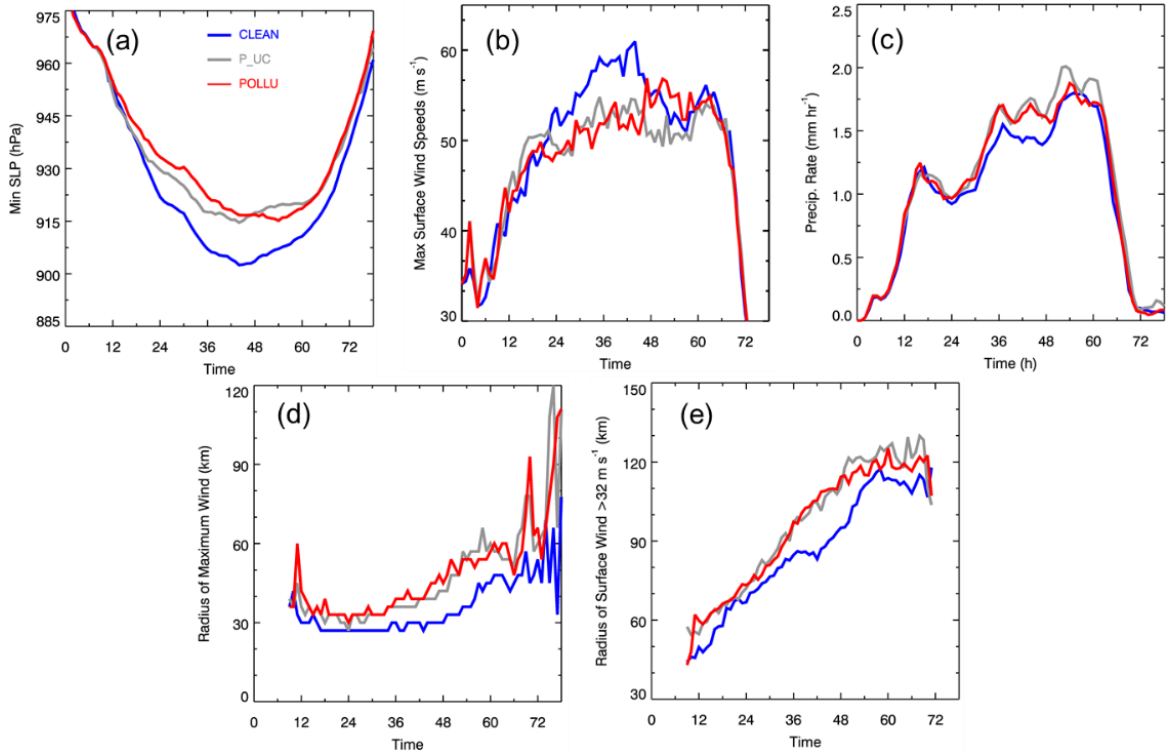
Figure 5.7 Hurricane peak intensity, size, and precipitation in response to the effects of aerosol and ocean coupling. (a) minimal sea-level pressure; (b) maximal surface wind speed; (c) domain-averaged precipitation rates; (d) radius of maximum wind (RMW); and (e) radius of hurricane force wind > 64 kt. CLEAN is a clean case, and POLLU and P_UC are polluted cases. CLEAN and POLLU are performed using WRF-ROMS coupled model, and P_UC is performed using WRF only with SST prescribed based on outputs from CLEAN case.

Also, we find that the size of storm can be enlarged by up to 20 km for radius of maximum wind speed (RMW) and radius of hurricane force wind (> 64 kt) in the POLLU case relative to the CLEAN case. The storm circulation expansion and precipitation enhancement induced by aerosol effects are also observed by other uncoupled or coupled studies (Wang et al. 2014a; Khain et al. 2016).

Fig. 5.8 shows the aerosol and cloud microphysics responses during the rapid intensification period at 33 hr. Corresponding to more aerosol particles involved at the

hurricane periphery (50 km – 200 km) in the POLLU case, there are more cloud droplets produced over there. The freezing of the large amount of droplets lifted aloft releases additional latent heat at the upper level of outer rainbands and invigorates convection (positive values of latent heating and vertical velocity difference seen in Fig. 5.9). The higher cloud and ice water content in POLLU case than CLEAN case suggest the more efficient mixed- and ice-phase cloud processes over its outer rainbands (Fig. 5.8). The invigoration of outer rainbands might also result in small thermodynamic instability (equivalent potential temperature, θ_e) at a low level (Fig. 5.9), reducing warm and moist air supply into the center and thus weakening hurricane peak intensity.
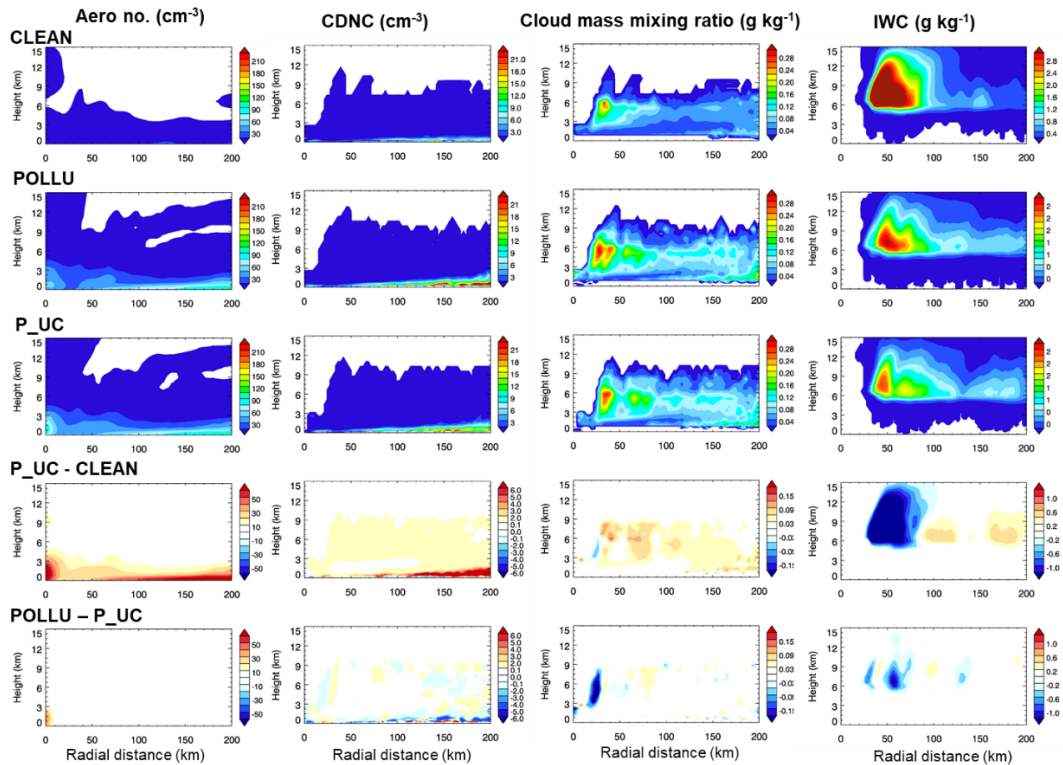
Figure 5.8 Aerosol impacts on cloud microphysical response at 33hr for CLEAN, POLLU and P_UC cases and the difference between P_UC and the difference between CLEAN and POLLU. All parameters are azimuthal averages.

Because of the storm core weakening and rainbands invigorating, the fluid at surface expands in the horizontal direction in order to maintain mass continuity. Fig. 5.9 shows that the region with high vortices shrinks in the vertical direction as the aerosol loading increases and reveals that the vortices are reduced in the storm core (less than 30 km) and enhanced over outer rainbands (50 – 100 km) in the polluted condition. Note that the negative differences at inner radii and positive ones at outer radii for tangential velocities again imply that the storm vortex horizontally shift outward and the circulation expands horizontally.
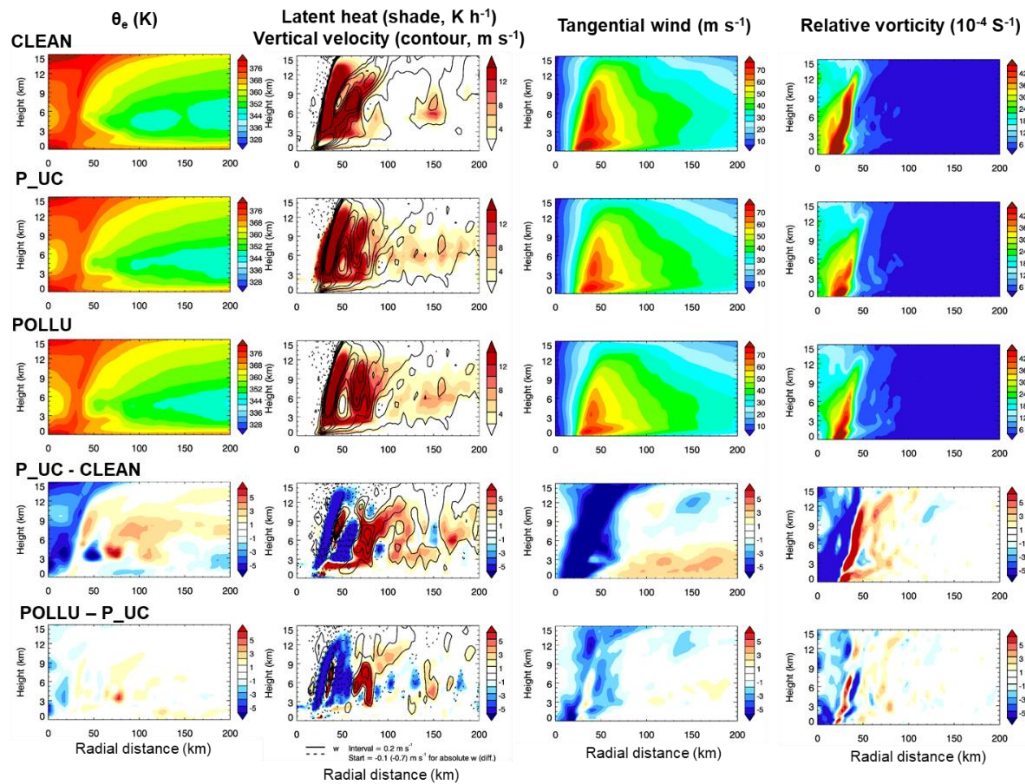
Figure 5.9 Same as Figure 5.6 but for aerosol-induced thermodynamic and dynamic feedback. θ_e denotes the equivalent potential temperature (unit is K).

In order to evaluate the ocean coupling effect on the storm at different hurricane stages, a stage from 18 to 36 hr (S1), representing the rapid intensification period, and a stage from 42 to 55 hr (S2), representing the mature period, are identified according to the evolution of hurricane peak intensity. To examine how the aerosols, hurricane, and ocean interact with each other, here we analyze the responses of storm structure to aerosol and ocean coupling effects.

Figs. 5.10 and 5.11 illustrates the azimuthally-averaged radial profiles of surface wind, surface wind stress, SST, total surface heat fluxes, and SLP for S1 and S2. During S1, the aerosol effect mainly shows a weakening of the peak intensity. While during S2 when the aerosol effect is still significant, the storm structure is also altered, i.e. the surface wind is weaker over the region near the hurricane center and stronger far away from the hurricane center under polluted condition (Fig. 5.10b). Correspondingly, the azimuthally-averaged mean of SLP is lower in the storm core and higher at the periphery in POLLU case than CLEAN case (Fig. 5.11d). The changes in radial profiles of sea-level pressure and surface wind can be explained by the aerosol-induced weakening of the storm and the expansion of the storm circulation, which leads to an outward shift of the eyewall position and thus modifications on the horizontal distributions of sea-level pressure and surface wind.
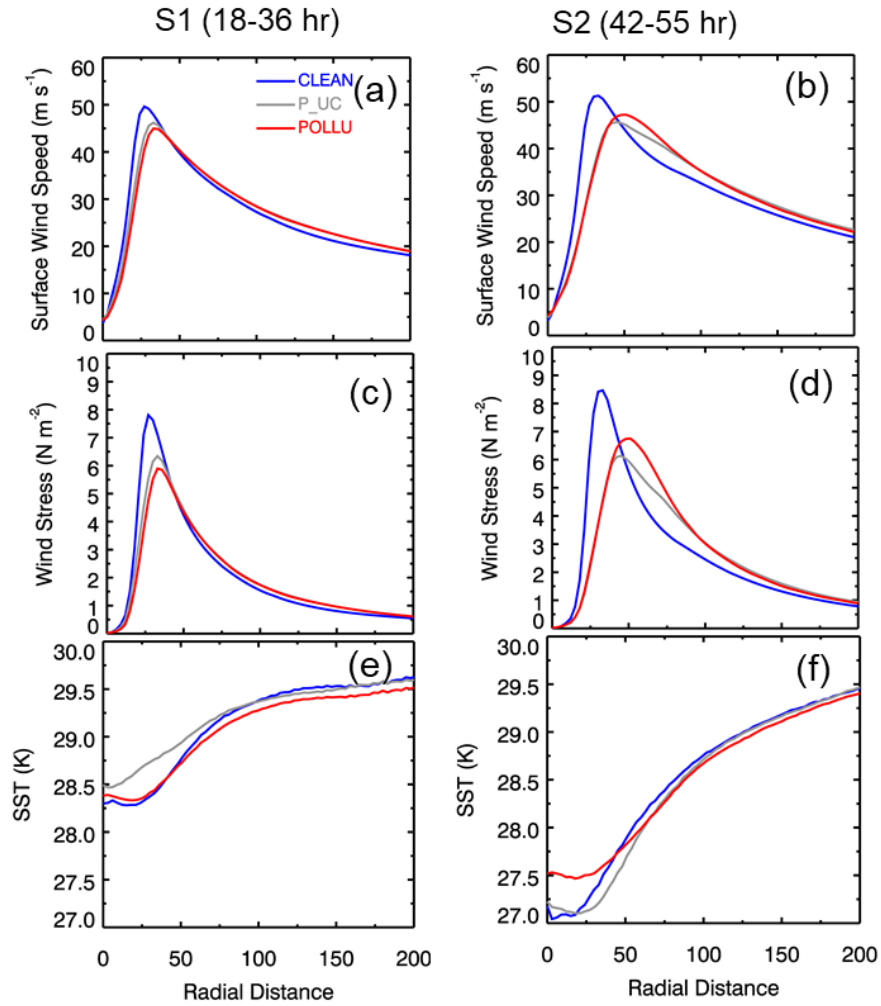
Figure 5.10 Azimuthally-averaged radial profile of hurricane storm structure in CLEAN, P_UC, and POLLU cases during S1 (a, c, e, g, and i, the rapid intensifying stage) and S2 (b, d, f, h, and j, the mature stage). (a) and (b) are for surface wind; (c) and (d) are for surface wind stress; (e) and (f) are for SST; (g) and (h) are for total heat flux; and (i) and (j) are for sea-level pressure.
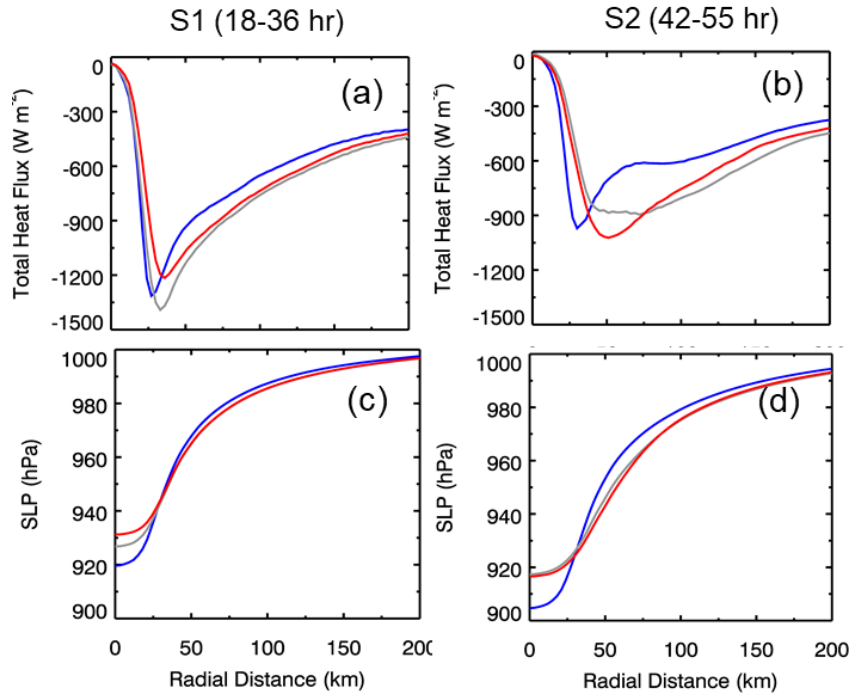
Figure 5.11 Azimuthally-averaged radial profile of hurricane storm structure in CLEAN, P_UC, and POLLU cases during S1 (a, c, e, g, and i, the rapid intensifying stage) and S2 (b, d, f, h, and j, the mature stage). (a) and (b) are for surface wind; (c) and (d) are for surface wind stress; (e) and (f) are for SST; (g) and (h) are for total heat flux; and (i) and (j) are for sea-level pressure.

5.3 Aerosol-induced Feedback of Ocean Coupling and its Importance Relative to

Aerosol Effect

Also shown in Figs. 5.4 are two sets of uncoupled simulations (WRF only) on the aerosol-hurricane interactions, with SST prescribed from two reanalysis datasets, i.e. CFSR and HYCOM. The simulated intensity is different between the two uncoupled runs, implying that the response of a hurricane to aerosol loadings depends on the SST dataset used for driving the model simulations. Therefore, the extent to which the ocean coupling can affect aerosol-hurricane interactions depends on SST and cannot be evaluated simply by contrasting the polluted coupled simulations with the uncoupled one. In order to isolate the

ocean coupling effect from aerosol effects in the ocean-hurricane system, we perform the uncoupled polluted case with SST prescribed from the CLEAN case (i.e., P_UC case). Therefore, the difference between the CLEAN and P_UC cases represents the aerosol indirect effect only. The P_UC case is then compared to the POLLU case to quantitively separate the ocean coupling effect on hurricane from the aerosol effect.

Figure 5.12a shows SST anomalies induced by the coupling effect by differing SST in the POLLU case from the P_UC case. There is a warmer area between 40 – 55 hr in the POLLU case. Since this warm area is mostly near and inside of the eyewall, it corresponds to the region covered by the storm core. This warm area is due to the weak surface winds at the storm core under the polluted condition, leading to small surface wind stress and thus weak upwelling and small cooling at the ocean surface in the POLLU case. In contrast, the SST at the periphery is overall colder in the POLLU case than the P_UC/CLEAN case. The colder periphery is because the location of maximum surface wind stress over ocean displaces more outward along radial direction in the POLLU case than the CLEAN case. Therefore, the upwelling cooling spreads more outward in radial direction in the POLLU case than the CLEAN case. There is no warm area before 40 hr due to the following two reasons: Firstly, the wind stress exerted on ocean surface is relatively weak to cause strong upwelling and associated cooling in ocean upper layer at early stage of hurricane; Secondly, the track shown in the P_UC case shifts a little from the CLEAN case during this period.

The energy from ocean to drive the circulation of hurricane can be evaluated by the amount of exchange of surface total heat flux (latent plus sensible heat flux) between the atmosphere and ocean (Bender et al. 1993). The surface heat flux is affected by the thermodynamic and dynamic condition at atmosphere-ocean interface, including surface

wind speed, SST, and relative humidity (Zhang and Mcphaden 1995). Fig. 5.12b shows the surface heat flux anomalies induced by ocean coupling. During the rapid intensification period (before 40 hr), the heat flux anomalies are positive, meaning that there is small evaporation and thus small latent energy supply to the storm circulation. While during the mature stage (from 40 – 55 hr), the heat flux is negative at storm core but positive at the periphery and far field. Overall, the anomalies of surface total heat flux are well anti-correlated with SST anomalies, indicating that the ocean feedback induced by SST perturbations are responsible for the different exchanging efficiency of latent energy between the POLLU and P_UC cases.

In contrast, the perturbations of surface heat flux are strongly positive at inner core and strongly negative at the periphery, in response to aerosol effect only or the combined effects of aerosol and ocean coupling (Figs. 5.12c and d). We also find that the good anti-correlation existing between anomalies of surface wind (not SST) and surface heat flux in the case of aerosol effect only or combined effects of aerosol and ocean coupling (not shown here). Specifically, the weak (strong) surface wind at storm core (periphery) results in suppressed (intensified) evaporation of water, consistent with the reduction (enhanced) in surface heat flux. The similarity in surface heat flux perturbations between aerosol effect only and the combined effect of aerosol and ocean coupling also suggests that aerosol effect is dominant in determining hurricane intensity when considering the aerosol-ocean-tropical cyclone three-way interaction system.

The relative importance of ocean coupling effect in determining hurricane intensity is evaluated by comparing the mean surface heat flux perturbations induced by ocean coupling and aerosol effect. On average the feedback of ocean coupling compensates the

89

aerosol effect by 59% and 15% in terms of surface heat flux perturbations for S1 and S2, respectively. Apparently, the ocean coupling shows appreciable effect on modulating latent heat energy exchange during hurricane development.
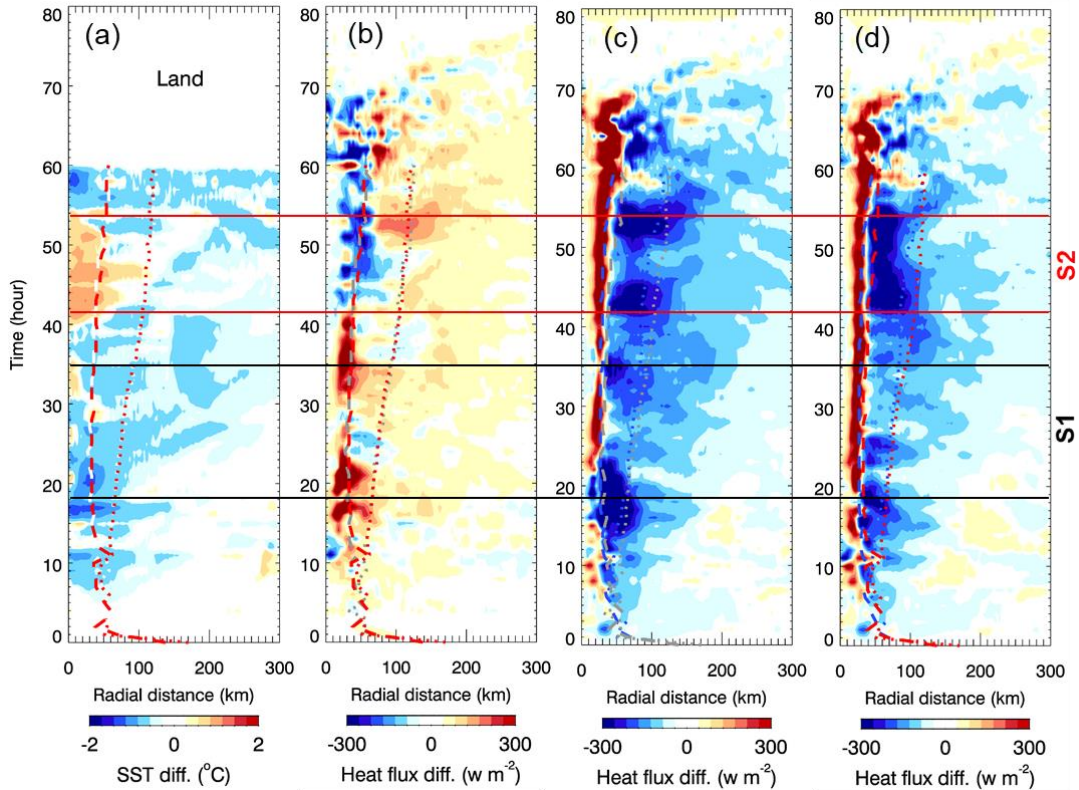
Figure 5.12 Hovmöller diagrams of azimuthally mean for (a) SST differences between the POLLU and P_UC cases and surface total heat flux differences of (b) POLLU - P_UC (ocean coupling feedback), (c) P_UC – CLEAN (aerosol effect only), and (d) POLLU - CLEAN (combined effects of aerosol and ocean coupling). Dash and dot lines denote RMW and the radii of the area covered by hurricane force winds (>34 m s-1), respectively, and their colors (blue, grey, and red) represent different cases (CLEAN, P_UC, and POLLU, respectively).

As depicted in Figs. 5.7a and b, the higher minimum SLP and smaller maximum wind speed in the P_UC case than the CLEAN case indicate that inclusion of aerosol effect

only can induce great weakening of the hurricane. When the ocean feedback is included in simulation (i.e. the POLLU case), the minimum sea-level pressure increases further during hurricane development stage (from 15 – 42 hr) and decrease a little at mature stage (from 45 – 60 hr), relative to the P_UC case. The inconsistent changes in hurricane peak intensity throughout hurricane lifecycle suggest that the aerosol-induced ocean coupling effect shows both positive and negative feedbacks, depending on hurricane development stage. The reasons leading to ocean positive and negative feedbacks will be explained in follow paragraph. Also, from Figs. 5.7d and e, the expansion of storm circulation is attributed primarily to the aerosol effect only. Overall, the changes in hurricane properties caused by aerosol-induced air-sea interactions are smaller than that induced by the aerosol effect only, but the ocean coupling effect still plays a role in modulating the hurricane response to aerosols.

As depicted in Figs. 5.10a and c, the surface wind and associated wind stress is slightly reduced in polluted cases compared to the clean case because of the weakening effect of aerosol during S1. Correspondingly, there is neglectable change in SST from the CLEAN case to the POLLU case (Fig. 5.10e). But the SST at the inner storm core in the P_UC case is a little warmer compared to the POLLU case, which is due to the slight shift of track caused by the aerosol effect in the P_UC case from the CLEAN case. This warming of SST leads to large latent energy transferred from the ocean to the storm system, and further enhance the pressure depression in the P_UC case compared to the POLLU case (Fig. 5.10i). While during S2, SST warms by as much as 0.5 °C at storm core in the POLLU case compared to the CLEAN case. This warming of SST in the POLLU case is consistent with the considerable decrease in wind speed and associated wind stress in the POLLU case

relative to the CLEAN case. The higher SST at the inner core favors more efficient evaporation of ocean water and thus larger latent heat entering into the storm system in the POLLU case than the P_UC case. The additional energy obtained by the storm system in turn slightly intensifies the hurricane peak intensity in the POLLU case, at least for the maximum surface wind speed in the POLLU case compared to P_UC case.

By changing the energy supply, the aerosol and ocean coupling can affect the storm cloud formation and precipitation at the surface. Fig. 5.13 displays the radial distribution of cloud water path (CWP, the vertical integration of all the condensates) and rainfall rate in response to aerosol and ocean coupling effects. It is expected that CWP during S1 is greatly reduced from the CLEAN to the POLLU case (Fig. 5.13a and c), which is mainly due to aerosol effect. The ocean coupling shows appreciable reductions in CWP and rainfall rates when comparing the POLLU and the P_UC case during S2 (Fig. 5.13b and d). More interestingly, if we normalize the radial distance by RMW, the peak of CWP during S2 is clearly away from the unit (the normalized RMW) for the polluted hurricane, while the CWP peak for the polluted case during S1 is located at the RMW. This evident shift of CWP peak location indicates that, in addition to the expansion, the storm cloud structure greatly tilts outward in the radial direction at upper level in polluted condition.
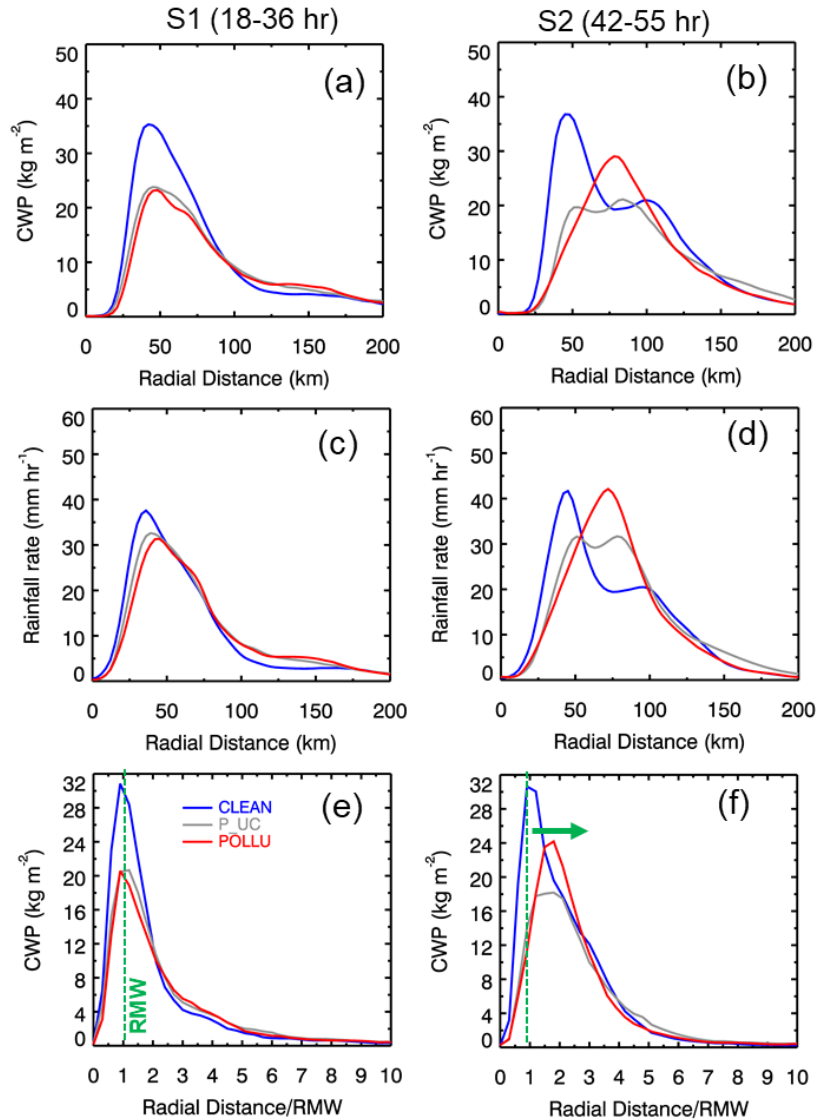
Figure 5.13 Azimuthally-averaged radial profile of storm cloud and precipitation in the CLEAN, P_UC, and POLLU cases during S1 (a and c, the rapid intensifying stage) and S2 (b and d, the mature stage). (a) and (b) are for cloud water path (CWP, vertically integrated of all type condensates); (c) and (d) are for surface precipitation rate; and (e) and (f) are still for CWP but with the radial distance normalized by RMW.

The different responses of CWP to aerosol and ocean coupling at different hurricane stages might be partially explained by the impacts of aerosol and ocean coupling on the thermodynamics and dynamics of storm. Figs. 5.14 and 5.15 display the temporally-

averaged radial distribution of latent heating and vertical velocity under different cases. By comparing S1 (Figs. 14a and e and Figs. 14a and e) to S2 (Figs. 14b and f and Figs. 15b and b), we find that the changes in latent heating and vertical velocity due to the aerosol effect are greater during S2 than the case during S1. Overall, the effect of ocean coupling on storm thermodynamics and dynamics is relatively smaller than the aerosol effect only (Figs. 14b and d and Figs. 15b and d). In addition, the convection is strongly invigorated by ocean coupling effect just outside of eyewall during S2, consistent with the enhancement of CWP and precipitation in the POLLU case relative to the P_UC case shown in Fig. 5.13. The more outward tilting of storm system at upper level during S2 is also evident in the vertical distribution of latent heating and vertical velocity perturbations.

S1 (18-36 hr) **S2 (42-55 hr)**
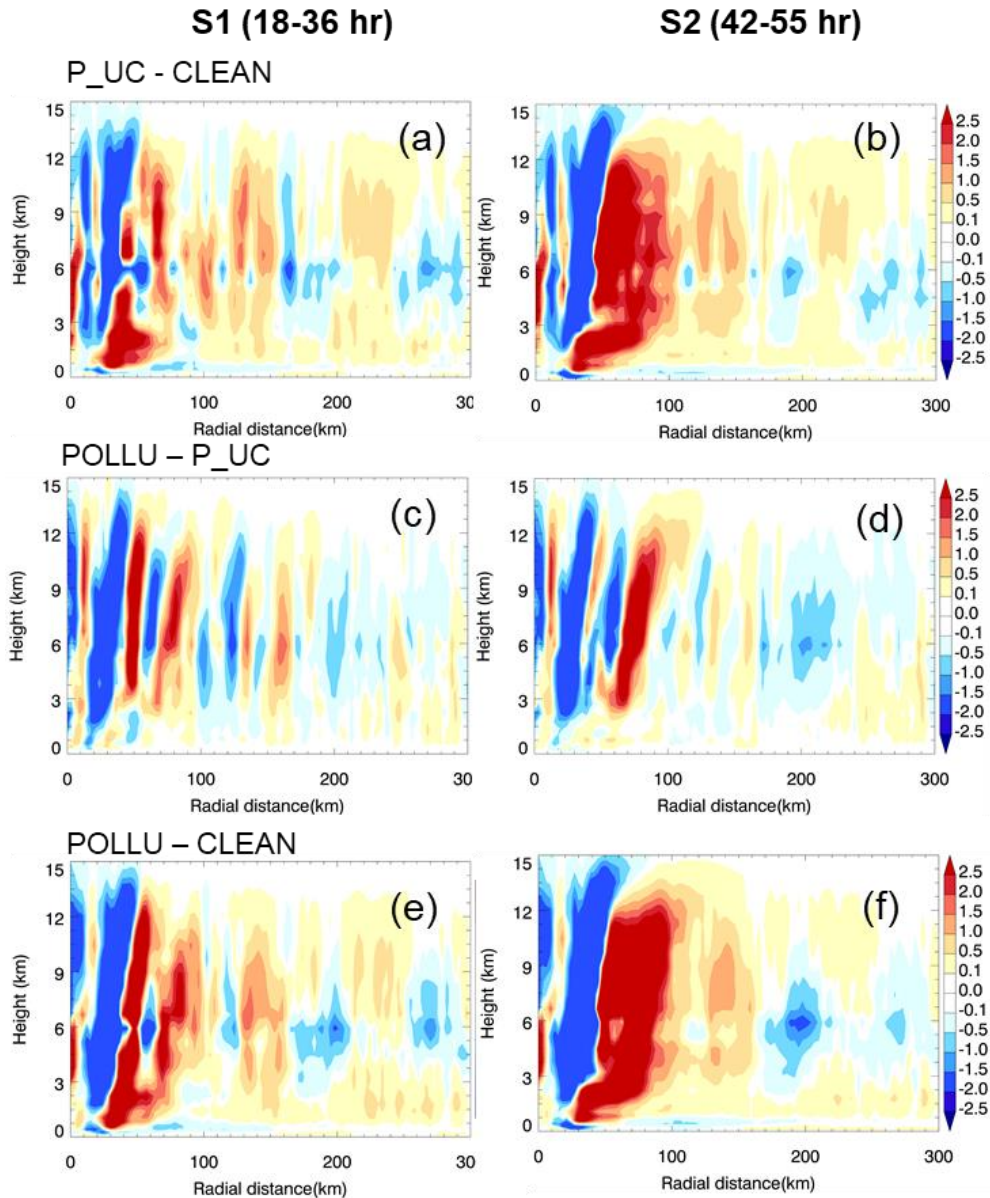
Figure 5.14 Azimuthally-averaged radial profile of latent heating in response to aerosol and ocean coupling effects during S1 (a, c and e, the rapid intensifying stage) and S2 (b, d and f, the mature stage). (a) and (b) are for the perturbations induced by aerosol effect only (P_UC - CLEAN); (c) and (d) are for the perturbations induced by ocean coupling (POLLU - P_UC); and (e) and (f) are for the perturbations induced by the combined effects of aerosol and ocean coupling (POLLU - CLEAN). The black and grey dash lines in (a), (c) and (e) denotes the RMW for clean and polluted conditions.
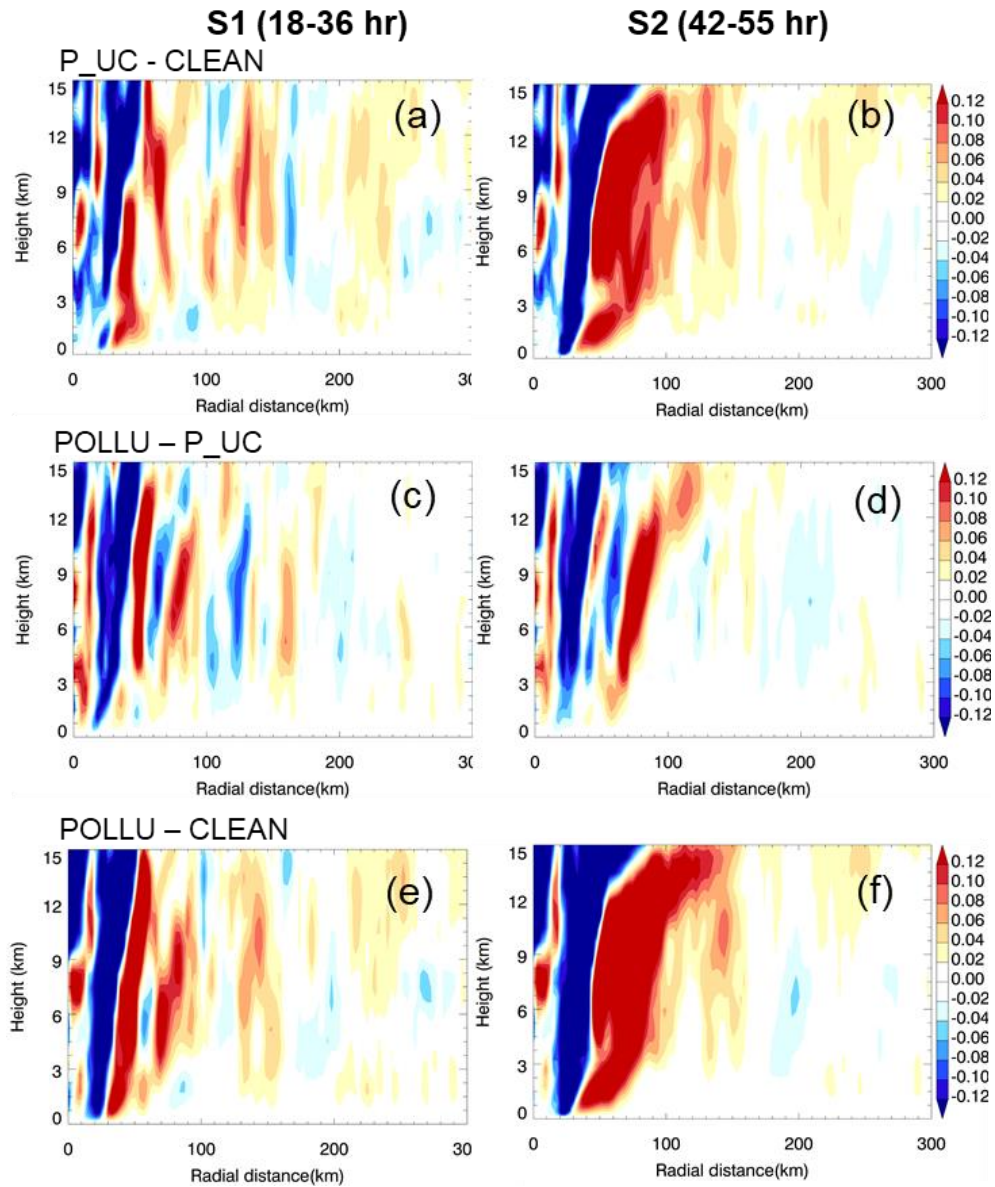
Figure 5.15 Same as Figure 5.12 but for vertical velocity.

5.4 Impacts on Storm Destructiveness

Due to the use of 3-D ocean model (ROMS) we are able to examine the aerosol effects on sea level height (or storm surge). In comparison with tide gauge measurements at Dauphin Island, AL, our simulation captures the peak timing and magnitude of observed sea

96

level height (Fig. 5.16). The simulated peak sea level height at Pass Christian, MS is comparable to the recorded height over there. The differences in sea level height between the POLLU and the CLEAN cases can be as high as 50, 45, and 80 cm at Dauphin Island, New Canal Station, and Pass Christian, respectively. The higher sea level height in polluted condition than the clean condition indicates that the aerosol effect can cause more severe storm surge.
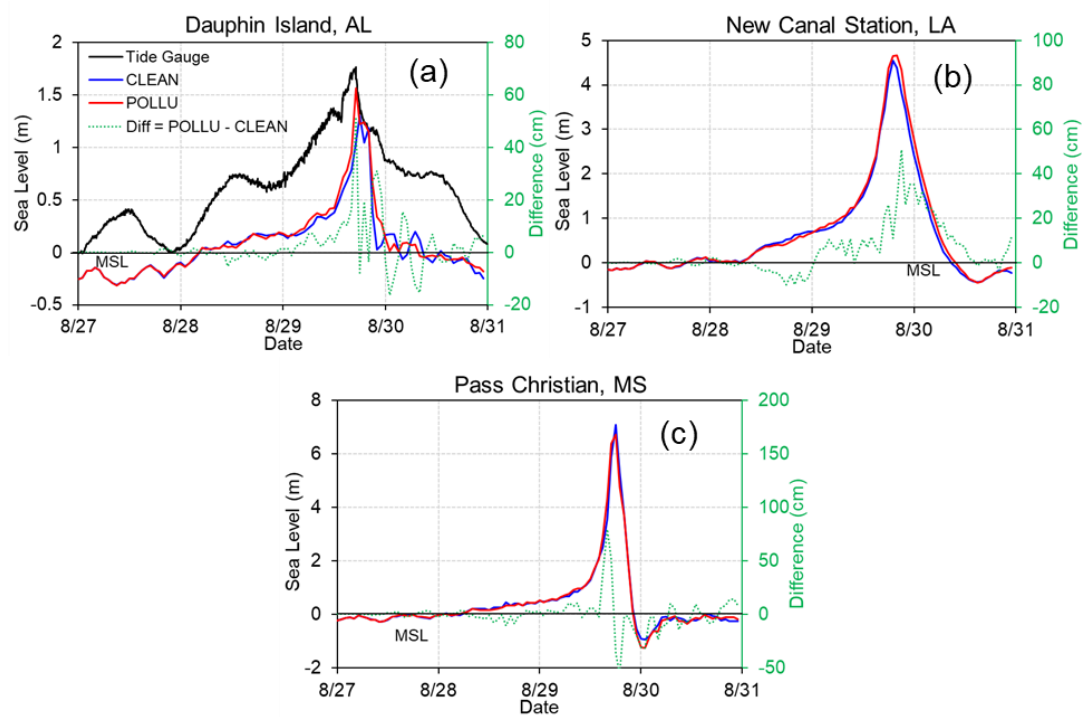
Figure 5.16 The temporal evolution of sea level height in the CLEAN, P_UC, and POLLU cases at three locations. (a) Dauphin Island, AL; (b) New Canal Station, LA; and (c) Pass Christian, MS. The left axis is the absolute sea level height, and the right axis is the difference between POLLU and CLEAN cases.

The storm surge variations under different aerosol scenarios can be most likely linked to the aerosol effects on the wind forces over ocean surface. Fig. 5.17 depicts the sea level height and surface wind speed perturbations at time of 64, 65, and 69 hr, corresponding to the peak time of sea level height at the abovementioned locations. In general, as stronger wind (positive values of wind speed perturbations) blows toward the coastal region, the ocean piles up there and results in higher storm surge (positive values of sea level height perturbation) and vice versa. For example, the higher sea levels at the stations of Pass Christian, MS and Dauphin Island, AL in the POLLU case than the CLEAN are corresponding to the larger wind speed blowing toward the coastal line there.

However, storm surge is sensitive to other properties of storm, including forward speed, size (RMW), the angle of approaching to the coast, and minimum seal-level pressure. Storm surge also is the combined effects of many other factors, including the shape and characteristics of coastal features such as bays and estuaries, the local geography, or the relative position of the interested station to the hurricane track. It is required to conduct more research to understand the physical processes underlying the aerosol effect on sea level height and thus storm surge.
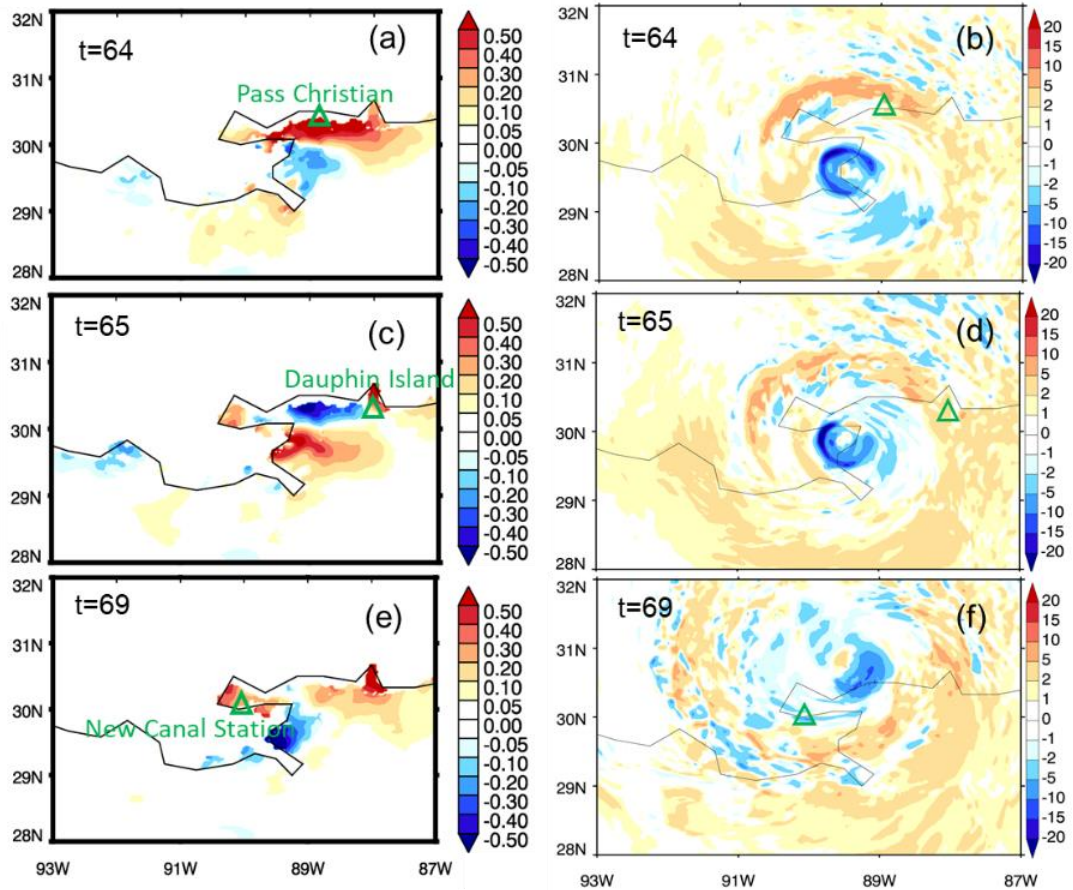
Figure 5.17 The spatial distribution of sea level height (left) and surface wind (right) in response to aerosol effects (POLLU – CLEAN) at three-time points. (a) and (b) t = 64 hr; (c) and (d) t = 65 hr; and (e) and (f) t = 69 hr.

To evaluate the overall destructiveness of storm under different scenarios, the storm destructive potential is estimated following (Powell and Reinhold 2007), in which the integrated kinetic energy (IKE) index is used. The equation for IKE calculation is

$$IKE = \int_V \frac{1}{2}\rho U^2 dV$$

where ρ is air density, U is 10 m wind speed, and V represent a volume with vertical depth of 1 m centered at the 10m-level layer. The IKE_{TS}, for marine winds > tropical storm force

99

(18 m s^{-1}), is specifically used as a proxy for hurricane destructive potential including those from storm surge and wave.

Fig. 5.18a shows that the IKE$_{TS}$ in the POLLU case is 17.8% higher on average than that of the CLEAN case over the entire hurricane lifecycle, and the IKE$_{TS}$ is 11 TJ higher in the POLLU case than the CLEAN case at hurricane landfall. Though the peak intensity of hurricane is greatly reduced in polluted condition, the size of aerosol-perturbed storm is enlarged notably in terms of radius for tropical storm force wind (Fig. 5.18b). In addition, the surface wind over the area covered by tropical storm force wind is stronger in the polluted cases than the clean case (see Fig. 5.16). Because of integrating stronger winds over a larger area, there is more overall destructive energy released by the hurricane in polluted condition. The high IKE in the POLLU case compared to the CLEAN case suggests that the overall intensity of hurricane is enhanced under polluted condition, though the peak intensity decreases in terms of minimum sea-level pressure depression or maximum surface wind speed.

With ocean coupling, the surface wind is stronger at the storm core but weaker at the periphery in the POLLU case than that in the P_UC case during mature stage (Fig. 5.10). But meanwhile the storm has contracted a little because of ocean coupling (Fig. 5.18b). Therefore, the net effect on surface wind and storm size results in a slight decrease in destructive potential during the mature stage. For example, the destructive potential is reduced by 5% on average between 45 hr -65 hr in the POLLU case compared to the P_UC case. The ocean coupling effect could be more significant as more aerosols are involved in the hurricane. For example, the reduction in destructive potential by ocean coupling can increase to 11% as aerosol concentration is enhanced to 2000 cm^{-3} (not shown).

100
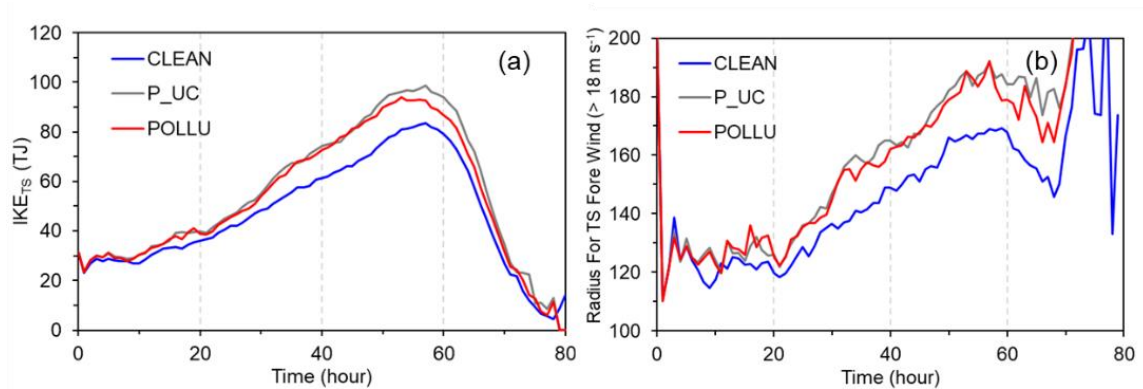
Figure 5.18 Temporal evolution of (a) the radius of area with marine winds > tropical storm force (18 m s–1) and (b) IKE for marine winds > tropical storm force (IKE_TS) for CLEAN, POLLU, and P_UC cases. The IKETS is used as a proxy for storm surge and wave destructive potential.

5.5 Summary

In this study, we conduct modeling simulations to investigate aerosol effects on hurricane development using regional atmosphere-ocean cloud-resolving model, WRF-ROMS. The horizontal grid spacing is set up as 3 km. Hurricane Katrina is taken as a case study. The land-sea contrast in aerosol initial condition is based on MODIS AOD prior to and during Katrina passage. Two aerosol scenarios are simulated, including 200 cm^{-3} for clean condition and 2000 cm^{-3} for polluted case. All the simulations start from 27 August and end on 31 August 2005. The feedback of ocean coupling is isolated from aerosol effect by conducting an additional polluted case with SST prescribed from the clean coupled case and then comparing it to the polluted coupled case. The responses of hurricane peak intensity, size, precipitation, and other structural properties of storm to the effects of aerosol and ocean coupling are examined.

101

For the aerosol-hurricane-ocean system, we find that the aerosol effect causes an expansion of storm circulation at the cost of hurricane peak intensity, consistent with previous studies without the inclusion of air-sea interactions. Two different stages during hurricane development are identified with distinct responses to the aerosol and ocean coupling effects, i.e. stage 1 (S1) from 18 hr – 36 hr, representing the rapid intensification period, and stage 2 (S2) from 42 hr – 55 hr, representing the mature stage. In addition to expanding storm circulation, the aerosol effects can also induce more outward tilting of the upper-level portion of a storm.

The aerosol-induced feedback of ocean coupling overall plays a small role in the three-way interactions relative to the aerosol effect only. The ocean coupling can cause a slight decrease in the depression of SLP during S1 and a slight increase in maximum surface wind speed during S2. In addition, the ocean coupling induces significant enhancements in cloud formation and precipitation during S2. The ocean coupling affects the hurricane by altering the SST, which is warming at the storm core when air-sea interactions are included. The SST warming in the polluted coupled case is because the weakened wind at storm core reduces the upwelling cooling in polluted case compared to the clean case. As a result, the warming of SST favors efficient evaporation of ocean water and additional latent energy supply to the storm, which then would intense winds and in turn cools water. For the hurricane case under study, the aerosol-induced ocean coupling effect show a clear influence on hurricane after the simulation starts 40 hr.

Both the storm surge and storm destructive potential tend to be exacerbated by the aerosol effect. The storm destructive potential can be significantly enhanced on average from clean to polluted cases. The severe storm surge or storm destructiveness is mostly likely due

102

to the storm circulation expansion and thus corresponding modulations on structure (e.g. wind radial profile) under polluted condition. The ocean coupling can reduce the destructive potential during the hurricane landfall. Therefore, the discrepancy in destructive potential estimation between with and without ocean coupling cannot be ignored, particularly in regions with heavy pollution like East Asia.

To test the robustness of the conclusions drawn in this study, more hurricane or tropical cyclone cases should be selected for studying aerosol and ocean coupling effects. In addition, the continental aerosols in this study are simplified as consisting of pure ammonium sulfate, which is far away from the real-world situation where aerosols containing different chemical composition. Also, the spatial distribution of aerosol initial number concentration is simplified, which might result in biases when evaluating the aerosol effect on hurricane development. Therefore, more detailed and comprehensive considerations of aerosol components and aerosol spatial distribution are needed in future work.

6. CONCLUSIONS

This study aims to quantitatively assess the regional-scale aerosol effects under various weather conditions. Firstly, the aerosol microphysical and radiative effects on the continental cloud complex during the RACORO field campaign were separately studied. The aerosol effects due to cloud transition and the aerosol net effects on the cloud complex are particularly evaluated. Secondly, the characteristics of the formation and evolution of severe haze in China have been elucidated on the basis of field measurements. The regional climate effects under extremely hazy condition have been estimated by conducting case studies with the WRF model coupled with an explicit aerosol radiative module. Two typical severe haze episodes occurring in fall of 2013 in Beijing, China, and the interactions between severe haze and PBL as well as aerosol/BC radiative forcing are quantitatively examined. Particularly, the role of BC aging in aerosol-PBL interactions and its contribution to net aerosol radiative forcing during severe haze periods are evaluated. Thirdly, to investigate the aerosol-hurricane-ocean three-way interactions by performing modeling studies on Hurricane Katrina 2005 using a regional three-dimensional atmosphere-ocean coupled model, WRF-ROMS. By contrasting a coupled simulation of the polluted hurricane and an uncoupled one with SST from the outputs of the corresponding clean coupled case, the aerosol-induced ocean coupling effect is isolated from aerosol-hurricane interactions for the first time.

The modeling studies on the continental cloud complex, consisting of shallow cumuli, DCC, and stratus cloud reveal that, under an elevated aerosol loading with AME only, a reduced cloudiness for the shallow cumuli and stratus results from more droplet evaporation competing with suppressed precipitation, but an enhanced cloudiness for the

104

DCC is attributed to more condensation. With the inclusion of ARE, the shallow cumuli are suppressed due to the thermodynamic effects of light-absorbing aerosols. The responses of DCC and stratus to aerosols are monotonic with AME only but non-monotonic with both AME and ARE. The DCC is invigorated because of favorable convection and moisture conditions at night induced by daytime ARE, via the so-called "aerosol-enhanced conditional instability" mechanism. Overall, inclusion of ARE tends to greatly change the sensitivity and monotonicity of cloud responses to aerosols, especially when environmental feedbacks due to aerosol effects on preceding clouds are considered. The results reveal that the overall aerosol effects on the cloud complex are distinct from the individual cloud types, highlighting that aerosol-cloud interactions for the diverse cloud regimes and their transitions need to be evaluated in order to accurately assess the regional and global climatic impacts.

China has been experiencing increasingly severe regional haze associated with a periodic cycle of heavy PM pollution. Here we elucidate the spatiotemporal characteristics of PM pollution during two typical severe haze episodes over NCP and evaluate the intensity of photochemical activities in Beijing as well as the interactions between the elevated level PM and PBL to better understand how severe haze forms in China. During severe haze, it is found that the region with high values of satellite-retrieved aerosol optical depth (AOD) centers at megacities like Beijing over NCP, distinct from the spatial distribution pattern of seasonal and annual mean. The observed [OOA] is well correlated with the odd-oxygen concentration ($[O_x]$) during the clean-to-hazy transition periods; and the $[OOA]/[O_x]$ ratio in Beijing is 2.4 and 5.1 times higher than the case of Mexico City and Houston, respectively. The higher $[OOA]/[O_x]$ ratio corresponds to more intensive photochemical activities taking

place in Beijing than the other two megacities. Modeling studies using Weather Research and Forecasting coupled with an explicit aerosol radiative module indicate that the strong aerosol-PBL interactions during severe haze result in a greatly suppressed and stabilized boundary layer with higher humidity, triggering a positive feedback loop to amplify PM pollution. For the two severe haze episodes under study, the heavy loading PM induces a negative TOA forcing of -5.6 ~ -5.9 W m^{-2}, a result of the strong cooling at surface largely canceled out by the strong heating in the atmosphere. The aging of BC can contribute more than 40% of PBL collapse induced by total aerosols and about 50% of TOA positive forcing caused by total BC during severe haze, suggesting the importance of BC aging in aerosol-PBL interactions and aerosol regional climate effect under extremely hazy condition.

Hurricane Katrina 2005 is simulated using the regional three-dimensional atmosphere-ocean coupled model, i.e., WRF-ROMS, to investigate the aerosol-hurricane-ocean three-way interactions. For the aerosol-hurricane-ocean system, the aerosol effect causes an expansion of storm circulation at the cost of hurricane peak intensity, showing a larger size of storm circulation and more outward shift of eyewall under polluted condition. Aerosol-induced feedback of ocean coupling can be inferred from the contrast between the polluted coupled and uncoupled simulations; it overall plays a secondary role in the three-way interactions. There is more appreciable influence induced by the ocean coupling during the mature stage than the rapid intensification stage. During the mature stage, the ocean coupling shows an enhancing effect on CWP and precipitation. This is attributed to the positive SST perturbations at the storm core caused by the considerable changes in surface wind and wind stress from clean to polluted cases. The higher SST is responsible the more efficient latent heat transfer from ocean to storm system. In addition, by examining the

differences between clean and polluted coupled simulations, the storm surge or storm destructiveness tends to be exacerbated by aerosol effect due to the circulation expansion and corresponding modulations of the TC structure under polluted condition.

REFERENCES

Abdul-Razzak, H., S. J. Ghan, and C. Rivera-Carpio, 1998: A parameterization of aerosol activation - 1. Single aerosol type. *J Geophys Res*, **103,** 6123-6131.

Ackerman, A. S., O. B. Toon, D. E. Stevens, A. J. Heymsfield, V. Ramanathan, and E. J. Welton, 2000: Reduction of tropical cloudiness by soot. *Science*, **288,** 1042-1047.

Albrecht, B. A., 1989: Aerosols, cloud microphysics, and fractional cloudiness. *Science*, **245,** 1227-1230.

Allen, R. J., and S. C. Sherwood, 2010: Aerosol-cloud semi-direct effect and land-sea temperature contrast in a GCM. *Geophys Res Lett*, **37,** L07702.

Andreae, M. O., D. Rosenfeld, P. Artaxo, A. A. Costa, G. P. Frank, K. M. Longo, and M. A. F. Silva-Dias, 2004: Smoking rain clouds over the Amazon. *Science*, **303,** 1337-1342.

Atkinson, R., 2000: Atmospheric chemistry of VOCs and NOx. *Atmos Environ*, **34,** 2063-2101.

Bender, M. A., I. Ginis, and Y. Kurihara, 1993: Numerical simulations of tropical cyclone-ocean interaction with a high-resolution coupled model. *J Geophys Res*, **98,** 23245-23263.

Bigg, E. K., 1953: The formation of atmospheric ice crystals by the freezing of droplets. *Q J Roy Meteorol Soc*, **79,** 510-519.

Bond, D. W., S. Steiger, R. Y. Zhang, X. X. Tie, and R. E. Orville, 2002: The importance of NOx production by lightning in the tropics. *Atmos Environ*, **36,** 1509-1519.

Bond, T. C., S. J. Doherty, D. W. Fahey, P. M. Forster, T. Berntsen, B. J. DeAngelo, M. G. Flanner, S. Ghan, B. Kärcher, D. Koch, S. Kinne, Y. Kondo, P. K. Quinn, M. C. Sarofim, M. G. Schultz, M. Schulz, C. Venkataraman, H. Zhang, S. Zhang, N. Bellouin, S. K. Guttikunda, P. K. Hopke, M. Z. Jacobson, J. W. Kaiser, Z. Klimont, U. Lohmann, J. P. Schwarz, D. Shindell, T. Storelvmo, S. G. Warren, and C. S. Zender, 2013: Bounding the role of black carbon in the climate system: A scientific assessment. *J Geophys Res*, **118,** 5380-5552.

Cai, W., K. Li, H. Liao, H. Wang, and L. Wu, 2017: Weather conditions conducive to Beijing severe haze more frequent under climate change. *Nat Clim Change*, **7,** 257.

Charlson, R. J., and M. J. Pilat, 1969: Climate: The Influence of aerosols. *J Appl Meteorol*, **8,** 1001-1002.

Che, H., X. Xia, J. Zhu, Z. Li, O. Dubovik, B. Holben, P. Goloub, H. Chen, V. Estelles, E. Cuevas-Agullo, L. Blarel, H. Wang, H. Zhao, X. Zhang, Y. Wang, J. Sun, R. Tao, X. Zhang, and G. Shi, 2014: Column aerosol optical properties and aerosol radiative forcing during a serious haze-fog month over North China Plain in 2013 based on ground-based sunphotometer measurements. *Atmos Chem Phys*, **14,** 2125-2138.

Chou, M. D., and M. J. Suarez, 1999: A solar radiation parameterization for atmospheric studies. Technical Report, NASA/TM-1999-104606/VOL15.

Coakley, J. A., R. D. Cess, and F. B. Yurevich, 1983: The Effect of tropospheric aerosols on the Earth's radiation budget: A parameterization for climate models. *J Atmos Sci*, **40,** 116-138.

Cotton, W. R., G. M. Krall, and G. G. Carrio, 2012: Potential indirect effects of aerosol on tropical cyclone intensity: Convective fluxes and cold-pool activity. *Tropical Cyclone Res Rev*, **1,** 293-306.

DeMott, P. J., O. Mohler, O. Stetzer, G. Vali, Z. Levin, M. D. Petters, M. Murakami, T. Leisner, U. Bundke, H. Klein, Z. A. Kanji, R. Cotton, H. Jones, S. Benz, M. Brinkmann, D. Rzesanke, H. Saathoff, M. Nicolet, A. Saito, B. Nillius, H. Bingemer, J. Abbatt, K. Ardon, E. Ganor, D. G. Georgakopoulos, and C. Saunders, 2011: Resurgence in ice nuclei measurement research. *Bull Am Meteorol Soc*, **92,** 1623.

Ding, A. J., X. Huang, W. Nie, J. N. Sun, V. M. Kerminen, T. Petäjä, H. Su, Y. F. Cheng, X. Q. Yang, M. H. Wang, X. G. Chi, J. P. Wang, A. Virkkula, W. D. Guo, J. Yuan, S. Y. Wang, R. J. Zhang, Y. F. Wu, Y. Song, T. Zhu, S. Zilitinkevich, M. Kulmala, and C. B. Fu, 2016: Enhanced haze pollution by black carbon in megacities in China. *Geophys Res Lett*, **43,** 2873–2879.

Dodla, V. B., S. Desamsetti, and A. Yerramilli, 2011: A comparison of HWRF, ARW and NMM models in Hurricane Katrina (2005) simulation. *Int J Environ Res Public Health*, **8,** 2447-2469.

Emanuel, K., C. DesAutels, C. Holloway, and R. Korty, 2004: Environmental Control of Tropical Cyclone Intensity. *J Atmos Sci*, **61,** 843-858.

Fan, J., R. Y. Zhang, G. H. Li, J. Nielsen-Gammon, and Z. Q. Li, 2005: Simulations of fine particulate matter (PM2.5) in Houston, Texas. *J Geophys Res*, **110,** D16203.

Fan, J., R. Zhang, G. Li, W.-K. Tao, and X. Li, 2007a: Simulations of cumulus clouds using a spectral microphysics cloud-resolving model. *J Geophys Res*, **112,** D04201.

Fan, J., R. Y. Zhang, G. H. Li, and W. K. Tao, 2007b: Effects of aerosols and relative humidity on cumulus clouds. *J Geophys Res*, **112,** D14204.

Fan, J., R. Zhang, W.-K. Tao, and K. I. Mohr, 2008: Effects of aerosol optical properties on deep convective clouds and radiative forcing. *J Geophys Res*, **113,** D08209.

Fan, J., L. R. Leung, D. Rosenfeld, Q. Chen, Z. Li, J. Zhang, and H. Yan, 2013: Microphysical effects determine macrophysical response for aerosol impacts on deep convective clouds. *Proc Natl Acad Sci U S A*, **110,** E4581-4590.

Fan, J., D. Rosenfeld, Y. Yang, C. Zhao, L. R. Leung, and Z. Q. Li, 2015: Substantial contribution of anthropogenic air pollution to catastrophic floods in Southwest China. *Geophys Res Lett*, **42,** 6066-6075.

Ghan, S. J., L. R. Leung, R. C. Easter, and K. AbdulRazzak, 1997: Prediction of cloud droplet number in a general circulation model. *J Geophys Res*, **102,** 21777-21794.

Grant, L. D., and S. C. van den Heever, 2014: Aerosol-cloud-land surface interactions within tropical sea breeze convection. *J Geophys Res*, **119,** 8340-8361.

——, 2015: Cold pool and precipitation responses to aerosol loading: Modulation by dry layers. *J Atmos Sci*, **72,** 1398-1408.

Guo, S., M. Hu, M. L. Zamora, J. Peng, D. Shang, J. Zheng, Z. Du, Z. Wu, M. Shao, L. Zeng, M. J. Molina, and R. Zhang, 2014: Elucidating severe urban haze formation in China. *Proc Natl Acad Sci U S A*, **111,** 17373-17378.

Gustafsson, Ö., and V. Ramanathan, 2016: Convergence on climate warming by black carbon aerosols. *Proc Nat Acad Sci USA*, **113,** 4243-4245.

Hansen, J., M. Sato, and R. Ruedy, 1997: Radiative forcing and climate response. *J Geophys Res*, **102,** 6831-6864.

He, C., K. N. Liou, Y. Takano, R. Zhang, M. Levy Zamora, P. Yang, Q. Li, and L. R. Leung, 2015: Variation of the radiative properties during black carbon aging: theoretical and experimental intercomparison. *Atmos Chem Phys*, **15,** 11967-11980.

Herbener, S. R., S. C. v. d. Heever, G. G. Carrió, S. M. Saleeby, and W. R. Cotton, 2014: Aerosol indirect effects on idealized tropical cyclone dynamics. *J Atmos Sci*, **71,** 2040-2055.

Hong, S. Y., Y. Noh, and J. Dudhia, 2006: A new vertical diffusion package with an explicit treatment of entrainment processes. *Mon Wea Rev*, **134,** 2318-2341.

IPCC, 2013: *Climate Change 2013: The Physical Science Basis. Contribution of Working Group I to the Fifth Assessment Report of the Intergovernmental Panel on Climate Change.* Cambridge University Press, 1535 pp, Cambridge, United Kingdom and New York, NY, USA.

Jiang, H., and G. Feingold, 2006: Effect of aerosol on warm convective clouds: Aerosol-cloud-surface flux feedbacks in a new coupled large eddy model. *J Geophys Res*, **111,** n/a-n/a.

Jiang, J. H., H. Su, C. Zhai, S. T. Massie, M. R. Schoeberl, P. R. Colarco, S. Platnick, Y. Gu, and K. N. Liou, 2011: Influence of convection and aerosol pollution on ice cloud particle effective radius. *Atmos Chem Phys*, **11,** 457-463.

Johnson, B. T., K. P. Shine, and P. M. Forster, 2004: The semi-direct aerosol effect: Impact of absorbing aerosols on marine stratocumulus. *Q J Roy Meteorol Soc*, **130,** 1407-1422.

Kaufman, Y. J., I. Koren, L. A. Remer, D. Rosenfeld, and Y. Rudich, 2005: The effect of smoke, dust, and pollution aerosol on shallow cloud development over the Atlantic Ocean. *Proc Nat Acad Sci USA*, **102,** 11207-11212.

Khain, A., B. Lynn, and J. Dudhia, 2010: Aerosol effects on intensity of landfalling hurricanes as seen from simulations with the WRF model with spectral bin microphysics. *J Atmos Sci*, **67,** 365-384.

Khain, A., B. Lynn, and J. Shpund, 2016: High resolution WRF simulations of Hurricane Irene: Sensitivity to aerosols and choice of microphysical schemes. *Atmos Res*, **167,** 129-145.

Khain, A. P., and I. Ginis, 1991: The mutual response of a moving tropical cyclone and the ocean. *Beitr Phys Atmos*, **64,** 125-141.

Khain, A. P., D. Rosenfeld, and A. Pokrovsky, 2005: Aerosol impact on the dynamics and microphysics of deep convective clouds. *Q J Roy Meteorol Soc*, **131,** 2639-2663.

Khain, A. P., N. BenMoshe, and A. Pokrovsky, 2008: Factors determining the impact of aerosols on surface precipitation from clouds: An attempt at classification. *J Atmos Sci*, **65,** 1721-1748.

Khain, A. P., 2009: Notes on state-of-the-art investigations of aerosol effects on precipitation: a critical review. *Environ Res Lett*, **4,** 015004.

Kogan, Y. L., D. B. Mechem, and K. Choi, 2012: Effects of Sea-Salt Aerosols on Precipitation in Simulations of Shallow Cumulus. *J Atmos Sci*, **69,** 463-483.

Lee, S. S., L. J. Donner, and V. T. J. Phillips, 2009: Sensitivity of aerosol and cloud effects on radiation to cloud types: comparison between deep convective clouds and warm stratiform clouds over one-day period. *Atmos Chem Phys*, **9,** 2555-2575.

Lee, S. S., L. J. Donner, and J. E. Penner, 2010: Thunderstorm and stratocumulus: how does their contrasting morphology affect their interactions with aerosols? *Atmos Chem Phys*, **10,** 6819-6837.

Lee, S. S., and G. Feingold, 2013: Aerosol effects on the cloud-field properties of tropical convective clouds. *Atmos Chem Phys*, **13,** 6713-6726.

Lei, W. F., A. Derecskei-Kovacs, and R. Y. Zhang, 2000: Ab initio study of OH addition reaction to isoprene. *J Chem Phys*, **113,** 5354-5360.

Levy, M. E., R. Y. Zhang, A. F. Khalizov, J. Zheng, D. R. Collins, C. R. Glen, Y. Wang, X. Y. Yu, W. Luke, J. T. Jayne, and E. Olaguer, 2013: Measurements of submicron aerosols in Houston, Texas during the 2009 SHARP field campaign. *J Geophys Res*, **118,** 10518-10534.

Levy, R. C., G. G. Leptoukh, R. Kahn, V. Zubko, A. Gopalan, and L. A. Remer, 2009: A critical look at deriving monthly aerosol optical depth from satellite data. *IEEE Trans Geosci Remote Sens*, **47,** 2942-2956.

Li, G., Y. Wang, K.-H. Lee, Y. Diao, and R. Zhang, 2008a: Increased winter precipitation over the North Pacific from 1984–1994 to 1995–2005 inferred from the Global Precipitation Climatology Project. *Geophys Res Lett*, **35,** L13821.

Li, G., Y. Wang, and R. Zhang, 2008b: Implementation of a two-moment bulk microphysics scheme to the WRF model to investigate aerosol-cloud interaction. *J Geophys Res*, **113,** D15211.

Li, G., Y. Wang, K.-H. Lee, Y. Diao, and R. Zhang, 2009: Impacts of aerosols on the development and precipitation of a mesoscale squall line. *J Geophys Res*, **114,** D17205.

Li, J. N., K. von Salzen, Y. R. Peng, H. Zhang, and X. Z. Liang, 2013: Evaluation of black carbon semi-direct radiative effect in a climate model. *J Geophys Res*, **118,** 4715-4728.

Li, P., R. Yan, S. Yu, S. Wang, W. Liu, and H. Bao, 2015: Reinstate regional transport of PM2.5 as a major cause of severe haze in Beijing. *Proc Nat Acad Sci USA*, **112,** E2739-E2740.

Li, Z., X. Xia, M. Cribb, W. Mi, B. Holben, P. Wang, H. Chen, S.-C. Tsay, T. F. Eck, F. Zhao, E. G. Dutton, and R. E. Dickerson, 2007: Aerosol optical properties and their radiative effects in northern China. *J Geophys Res*, **112,** D22S01.

Li, Z., J. Guo, A. Ding, H. Liao, J. Liu, Y. Sun, T. Wang, H. Xue, H. Zhang, and B. Zhu, 2017: Aerosol and boundary-layer interactions and impact on air quality. *Nat Sci Rev*, **4,** 810-833.

Li, Z. Q., F. Niu, J. W. Fan, Y. G. Liu, D. Rosenfeld, and Y. N. Ding, 2011: Long-term impacts of aerosols on the vertical development of clouds and precipitation. *Nat Geosci*, **4,** 888-894.

Lim, K.-S. S., and S.-Y. Hong, 2010: Development of an effective double-moment cloud microphysics scheme with prognostic cloud condensation nuclei (CCN) for weather and climate models. *Mon Wea Rev*, **138,** 1587-1612.

Lin, J. C., T. Matsui, R. A. Pielke, and C. Kummerow, 2006: Effects of biomass-burning-derived aerosols on precipitation and clouds in the Amazon Basin: a satellite-based empirical study. *J Geophys Res*, **111,** D19204.

Lin, Y., Y. Wang, B. Pan, J. Hu, Y. Liu, and R. Zhang, 2016: Distinct Impacts of Aerosols on an Evolving Continental Cloud Complex during the RACORO Field Campaign. *J Atmos Sci*, **73,** 3681-3700.

Lindeman, J. D., Z. Boybeyi, and I. Gultepe, 2011: An examination of the aerosol semi-direct effect for a polluted case of the ISDAC field campaign. *J Geophys Res*, **116,** D00T10.

Liu, X. G., J. Li, Y. Qu, T. Han, L. Hou, J. Gu, C. Chen, Y. Yang, X. Liu, T. Yang, Y. Zhang, H. Tian, and M. Hu, 2013: Formation and evolution mechanism of regional haze: a case study in the megacity Beijing, China. *Atmos Chem Phys*, **13,** 4501-4514.

Liu, Y., and P. H. Daum, 2002: Anthropogenica erosols - Indirect warming effect from dispersion forcing. *Nature*, **419,** 580-581.

Lu, C. S., S. J. Niu, Y. G. Liu, and A. M. Vogelmann, 2013: Empirical relationship between entrainment rate and microphysics in cumulus clouds. *Geophys Res Lett*, **40,** 2333-2338.

Lynn, B. H., A. P. Khain, J. W. Bao, S. A. Michelson, T. Yuan, G. Kelman, D. Rosenfeld, J. Shpund, and N. Benmoshe, 2016: The sensitivity of Hurricane Irene to aerosols and ocean coupling: Simulations with WRF spectral bin microphysics. *J Atmos Sci*, **73,** 467-486.

Ma, Z., J. Fei, L. Liu, X. Huang, and X. Cheng, 2013: Effects of the cold core eddy on tropical cyclone intensity and structure under idealized air–sea interaction conditions. *Mon Wea Rev*, **141,** 1285-1303.

Mallet, M., J. C. Roger, S. Despiau, J. P. Putaud, and O. Dubovik, 2004: A study of the mixing state of black carbon in urban zone. *J Geophys Res*, **109,** D04202.

Matsui, T., H. Masunaga, S. M. Kreidenweis, R. A. Pielke, W.-K. Tao, M. Chin, and Y. J. Kaufman, 2006: Satellite-based assessment of marine low cloud variability associated with aerosol, atmospheric stability, and the diurnal cycle. *J Geophys Res*, **111,** D17204.

McFarquhar, G. M., S. Platnick, L. Di Girolamo, H. K. Wang, G. Wind, and G. Y. Zhao, 2004: Trade wind cumuli statistics in clean and polluted air over the Indian Ocean from in situ and remote sensing measurements. *Geophys Res Lett*, **31,** L21105.

Meier, J., B. Wehner, A. Massling, W. Birmili, A. Nowak, T. Gnauk, E. Brüggemann, H. Herrmann, H. Min, and A. Wiedensohler, 2009: Hygroscopic growth of urban

aerosol particles in Beijing (China) during wintertime: a comparison of three experimental methods. *Atmos Chem Phys*, **9,** 6865-6880.

Menon, S., J. Hansen, L. Nazarenko, and Y. Luo, 2002: Climate effects of black carbon aerosols in China and India. *Science*, **297,** 2250-2253.

Milbrandt, J. A., and M. K. Yau, 2005: A multimoment bulk microphysics parameterization. Part II: A proposed three-moment closure and scheme description. *J Atmos Sci*, **62,** 3065-3081.

Mlawer, E. J., S. J. Taubman, P. D. Brown, M. J. Iacono, and S. A. Clough, 1997: Radiative transfer for inhomogeneous atmospheres: RRTM, a validated correlated-k model for the longwave. *J Geophys Res*, **102,** 16663-16682.

Morrison, H., 2012: On the robustness of aerosol effects on an idealized supercell storm simulated with a cloud system-resolving model. *Atmos Chem Phys*, **12,** 7689-7705.

Nesbitt, S. W., R. Y. Zhang, and R. E. Orville, 2000: Seasonal and global NOx production by lightning estimated from the Optical Transient Detector (OTD). *Tellus Series B-Chemical and Physical Meteorology*, **52,** 1206-1215.

Nozaki, K. Y., 1973: Mixing depth model using hourly surface observations report 7053.

Orville, R. E., G. Huffines, J. Nielsen-Gammon, R. Y. Zhang, B. Ely, S. Steiger, S. Phillips, S. Allen, and W. Read, 2001: Enhancement of cloud-to-ground lightning over Houston, Texas. *Geophys Res Lett*, **28,** 2597-2600.

Pasquill, F., 1961: The estimation of the dispersion of windborne material. *Meteorological Magazin*, **90,** 33-49.

Patricola, C. M., M. Li, Z. Xu, P. Chang, R. Saravanan, and J.-S. Hsieh, 2012: An investigation of tropical Atlantic bias in a high-resolution coupled regional climate model. *Climate Dynamic*, **39,** 2443–2463.

Peng, J., M. Hu, S. Guo, Z. Du, J. Zheng, D. Shang, M. Levy Zamora, L. Zeng, M. Shao, Y.-S. Wu, J. Zheng, Y. Wang, C. R. Glen, D. R. Collins, M. J. Molina, and R. Zhang, 2016: Markedly enhanced absorption and direct radiative forcing of black carbon under polluted urban environments. *Proc Nat Acad Sci USA***,** 4266–4271.

Peng, J., M. Hu, S. Guo, Z. Du, D. Shang, J. Zheng, J. Zheng, L. Zeng, M. Shao, Y. Wu, D. Collins, and R. Zhang, 2017: Ageing and hygroscopicity variation of black carbon particles in Beijing measured by a quasi-atmospheric aerosol evolution study (QUALITY) chamber. *Atmos Chem Phys*, **17,** 10333-10348.

Petäjä, T., L. Järvi, V. M. Kerminen, A. J. Ding, J. N. Sun, W. Nie, J. Kujansuu, A. Virkkula, X. Yang, C. B. Fu, S. Zilitinkevich, and M. Kulmala, 2016: Enhanced air pollution via aerosol-boundary layer feedback in China. *Sci Rep*, **6,** 18998.
114

Powell, M. D., and T. A. Reinhold, 2007: Tropical cyclone destructive potential by integrated kinetic energy. *Bull Am Meteorol Soc*, **88,** 513-526.

Pruppacher, H. R., and J. D. Klett, 1997: *Microphysics of clouds and precipitation.* 2nd ed. Oxford Press, Oxford, UK.

Ramanathan, V., F. Li, M. V. Ramana, P. S. Praveen, D. Kim, C. E. Corrigan, H. Nguyen, E. A. Stone, J. J. Schauer, G. R. Carmichael, B. Adhikary, and S. C. Yoon, 2007: Atmospheric brown clouds: Hemispherical and regional variations in long-range transport, absorption, and radiative forcing. *J Geophys Res*, **112,** D22S21.

Rosenfeld, D., A. Khain, B. Lynn, and W. L. Woodley, 2007: Simulation of hurricane response to suppression of warm rain by sub-micron aerosols. *Atmos Chem Phys*, **7,** 3411-3424.

Rosenfeld, D., M. Clavner, and R. Nirel, 2011: Pollution and dust aerosols modulating tropical cyclones intensities. *Atmos Res*, **102,** 66-76.

Rosenfeld, D., W. L. Woodley, A. Khain, W. R. Cotton, G. Carrió, I. Ginis, and J. H. Golden, 2012: Aerosol effects on microstructure and intensity of tropical cyclones. *Bull Am Meteorol Soc*, **93,** 987-7001.

Saha, S., S. Moorthi, H.-L. Pan, X. Wu, J. Wang, S. Nadiga, P. Tripp, R. Kistler, J. Woollen, D. Behringer, H. Liu, D. Stokes, R. Grumbine, G. Gayno, J. Wang, Y.-T. Hou, H.-y. Chuang, H.-M. H. Juang, J. Sela, M. Iredell, R. Treadon, D. Kleist, P. V. Delst, D. Keyser, J. Derber, M. Ek, J. Meng, H. Wei, R. Yang, S. Lord, H. v. d. Dool, A. Kumar, W. Wang, C. Long, M. Chelliah, Y. Xue, B. Huang, J.-K. Schemm, W. Ebisuzaki, R. Lin, P. Xie, M. Chen, S. Zhou, W. Higgins, C.-Z. Zou, Q. Liu, Y. Chen, Y. Han, L. Cucurull, R. W. Reynolds, G. Rutledge, and M. Goldberg, 2010: The NCEP climate forecast system reanalysis. *Bull Am Meteorol Soc*, **91,** 1015-1058.

Sakaeda, N., R. Wood, and P. J. Rasch, 2011: Direct and semidirect aerosol effects of southern African biomass burning aerosol. *J Geophys Res*, **116,** D12205.

Saleeby, S. M., W. Berg, S. van den Heever, and T. L'Ecuyer, 2010: Impact of cloud-nucleating aerosols in cloud-resolving model simulations of warm-rain precipitation in the east China sea. *J Atmos Sci*, **67,** 3916-3930.

Saleeby, S. M., S. R. Herbener, S. C. van den Heever, and T. L'Ecuyer, 2015: Impacts of Cloud Droplet–Nucleating Aerosols on Shallow Tropical Convection. *J Atmos Sci*, **72,** 1369-1385.

Schade, L. R., and K. A. Emanuel, 1999: The ocean's effect on the intensity of tropical cyclones: Results from a simple coupled atmosphere–ocean model. *J Atmos Sci*, **56,** 642-651.

Seifert, A., and K. D. Beheng, 2006: A two-moment cloud microphysics parameterization for mixed-phase clouds. Part 2: Maritime vs. continental deep convective storms. *Meteorol Atmos Phys*, **92,** 67-82.

Seigel, R. B., 2014: Shallow cumulus mixing and subcloud-layer responses to variations in aerosol loading. *J Atmos Sci*, **71,** 2581-2603.

Shi, J. J., T. Matsui, W. K. Tao, Q. Tan, C. Peters-Lidard, M. Chin, K. Pickering, N. Guy, S. Lang, and E. M. Kemp, 2014: Implementation of an aerosol-cloud-microphysics-radiation coupling into the NASA unified WRF: Simulation results for the 6-7 August 2006 AMMA special observing period. *Q J Roy Meteorol Soc*, **140,** 2158-2175.

Small, J. D., P. Y. Chuang, G. Feingold, and H. Jiang, 2009: Can aerosol decrease cloud lifetime? *Geophys Res Lett*, **36,** L16806.

Small, J. D., J. H. Jiang, H. Su, and C. X. Zhai, 2011: Relationship between aerosol and cloud fraction over Australia. *Geophys Res Lett*, **38,** L23802.

Storer, R. L., S. C. van den Heever, and G. L. Stephens, 2010: Modeling aerosol impacts on convective storms in different environments. *J Atmos Sci*, **67,** 3904-3915.

Sun, Y. L., Q. Jiang, Z. F. Wang, P. Q. Fu, J. Li, T. Yang, and Y. Yin, 2014: Investigation of the sources and evolution processes of severe haze pollution in Beijing in January 2013. *J Geophys Res*, **119,** 4380-4398.

Tang, G., J. Zhang, X. Zhu, T. Song, C. Münkel, B. Hu, K. Schäfer, Z. Liu, J. Zhang, L. Wang, J. Xin, P. Suppan, and Y. Wang, 2016a: Mixing layer height and its implications for air pollution over Beijing, China. *Atmos Chem Phys*, **16,** 2459-2475.

Tang, W., J. Qin, K. Yang, S. Liu, N. Lu, and X. Niu, 2016b: Retrieving high-resolution surface solar radiation with cloud parameters derived by combining MODIS and MTSAT data. *Atmos Chem Phys*, **16,** 2543-2557.

Tao, W. K., X. W. Li, A. Khain, T. Matsui, S. Lang, and J. Simpson, 2007: Role of atmospheric aerosol concentration on deep convective precipitation: Cloud-resolving model simulations. *J Geophys Res*, **112,** D24S18.

Tao, W. K., J. P. Chen, Z. Q. Li, C. Wang, and C. D. Zhang, 2012: Impact of aerosols on convective clouds and precipitation. *Rev Geophys*, **50,** RG2001.

Tao, W. K., T. Matsui, 2015: Cloud-system resolving modeling and aerosols. *Encyclopedia of Atmospheric Sciences*, **4,** 222-231.

Tie, X., R.-J. Huang, J. Cao, Q. Zhang, Y. Cheng, H. Su, D. Chang, U. Pöschl, T. Hoffmann, U. Dusek, G. Li, D. R. Worsnop, and C. D. O'Dowd, 2017: Severe pollution in China amplified by atmospheric moisture. *Sci Rep*, **7,** 15760.

116

Tie, X. X., S. Madronich, S. Walters, R. Y. Zhang, P. Rasch, and W. Collins, 2003: Effect of clouds on photolysis and oxidants in the troposphere. *J Geophys Res*, **108,** 4642.

Toon, O. B., and T. P. Ackerman, 1981: Algorithms for the calculation of scattering by stratified spheres. *Appl Opt*, **20,** 3657-3660.

Turner, D. D., S. A. Clough, J. C. Lijegren, E. E. Clothiaux, K. E. Cady-Pereira, and K. L. Gaustad, 2007: Retrieving liquid water path and precipitable water vapor from the atmospheric radiation measurement (ARM) microwave radiometers. *IEEE Trans Geosci Remote Sens*, **45,** 3680-3690.

Twomey, S., 1977: The influence of pollution on the shortwave albedo of clouds. *J Atmos Sci*, **34,** 1149-1152.

van den Heever, S. C., G. G. Carrió, W. R. Cotton, P. J. DeMott, and A. J. Prenni, 2006: Impacts of nucleating aerosol on Florida storms. Part I: Mesoscale simulations. *J Atmos Sci*, **63,** 1752-1775.

van den Heever, S. C., G. L. Stephens, and N. B. Wood, 2011: Aerosol indirect effects on tropical convection characteristics under conditions of radiative–convective equilibrium. *J Atmos Sci*, **68,** 699-718.

Vogelmann, A. M., G. M. McFarquhar, J. A. Ogren, D. D. Turner, J. M. Comstock, G. Feingold, C. N. Long, H. H. Jonsson, A. Bucholtz, D. R. Collins, G. S. Diskin, H. Gerber, R. P. Lawson, R. K. Woods, E. Andrews, H.-J. Yang, J. C. Chiu, D. Hartsock, J. M. Hubbe, C. Lo, A. Marshak, J. W. Monroe, S. A. McFarlane, B. Schmid, J. M. Tomlinson, and T. Toto, 2012: Racoro extended-term aircraft observations of boundary layer clouds. *Bull Am Meteorol Soc*, **93,** 861-878.

Wallace, J. M., and P. V. Hobbs, 2005: *Atmospheric science: An introductory survey.* Elsevier, New York.

Wang, G., R. Zhang, M. E. Gomez, L. Yang, M. Levy Zamora, M. Hu, Y. Lin, J. Peng, S. Guo, J. Meng, J. Li, C. Cheng, T. Hu, Y. Ren, Y. Wang, J. Gao, J. Cao, Z. An, W. Zhou, G. Li, J. Wang, P. Tian, W. Marrero-Ortiz, J. Secrest, Z. Du, J. Zheng, D. Shang, L. Zeng, M. Shao, W. Wang, Y. Huang, Y. Wang, Y. Zhu, Y. Li, J. Hu, B. Pan, L. Cai, Y. Cheng, Y. Ji, F. Zhang, D. Rosenfeld, P. S. Liss, R. A. Duce, C. E. Kolb, and M. J. Molina, 2016a: Persistent sulfate formation from London Fog to Chinese haze. *Proc Nat Acad Sci USA*, **113,** 13630-13635.

Wang, H., G. Y. Shi, X. Y. Zhang, S. L. Gong, S. C. Tan, B. Chen, H. Z. Che, and T. Li, 2015a: Mesoscale modelling study of the interactions between aerosols and PBL meteorology during a haze episode in China Jing–Jin–Ji and its near surrounding region – Part 2: Aerosols' radiative feedback effects. *Atmos Chem Phys*, **15,** 3277-3287.

Wang, J., D. J. Allen, K. E. Pickering, Z. Li, and H. He, 2016b: Impact of aerosol direct effect on East Asian air quality during the EAST-AIRE campaign. *J Geophys Res*, **121,** 6534-6554.

Wang, S., Q. Wang, and G. Feingold, 2003: Turbulence, condensation, and liquid water transport in numerically simulated nonprecipitating stratocumulus clouds. *J Atmos Sci*, **60,** 262-278.

Wang, Y., H. Che, J. Ma, Q. Wang, G. Shi, H. Chen, P. Goloub, and X. Hao, 2009: Aerosol radiative forcing under clear, hazy, foggy, and dusty weather conditions over Beijing, China. *Geophys Res Lett*, **36,** L06804.

Wang, Y., Q. Wan, W. Meng, F. Liao, H. Tan, and R. Zhang, 2011: Long-term impacts of aerosols on precipitation and lightning over the Pearl River Delta megacity area in China. *Atmos Chem Phys*, **11,** 12421-12436.

Wang, Y., J. W. Fan, R. Y. Zhang, L. R. Leung, and C. Franklin, 2013a: Improving bulk microphysics parameterizations in simulations of aerosol effects. *J Geophys Res*, **118,** 5361-5379.

Wang, Y., A. Khalizov, M. Levy, and R. Y. Zhang, 2013b: New Directions: Light absorbing aerosols and their atmospheric impacts. *Atmos Environ*, **81,** 713-715.

Wang, Y., K.-H. Lee, Y. Lin, M. Levy, and R. Zhang, 2014a: Distinct effects of anthropogenic aerosols on tropical cyclones. *Nat Clim Change*, **4,** 368-373.

Wang, Y., M. Wang, R. Zhang, S. J. Ghan, Y. Lin, J. Hu, B. Pan, M. Levy, J. H. Jiang, and M. J. Molina, 2014b: Assessing the effects of anthropogenic aerosols on Pacific storm track using a multiscale global climate model. *Proc Natl Acad Sci U S A*, **111,** 6894-6899.

Wang, Y., R. Y. Zhang, and R. Saravanan, 2014c: Asian pollution climatically modulates mid-latitude cyclones following hierarchical modelling and observational analysis. *Nature Communications*, **5,** 3098.

Wang, Y. S., L. Yao, L. L. Wang, Z. R. Liu, D. S. Ji, G. Q. Tang, J. K. Zhang, Y. Sun, B. Hu, and J. Y. Xin, 2014d: Mechanism for the formation of the January 2013 heavy haze pollution episode over central and eastern China. *Sci China Earth*, **57,** 14-25.

Wang, Z., X. Huang, and A. Ding, 2017: Dome effect of black carbon and its key influencing factors: A one-dimensional modelling study. *Atmos. Chem. Phys. Discuss.*, **2017,** 1-29.

Wang, Z. L., H. Zhang, and X. Y. Zhang, 2015b: Simultaneous reductions in emissions of black carbon and co-emitted species will weaken the aerosol net cooling effect. *Atmos Chem Phys*, **15,** 3671-3685.

Werner, F., F. Ditas, H. Siebert, M. Simmel, B. Wehner, P. Pilewskie, T. Schmeissner, R. A. Shaw, S. Hartmann, H. Wex, G. C. Roberts, and M. Wendisch, 2014: Twomey effect observed from collocated microphysical and remote sensing measurements over shallow cumulus. *J Geophys Res*, **119,** 1534-1545.

Wilcox, E. M., 2010: Stratocumulus cloud thickening beneath layers of absorbing smoke aerosol. *Atmos Chem Phys*, **10,** 11769-11777.

Wilcox, E. M., R. M. Thomas, P. S. Praveen, K. Pistone, F. A.-M. Bender, and V. Ramanathan, 2016: Black carbon solar absorption suppresses turbulence in the atmospheric boundary layer. *Proc Nat Acad Sci USA*, **113,** 11794-11799.

Williams, E. R., R. Zhang, and J. Rydock, 1991: Mixed-phase microphysics and cloud electrification. *J Atmos Sci*, **48,** 2195-2203.

Wood, E. C., M. R. Canagaratna, S. C. Herndon, T. B. Onasch, C. E. Kolb, D. R. Worsnop, J. H. Kroll, W. B. Knighton, R. Seila, M. Zavala, L. T. Molina, P. F. DeCarlo, J. L. Jimenez, A. J. Weinheimer, D. J. Knapp, B. T. Jobson, J. Stutz, W. C. Kuster, and E. J. Williams, 2010: Investigation of the correlation between odd oxygen and secondary organic aerosol in Mexico City and Houston. *Atmos Chem Phys*, **10,** 8947-8968.

Wood, R., 2012: Stratocumulus clouds. *Mon Wea Rev*, **140,** 2373-2423.

Wu, G., Z. Li, C. Fu, X. Zhang, R. Zhang, R. Zhang, T. Zhou, J. Li, J. Li, D. Zhou, L. Wu, L. Zhou, B. He, and R. Huang, 2016: Advances in studying interactions between aerosols and monsoon in China. *Sci China Earth*, **59,** 1-16.

Xia, X., H. Chen, P. Goloub, W. Zhang, B. Chatenet, and P. Wang, 2007: A compilation of aerosol optical properties and calculation of direct radiative forcing over an urban region in northern China. *J Geophys Res*, **112,** D12203.

Xue, H., and G. Feingold, 2006: Large-eddy simulations of trade wind cumuli: Investigation of aerosol indirect effects. *J Atmos Sci*, **63,** 1605-1622.

Xue, H., G. Feingold, and B. Stevens, 2008: Aerosol effects on clouds, precipitation, and the organization of shallow cumulus convection. *J Atmos Sci*, **65,** 392-406.

Yablonsky, R. M., and I. Ginis, 2009: Limitation of one-dimensional ocean models for coupled hurricane–ocean model forecasts. *Mon Wea Rev*, **137,** 4410-4419.

Yamaguchi, T., G. Feingold, J. Kazil, and A. McComiskey, 2015: Stratocumulus to cumulus transition in the presence of elevated smoke layers. *Geophys Res Lett*, **42,** 10,478-410,485.

Yang, Q., W. I. Gustafson, J. D. Fast, H. Wang, R. C. Easter, M. Wang, S. J. Ghan, L. K. Berg, L. R. Leung, and H. Morrison, 2012: Impact of natural and anthropogenic

aerosols on stratocumulus and precipitation in the Southeast Pacific: a regional modelling study using WRF-Chem. *Atmos Chem Phys*, **12,** 8777-8796.

Yu, H., S. C. Liu, and R. E. Dickinson, 2002: Radiative effects of aerosols on the evolution of the atmospheric boundary layer. *J Geophys Res*, **107,** 4142.

Yuan, T. L., Z. Q. Li, R. Y. Zhang, and J. W. Fan, 2008: Increase of cloud droplet size with aerosol optical depth: An observation and modeling study. *J Geophys Res*, **113,** D04201.

Zhang, D., W. F. Lei, and R. Y. Zhang, 2002: Mechanism of OH formation from ozonolysis of isoprene: kinetics and product yields. *Chem Phys Lett*, **358,** 171-179.

Zhang, G. J., and M. J. Mcphaden, 1995: The relationship between sea surface temperature and latent heat flux in the equatorial Pacific. *J Clim*, **8,** 589-605.

Zhang, M. H., W. Y. Lin, S. A. Klein, J. T. Bacmeister, S. Bony, R. T. Cederwall, A. D. Del Genio, J. J. Hack, N. G. Loeb, U. Lohmann, P. Minnis, I. Musat, R. Pincus, P. Stier, M. J. Suarez, M. J. Webb, J. B. Wu, S. C. Xie, M. S. Yao, and J. H. Zhang, 2005: Comparing clouds and their seasonal variations in 10 atmospheric general circulation models with satellite measurements. *J Geophys Res*, **110,** ISCCPD15S02.

Zhang, R., G. Li, J. Fan, D. L. Wu, and M. J. Molina, 2007: Intensification of Pacific storm track linked to Asian pollution. *Proc Natl Acad Sci U S A*, **104,** 5295-5299.

Zhang, R., A. F. Khalizov, J. Pagels, D. Zhang, H. Xue, and P. H. McMurry, 2008: Variability in morphology, hygroscopicity, and optical properties of soot aerosols during atmospheric processing. *Proc Nat Acad Sci USA*, **105,** 10291-10296.

Zhang, R., S. Guo, M. Levy Zamora, and M. Hu, 2015a: Reply to Li et al.: Insufficient evidence for the contribution of regional transport to severe haze formation in Beijing. *Proc Nat Acad Sci USA*, **112,** E2741.

Zhang, R., G. Wang, S. Guo, M. L. Zamora, Q. Ying, Y. Lin, W. Wang, M. Hu, and Y. Wang, 2015b: Formation of urban fine particulate matter. *Chem Rev*, **115,** 3803-3855.

Zhang, X., Q. Zhang, C. Hong, Y. Zheng, G. Geng, D. Tong, Y. Zhang, and X. Zhang, 2018: Enhancement of PM2.5 concentrations by aerosol-meteorology interactions over China. *J Geophys Res*, 1179-1194.

Zhao, J., R. Y. Zhang, K. Misawa, and K. Shibuya, 2005: Experimental product study of the OH-initiated oxidation of m-xylene. *Journal of Photochemistry and Photobiology a-Chemistry*, **176,** 199-207.